



Virginia Commonwealth University
VCU Scholars Compass

Theses and Dissertations

Graduate School

2018

Liquid Interaction with Non-wettable Surfaces Structured with Macroscopic Ridges

Mehran Abolghasemibizaki

Follow this and additional works at: <https://scholarscompass.vcu.edu/etd>



Part of the [Other Mechanical Engineering Commons](#), and the [Structural Materials Commons](#)

© The Author

Downloaded from

<https://scholarscompass.vcu.edu/etd/5381>

This Dissertation is brought to you for free and open access by the Graduate School at VCU Scholars Compass. It has been accepted for inclusion in Theses and Dissertations by an authorized administrator of VCU Scholars Compass. For more information, please contact libcompass@vcu.edu.

Copyright © 2018 Mehran Abolghasemibizaki. All Rights Reserved

Liquid Interaction with Non-wettable Surfaces Structured with Macroscopic Ridges

A dissertation submitted in partial fulfillment of the requirements for the degree of Doctor of
Philosophy at Virginia Commonwealth University

By

Mehran Abolghasemibizaki

M.Sc. in Mechanical Engineering, K.N. Toosi University of Technology, Tehran, Iran, 2011

Advisor: Reza Mohammadi

Assistant Professor, Department of Mechanical and Nuclear Engineering

Virginia Commonwealth University

Richmond, Virginia

May, 2018

Dedication

I dedicate this work to *Neda*, my wife, because without her support both mentally and practically achieving this importance would have been hardly possible.

Acknowledgement

I express my sincere acknowledgment to my advisor Dr. Reza Mohammadi for his guidance, endless support and encouragement of my scientific endeavors.

I would like to thank my committee members— Prof. Gary Atkinson, Prof. Carlos Castano, Prof. Ravi Hadimani, Prof. Hooman Tafreshi and Prof. Christina Tang for their constructive comments and suggestions.

The love and support of my parents have always been an encouragement for me to achieve what I aim for in my life. My appreciation to them is beyond something that I can write.

The support of my friends and facilities provided by Nanomaterials Core Characterization at VCU is much appreciated.

Virginia Commonwealth University is also appreciated for financially supporting this work.

Table of Contents

Dedication	iii
Acknowledgement	iv
Table of Contents	v
List of Figures	vii
List of Tables	xv
Abstract	xvi
Chapter 1 Introduction	1
1.1 Background	1
1.1.1 Droplet Motion on an Inclined Surface	3
1.1.2 Droplet Impact on Solid Substrates	4
1.1.3 Droplet Impact on Superhydrophobic Surfaces	5
1.2 Structure of This Dissertation	11
Chapter 2 Facile and Inexpensive Synthesis of Durable Superhydrophobic Carbon Soot Coatings	14
2.1 Introduction	14
2.2 Modified Soot Coating	15
2.2.1 Sample Preparation	15
2.2.2 Wettability and Characterization of Soot Coating (Modified and Conventional)	16
2.3 Chemically Functionalized Soot Coating	19
2.4 Conclusions	20
Chapter 3 Rolling Viscous Drops on Non-wettable Ribbed Surfaces	21
3.1 Introduction	21
3.2 Experimental Method	23
3.2.1 Sample Preparation	23
3.2.2 Surface Free Energy Examination	24
3.2.3 Rolling Drop Setup	26
3.3 Results and Discussion	28
3.3.1 Wettability and Surface Free Energy of the Soot-based Coatings	28
3.3.2 Rolling Viscous Drop	30

3.4 Conclusions	39
Chapter 4 Droplet Impact on Superhydrophobic Ribbed Surfaces	41
4.1 Introduction	41
4.2 Experimental Methods	42
4.2.1 Sample Preparation	42
4.2.2 Experimental Setup	45
4.3 Results and Discussion	46
4.4 Conclusions	58
Chapter 5 Droplet Impact on Cylindrical Surfaces to Achieve the Shortest Possible Contact Time	60
5.1 Introduction	60
5.2 Experimental Methods	62
5.2.1 Sample Preparation	62
5.2.2 Experimental Setup	63
5.3 Results and Discussion	64
5.4 Conclusions	73
Chapter 6 Overall Conclusions and Future Work	75
6.1 Conclusions	75
6.2 Future Work	76
Chapter 7 References	78
Appendix: Vita	84

List of Figures

Figure 1.1. Schematic diagram of the impact process on a single macrotexture. (a) A water droplet of radius R_o impacts on a macrotexture of height $a < \delta < R_o$ at velocity V . The diagram portrays (b) side and (c) top view of the recoiling pancake of thickness δ at non-uniform retraction velocity (V_r vs V_p). Adapted from Refs. [39, 40].	8
Figure 1.2. The variation of the position of the contact line, as shown as r in the inset, during the impact period. Courtesy of Bird et al. [39], used by permission.	9
Figure 1.3. Variation of the contact time of water droplet impacting on a macrotexture for (a) different radius of the droplet (b) different radius of the macrotexture when the impact velocity increases. Contact time on the texture is normalized by τ , contact time on the control smooth surface. Courtesy of Gauthier et al. [40], used by permission.	10
Figure 1.4. (a) Variation of contact line in axial and azimuthal directions during the droplet impact on a curved surface. (b) Splitting the contact time in the axial direction, the plot shows the variation of the spreading time (t_1 , left) and the retraction time (t_2 , right) for drop with $D_o = 2.9$ mm impacting on flat (Infinity) and curved surfaces with various diameters (D) at different impact velocities. Courtesy of Liu et al. [41]	11
Figure 2.1. Schematic diagram of the conical chimney used to manipulate the combustion process to achieve a modified soot coating. The dimensions are in cm. Courtesy of Esmerlyan et al. [63], used with permission.	15
Figure 2.2. Advancing and receding contact angles of the modified soot coating at different temperatures.	17

Figure 2.3. SEM image at low and high magnifications of (a) conventional and (b) modified carbon soot coating [47].	18
Figure 3.1. (a) The schematic diagram of the experimental setup. The inset is a SEM image of a functionalized soot coating that illustrates its nano-/micro-sized roughness. (b) The actual setup used for the tests.....	27
Figure 3.2. The snapshots from left to right depict how a 1 μL droplet of diiodomethane (CH_2I_2) spreads on untreated soot. The spreading occurs in less than 1 second. Olive oil also spreads similar on both untreated and ethanol-treated soot coatings.....	28
Figure 3.3. The top row (a) from left to right shows that the un-treated soot cannot detach a 5 μL water drop from the needle of 0.2 mm inside diameter due to its Cassie-Baxter state of wetting. The bottom row (b) illustrates how the same size drop sticks to the ethanol-treated soot as soon as it touches the surface (Wenzel state).	29
Figure 3.4. The radius (l) of the solid-liquid contact area for glycerol drops of different initial radii (R) sitting on the horizontal macroscopically-smooth, non-wettable surface. Both values were normalized with the capillary length $\kappa^{-1} = \sqrt{\gamma/\rho g} = 2.27\text{mm}$	32
Figure 3.5. The variation of the measured velocity normalized by $V_o = \frac{2(1-\cos\theta)\gamma\sin\alpha}{3\mu}$ as a function of drop radius normalized by κ^{-1} . The equation for V_o is taken from Richard and Quere's work [22]. It can be seen that the diagrams are sporadic for different tilting angles (α) and do not collapse in a single plot of $\frac{V}{V_o} \approx \frac{\kappa^{-1}}{R}$, similar to what Richard and Quere reported in their study. However, the results follow the trend of the smaller the drop, the faster it rolls.	33

- Figure 3.6. For the case of the rolling drop on a tilted surface at the angle of α , the δ is a consequence of the normal component of gravity to the surface..... 34
- Figure 3.7. The normalized velocity of the rolling drops as a function of their normalized radii for the 6 different tilting angles $\alpha = 5^\circ$ - 45° tested in this study. The solid black line represents $\frac{V}{V_o} = 2.23 \frac{\kappa^{*-1}}{R}$ where $V_o = \frac{\gamma}{\mu} \tan \alpha$ 35
- Figure 3.8. Glycerol drops of different radii deposited on (a) ribbed and (b) smooth surfaces. The capillary length for glycerol is ~ 2.27 mm..... 36
- Figure 3.9. The plot depicts the normalized velocity of the rolling drops versus their normalized radii on the ribbed surface for varied tilting angles (α). The solid black line represents $\frac{V_b}{V_o} = 2.83 \frac{\kappa^{*-1}}{R}$ where $V_o = \frac{\gamma}{\mu} \tan \alpha$ 37
- Figure 3.10. The plot shows the normalized velocity of glycerol drops rolling down, perpendicular to ridges, on the ribbed surface. The velocities are normalized by $V_o = \frac{\gamma}{\mu} \tan \alpha$ and the solid line represents the best fit for the data as $\frac{V_{b2}}{V_o} = 2.53 \frac{\kappa^{*-1}}{R}$ 38
- Figure 3.11. The image of (a) ribbed surface coated with functionalized soot and (b) skin pattern of the finger tip, taken using a Axio Lab optical microscope (Zeiss, Germany)..... 39
- Figure 4.1. Experimental configuration and materials. (a) A water droplet of radius R_o impacts on a ribbed surface with macrotexture of diameter $2b = 0.1$ - 0.3 mm at velocity V . (b) Low and (c) high magnification SEM images of a cube printed at $2b = 0.1$ mm and coated with functionalized soot. (d) The actual setup used for conducting the experiments..... 43

Figure 4.2. The top row from left to right shows that the volume of the water droplet advances from 3 μL to 6 μL while its advancing contact angle is $166.2 \pm 2.6^\circ$. The bottom row from right to left illustrates that receding contact angle of the surface is $164.1 \pm 1.2^\circ$, slightly lower than the advancing contact angle. 45

Figure 4.3. The ratio of the maximum spreading radius to initial radius of the droplet at different We . The ratio was measured experimentally for droplets of 6, 9, 16 and 31 μL impacting on the smooth PETG. Values of the initial radius of 6, 9, 16 and 31 μL droplets are 1.1, 1.3, 1.6 and 2.0 mm respectively. The maximum error bar is 0.05. The dashed line represents $1.02We^{0.25}$. This graph indicates that our measurements are sufficiently accurate and valid. 48

Figure 4.4. Water droplet of 9 μL impacting on ribbed ($2b = 0.2$ mm) and smooth surfaces at $V = 0.8$ m/s. The droplet symmetrically spreads to a circle on both samples. (a) The temporal variation of spreading radius (r), spreading length along (x) and perpendicular (y) to the cylindrical ridges during the impact. The data were acquired from side view videos. (b) Top view of the droplet at the end of the spreading stage on both samples; the circular pancake shape. 49

Figure 4.5. Impacting of a 9 μL water droplet at $V = 1.2$ m/s on (a) ribbed sample of $2b = 0.2$ mm and (b) smooth PETG. Unlike on the smooth surface, the droplet spreads to a quasi-elliptical shape and retracts in a non-circular manner on the ribbed substrate, which results in reduced contact time. The contact time for the ribbed surface is 11.4 ± 0.17 ms, compared to 13.5 ± 0.20 for the smooth sample. (c) The graph illustrates the variation of x , y and r , as defined earlier, during the impact. The data is extracted from top view videos for both surfaces. Extracting data continues until the outer rim seems stationary from the top view. 50

Figure 4.6. Impacting of a 9 μL water droplet at $V = 1.8$ m/s on (a) ribbed sample of $2b = 0.2$ mm and (b) smooth PETG. On the ribbed substrate, the droplet spreads to a barrel-shape at 3.4 ms and

retracts in a square-like manner. This faster anisotropic recoiling as well as splashing are the reasons for further contact time reduction. The contact time for the ribbed surface is 10.5 ± 0.45 ms, compared to 13.2 ± 0.40 for the smooth PETG. (c) Extracting the data from the top view videos, this graph depicts the variation of x , y and r during the impact. Since the splashing happens in x direction, the length of the outer edge before splashing is considered. 54

Figure 4.7. (a) The plot depicts the variation of the retraction and spreading time of a $9 \mu\text{L}$ water droplet impacting on smooth PETG and ribbed sample of $2b = 0.2$ mm for impact velocity changing from 0.4 to 2.2 m/s. Filled and empty circles show the retraction (t_{rs}) and spreading (t_{ss}) time on the smooth PETG, respectively, while the filled and empty triangles indicate the retraction (t_{rb}) and spreading (t_{sb}) time on the ribbed sample. The black solid line is the average of t_{rs} (10.0 ms) for $V = 1.0$ -2.2 m/s. The red dashed line is the average of t_{rb} (8.0 ms) for $V = 1.0$ -1.6 m/s, the range in which $t_{rb}/t_{rs} \approx \sqrt{2/\pi}$. (b) The pancake with the critical thickness on smooth PETG at $V = 2.2$ m/s, where it splashes from the outer rim. (c) The droplet adapts a butterfly shape at $V = 2.2$ m/s on the ribbed substrate. 55

Figure 4.8. (a) Variation of the contact time of a $9 \mu\text{L}$ water droplet for impact velocity $V = 0.4$ -2.2 m/s on smooth PETG as well as ribbed samples of $2b = 0.1$, 0.2 and 0.3 mm. The solid black line indicates that the average contact time of the droplet on smooth PETG is independent of V as reported in literature [31, 40]. The red dashed line shows the average contact time of 11.5 ms on the ribbed samples for $V = 1.0$ -1.6 m/s, intermediate impact regime, which is 13% shorter than that on the smooth PETG. The reduction in contact time is attributed to the 20% shorter retraction time on the ribbed samples. (b) For the ribbed sample of $2b = 0.2$ mm, the plot shows the contact time of water droplets of four volumes normalized by their contact time on smooth PETG. The

black dashed line illustrates a 13% reduction for $We \sim 15-50$, the intermediate impact regime, before the droplets start to splash on the ribbed surface. 56

Figure 4.9. (a) Contact time of 9 μL water droplet normalized by $\tau_o = \sqrt{\rho R_o^3 / \gamma}$ is plotted for superhydrophobic ribbed ($2b = 0.2 \text{ mm}$) with no wire, wired smooth (Ni wire diameter, $d = 0.1 \text{ mm}$), ribbed with wire along and perpendicular to the ridges at varied impact regimes. The schematic cross section of ribbed with wire along (b) and perpendicular (c) to the ridges are shown. 58

Figure 5.1. (a) Experimental configuration. (b) Side view of a ribbed-curved sample with radius of 4.5 mm and ridges of 300 μm in diameter. (c) Image of a curved specimen ($R = 4.5 \text{ mm}$) with an additional macroscopic copper wire (with a diameter of 0.2 mm) on its peak prior to coating. 64

Figure 5.2. Impact of a 9 μL water droplet at $V = 1.0 \text{ m/s}$ on (a) flat and (b) curved ($R = 4.5 \text{ mm}$) substrates. Spreading time in the axial direction (x) is equal to that found on a flat surface. Contact times were found to be $13.57 \pm 0.06 \text{ ms}$ (obtained from side-view videos) for the flat surface and $10.10 \pm 0.23 \text{ ms}$ (obtained from front-view videos) for the curved one. (c) Temporal variation of x , r , and z , as defined in this chapter, during the impact. Extracting data points for x continued until the outer rim was visible from the side view. Comparing the data of this diagram with the similar content reported by Liu et al. [41], the accuracy and validity of our measurements are confirmed. (d) Scanning electron microscopy (SEM) image of the functionalized soot utilized as superhydrophobic coating. 66

Figure 5.3. The maximum spreading radius and lengths normalized by $R_o = 1.29 \text{ mm}$ (9 μL) for different Weber numbers (various V). The dashed, solid, and dotted lines respectively depict $x^* =$

$1.00We^{0.24}$, $r^* = 1.02We^{0.25}$, and $z^* = 0.97We^{0.35}$. The error bars were too small to be shown (< 0.04). 67

Figure 5.4. The plot displays how the normalized retraction velocities ($V_r^* = V_r/\nu$) for curved and flat surfaces correlate with x^* and r^* , respectively. The solid black line illustrates that $V_r^* \propto r^*$, whereas the dashed red line follows $V_r^* \propto x^{*\frac{3}{2}}$. 68

Figure 5.5. (a) The plot shows the trend of the reduction of contact time on curved surfaces as the Weber number increases. The contact time has been normalized by the inertial-capillary time scale $\tau_o = \sqrt{\rho R_o^3/\gamma}$. The solid black line represents $\frac{t_c}{\tau_o} = 2.612We^{-0.12}$. The dashed green lines show the top and bottom boundaries of the numerical coefficient in Equation (5.3) for data acquired from the droplet impacts with different R/R_o ratios with a 95% confidence. (b) This plot shows that the normalized contact time versus Weber number for ribbed-curved samples follows the same trend yet with a slightly smaller numerical coefficient: $C = 2.528 \pm 0.269$ (the solid black and dashed green lines). The insets show that the edges of liquid film spreading on a ribbed-curved sample do not contact the solid substrate for high impact velocities, whilst they keep connected on the curved surface. The insets are associated with the impact of a 9 μL droplet on a curved/ribbed-curved surface of $R = 4.5$ mm at $V = 1.6$ m/s ($R/R_o = 3.49$). 70

Figure 5.6. For the case of $R/R_o = 3.49$, the plot depicts the variation of the normalized contact time vs changing the Weber number for ribbed-curved samples with various ridge's diameters ($2b = 100\text{-}300$ μm). The plot illustrates that changing the size of the ridges barely changes the contact time. The solid black line represents $\frac{t_c}{\tau_o} = 2.528We^{-0.12}$. 71

Figure 5.7. This plot demonstrates that the contact time of a bouncing 9 μL droplet on curved, ribbed-curved, wired curved, and wired ribbed-curved substrates decreases as the impact velocity

increases. The wired ribbed-curved substrate exhibits a contact time of $tc = 0.84 \pm 0.02\tau_o$ for $V = 1.6\text{-}2.0$ m/s, which may be the shortest contact physically possible. 72

Figure 5.8. Impact of the 9 μL water droplet at $V = 1.8$ m/s on the wired ribbed-curved ($R = 4.5$ mm) substrates. While the inertial-capillary time scale of the impact is $\tau_o = 5.44$ ms, the last point of the droplet leaves the surfaces at 4.5 ms (may not be clear here). This means that $tc \approx 0.84\tau_o$, which is an unprecedented contact time. 73

List of Tables

Table 3.1. Surface tension components of the liquids used to evaluate surface energy of the four solid surfaces studied. We have measured the total surface tension values (second column) in our experiments, while their contributing components (third and fourth columns) have been estimated by consulting Ref. [78].	26
Table 3.2. Contact angle values of water, diiodomethane, glycerol and olive oil on untreated soot, ethanol-treated soot, perfluorocarbon-treated soot and functionalized soot.	28
Table 3.3. The results of surface energy calculations for the different types of soot-based coatings. The values were obtained using Equation (3.3) and the data presented in Table 3.1 and Table 3.2.	30

Abstract

LIQUID INTERACTION WITH NON-WETTABLE SURFACES STRUCTURED WITH MACROSCOPIC RIDGES

By Mehran Abolghasemibizaki, Ph.D.

A dissertation submitted in partial fulfillment of the requirements for the degree of Doctor of Philosophy at Virginia Commonwealth University

Virginia Commonwealth University, 2018

Major Director: Reza Mohammadi, Assistant Professor, Department of Mechanical and Nuclear Engineering

Self-cleaning, anti-corrosion, anti-icing, dropwise-condensation, and drag-reduction are some applications in which superhydrophobic surfaces are implemented. To date, all the studies associated with superhydrophobic surfaces have been dedicated to understanding the liquid interaction with surfaces that are macroscopically smooth. The current study investigates the solid-liquid interaction of such surfaces which are fully decorated with macroscopic ridges (ribbed surfaces). In particular, the drop motion and impact on our newly designed non-wettable ribbed surface have been investigated in this work. Our experimental investigations have shown that liquid drops move faster on the ribbed surfaces due to lower friction induced by such a surface pattern. Moreover, an impacting droplet shows shorter contact time on ribbed surfaces. This concludes that ribbed surface pattern can be an efficient alternative design for the related applications.

Besides the experimental studies, the theoretical analyses done in this work have led to, firstly a scaling model to predict descent velocity of a rolling viscous drops on an inclined non-wettable surface more accurately. Secondly, for curved superhydrophobic surfaces a scaling model which

correlates the contact time of the impacting drop to its impact velocity has been developed. At the end, the knowledge obtained from this work has led to a special surface design which exhibits a contact time shorter than the inertial-capillary time scale, an unprecedented phenomenon.

Chapter 1 Introduction

1.1 Background

The interaction between a liquid drop and a solid surface is ubiquitous in our lives. While water is essential to life, its presence is not always beneficial. For instance, turbine blades will corrode when exposed to water and problems such as these have promoted the study and design of hydrophobic surfaces, which repel water. Mother Nature herself is not immune from water's effect, as she has often employed hydrophobic/superhydrophobic surfaces ranging from lotus leaves to gecko skin [1-4]. Having closely inspected a lotus leaf, researchers have found that the micro- and nanoscopic architecture of its surface holds air pockets underneath a drop sitting on it and consequently the drop holds its spherical shape and does not wet the leaf. Moreover, not only does Nature tailor a hydrophobic surface on a microscopic scale, she also does so on the macroscopic scale to optimize its performance [3, 4]. Inspired from this, the main objective of this work is to design and fabricate a non-wettable surface which repels the liquid drops as quickly as possible. Having fabricated a non-wettable surface structured with macroscopic ridges, I studied the liquid interaction with such a ribbed surface.

Generally, the wettability of a surface is assessed by its contact angle (θ) with a liquid droplet, determined through the balance of adhesive and cohesive forces acting on the three-phase contact line [5]. The cohesive forces of the liquid endeavor to minimize its surface area per volume, which causes the droplet to ball up and avoid further contact with the surface. On the other hand, the adhesive forces, depending on the chemistry of the substrate and its interaction with the liquid, tend to maximize the solid-liquid contact area [6, 7]. When the adhesive forces dominate the cohesive ones, the liquid drop wets the surface ($\theta < 90^\circ$), whereas if the cohesive forces overcome

the adhesive ones the surface gets wet partially. In most cases, water is used as the reference liquid; therefore, when the contact angle of a water droplet on a surface is acute, the surface is referred to as hydrophilic, whereas for contact angles $\theta \geq 90^\circ$ it is called hydrophobic. Superhydrophobicity, characterized by $\theta > 150^\circ$ and a contact angle hysteresis $< 10^\circ$ [7, 8], will be obtained when a hydrophobic surface acquires high-aspect-ratio surface protrusions in micro-scale [9]. Depositing a liquid drop on such a surface, if the liquid enters the surface asperities, the wetting is in the sticky Wenzel state with high contact angle hysteresis. In contrast, when the liquid suspends on the tips of the surface asperities and the air is preserved among the surface roughness, the slippery Cassie-Baxter state is achieved with low hysteresis [8].

Contact angle hysteresis is the difference between the values of dynamic contact angles, advancing and receding. Advancing contact angle is measured when the volume of the liquid drop sitting on the solid substrate increases, for example by injecting more liquid to the drop. The receding contact angle is associated with the value measured for a liquid drop shrinking in volume. Hence, if the wetting state of a liquid drop on a superhydrophobic surface is Wenzel, pinning happens and hysteresis will be high, while for the Cassie-Baxter state there is no pinning and the hysteresis will be sufficiently low ($< 10^\circ$).

The fabrication methods of superhydrophobic surfaces have been the focus of many studies due to the numerous applications of these surfaces such as drag-reduction [10], self-cleaning [2, 11, 12], anti-corrosion [13, 14], anti-icing [15, 16], and dropwise condensation [17-19]. The preparation methods can be categorized into bottom-up, top-down, and combination of both microfabrication approaches [20]. Both methods lead to surfaces with submicron roughness and low surface energy, the two main characteristics of a non-wettable surface. These methods, however, not only involve

many burdensome steps, but also require expensive pieces of equipment and lack scalability. An alternative method is depositing a layer of coating which inherently possesses the micro-/nanoscopic roughness, such as carbon soot.

The ribbed surface pattern utilized in this work was obtained by using an extruder-type 3D printer. A layer of our soot coating was deposited on the samples and then a chemical treatment [21] was done to achieve a functionalized soot coating with higher robustness and low surface energy. The interaction of liquid drops with such a non-wettable ribbed surface has been investigated from two distinguished points. First, the motion of drops on such a slippery surface and second, the dynamics of impact on them. These two broadly include the dynamic and practical solid-liquid interactions.

1.1.1 Droplet Motion on an Inclined Surface

A liquid drop with surface tension (γ), density (ρ), and radius (R_o) deposited on an inclined solid surface tilted at the angle of (α) moves down if its weight ($\frac{4\pi}{3}R_o^3\rho g \sin\alpha$, where g is the gravitational acceleration) exceeds the capillary force ($\pi l\gamma(\cos\theta_r - \cos\theta_a)$, where l is the radius of solid-liquid contact area and θ_r and θ_a are receding and advancing contact angle, respectively) [22]. It has been shown that if the liquid partially wets the surface, the larger the drop, the faster it moves [22-26] because the motion is mainly slipping generated by the weight of the drop. In the case of non-wettable surfaces, the scenario is indeed different and the viscosity (μ) of the liquid must be taken into consideration. For liquids of low viscosity, such as water, the drop runs down with an acceleration similar to a free fall in the early stage of the motion [23]. A viscous drop, however, rolls down at a constant descent velocity determined by the balance between viscous dissipation and the reduction rate of its gravitational potential energy, which results in the smaller the drop, the faster it rolls [22, 26]. Therefore one approach to examine to what extent decorating

a non-wettable surface with macroscopic ridges alters its interaction with liquids is comparing this descent velocity with that of a macroscopically-smooth counterpart, which will be discussed in detail in Chapter 3.

1.1.2 Droplet Impact on Solid Substrates

As Rioboo *et al.* [27] mentioned in their work, six different scenarios are likely to happen after the collision in droplet impact phenomena regarding to the liquid's properties and the wettability of the solid object; namely deposition, prompt splash, corona splash, receding breakup, partial rebound and rebound. Deposition, the most probable scenario, happens when the droplet spreads and stays attached to the solid substrate without any breakup during the impact process. This happens when the liquid partially wets the solid substrate and the surface has no surface asperities to interrupt the deposition process [27]. When the wettable surface becomes rough, the scenario changes to prompt splash. In prompt splash, many small droplets generate directly at the contact line at the beginning of the spreading phase when the radial velocity is high [27]. For example, when a liquid drop with low surface tension (ethanol $\gamma = 22$ mN/m) impacts on a micropatterned substrate made of polydimethylsiloxane (PDMS), a high enough impact velocity changes the deposition scenario to the prompt splash type [28]. Corona splash occurs when a drop hits a wettable surface with no roughness at high impact velocity [27] - for instance, an ethanol drop hitting smooth glass [29]. In this scenario the impacting drop appears as a corona after the collision, and smaller droplets generate around the rim of the corona, removed from the solid surface.

The last three scenarios belong to either superhydrophilic or superhydrophobic surfaces. When the liquid perfectly wets the surface (superhydrophilic), the receding contact angle can even get to zero. Receding breakup is a pure wetting phenomenon in which the receding contact angle

decreases while the liquid retracts from its maximum spreading radius, and some drops are left behind if the receding contact angle reaches the limiting value of zero [27, 30]. Partial rebound and rebound are observed when the solid substrate is superhydrophobic [27]. Superhydrophobic surfaces are achieved by both high degree of surface roughness and low surface energy, which enable them to trap air in their pores and exhibit contact angle $\theta > 150^\circ$ when they are in contact with water droplets. If the impact velocity is high enough to penetrate into the surface protrusions, partial rebound occurs, otherwise the droplet rebounds [23]. The scenario that we are studying is rebound, due to the superhydrophobicity of the carbon soot coating which we are utilizing in this research ($\theta \sim 165^\circ$).

1.1.3 Droplet Impact on Superhydrophobic Surfaces

When a water droplet lands on a superhydrophobic surface, its deformation is primarily controlled by its kinetic and surface energies [31], hence, the dynamic characteristics of the impact is defined by Weber number, $We = \rho V^2 R_o / \gamma$, in which V is the impact velocity of the droplet. If kinetic energy is much smaller than surface energy, $We \ll 1$, the water droplet behaves as a tennis ball hitting the ground [23, 32, 33]. In this regime the lower the impact velocity, the longer the contact time, which means that if the impact velocity is too small ($V \sim 0$), the droplet sticks to the surface [23, 31]. Above this critical point, ($We = 1$) however, the contact time is independent of the impact velocity. The water droplet behaves as spring of mass ρR_o^3 and stiffness γ with response time as

$$\tau_o = \sqrt{\rho R_o^3 / \gamma} \quad (1.1)$$

though its oscillation is far from being linear [23, 31-33]. For symmetric bouncing of a droplet in both low-deformation regimes ($We < 1$) and high-deformation regimes ($We > 1$), the contact time (t_c) is theoretically limited by the Rayleigh constant, $t_c/\tau_o \geq \pi/\sqrt{2} \approx 2.2$ [34], including Leidenfrost drops [35]. Although inertial-capillary time scale (τ_o) does not depend on the impact velocity, the deformation of the droplet and other details of the intermediate stages mainly depend on it.

Having struck a superhydrophobic surface, a water droplet deforms to a pancake of radius R_{max} and thickness δ . Due to the high restitution coefficient (of the order of 0.9) and small enough capillary number ($\mu V/\gamma < 0.03$) the effect of viscosity can be neglected [23, 32], Euler's equation thus can be used for scaling analysis [33, 36].

$$\rho \frac{DV}{Dt} = -\nabla P + \rho g \quad (1.2)$$

Okumura *et al.* [33] claimed that since the collision occurs during an impacting time R_o/V , the inertial term in Equation (1.2) is of the order of $\rho V^2/R_o$. The Laplace pressure scales as γ/δ , which changes over the thickness of the pancake δ , hence, the pressure gradient scales as γ/δ^2 . Moreover, the thickness of the pancake scales as R_o^3/R_{max}^2 through the conservation of mass. Since the deformation is large enough to neglect the gravity term, Equation (1.2) can be dimensionally written as

$$\frac{\rho V^2}{R_o} = \frac{\gamma R_{max}^4}{R_o^5} \quad (1.3)$$

Therefore the maximum radius of the pancake scales as

$$R_{max} \sim R_o We^{1/4} \quad (1.4)$$

Equation (1.4) can be deduced from another approach [36] as well. For a sessile drop, a puddle (pancake) forms when the size of the droplet is larger than the capillary length [22, 37], $\kappa^{-1} = \sqrt{\gamma/\rho g}$. Since balance between gravity and surface forces defines the shape of the puddle, its thickness scales with κ^{-1} [38]. As the impact velocity (V) decreases to zero during the impacting time R_o/V , the acceleration experienced by the drop is V^2/R_o , not g . Casting this reinforced gravity field to define a new capillary length causes the thickness of the puddle to scale with $\sqrt{\gamma R_o/\rho V^2}$. Employing the conservation of mass, Equation (1.4) can be deduced at the end [36]. This approach will be explained in more detail in Chapter 4.

Recently, two techniques have shown that the Rayleigh limit [34, 35] can be pushed lower through altering the dynamics of impact during spreading and recoiling stages [39-41]. The first technique provides a single macrotexture, whose amplitude is comparable to the thickness of the pancake, on a flat superhydrophobic surface [39, 40]. Second, designing a cylindrical superhydrophobic substrate whose radius is in the order of the radius of the impacting droplet [41].

On a flat superhydrophobic surface, the droplet spreads symmetrically to a pancake of uniform thickness (δ). The center of the pancake is inert during the retraction stage while its edge retracts at a constant velocity of [23, 42, 43]

$$V_r = \sqrt{2\gamma/\rho\delta} \quad (1.5)$$

If a water droplet impacts on a macrotexture, as shown in Figure 1.1, the symmetrical spreading will be interrupted. Since the liquid film is thinner along the macrotexture, the retraction velocity is faster with less mass to accelerate [39], see Figure 1.1b-c.

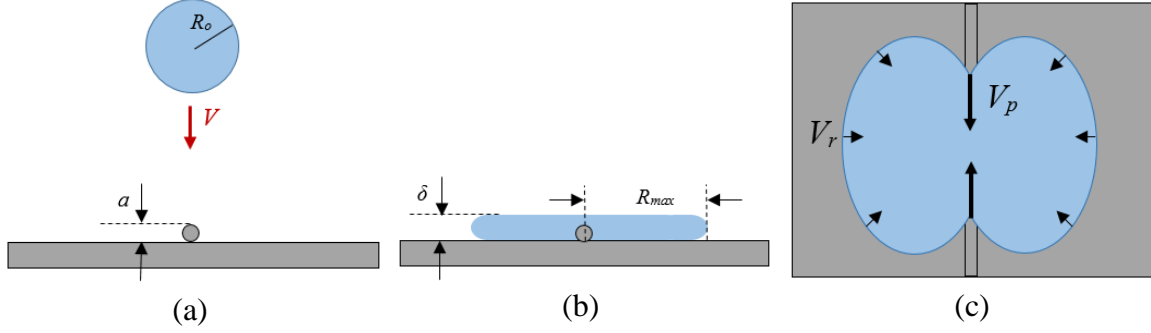


Figure 1.1. Schematic diagram of the impact process on a single macrotexture. (a) A water droplet of radius R_o impacts on a macrotexture of height $a < \delta < R_o$ at velocity V . The diagram portrays (b) side and (c) top view of the recoiling pancake of thickness δ at non-uniform retraction velocity (V_r vs V_p). Adapted from Refs. [39, 40].

Bird *et al.* [39] claimed that according to the Equation (1.5), the retraction velocity for the thin film on the peak of the macrotexture is approximately $V_p \approx \sqrt{2\gamma/\rho(\delta - a)}$, where a is the texture's amplitude, therefore, the outer edges of the liquid film on the texture recoils toward the center at higher speed. Using this rationality and assuming that the retraction velocity of the newly-formed inward rim is equal to the rest of the retracting film, they came up with an expression to predict the contact time reduction. Not only did the expression depend on the thickness of the flattened droplet, which is controlled by the impact velocity, but also it underestimated the contact time reduction by factor of 2 for their specifically designed experiment. It explains that the contact time reduction for a superhydrophobic macrotexture depends on the impact velocity, an important point that has been neglected. Bird *et al.* [39] presented Figure 1.2 to show how the water drop spreads and retracts on the macrotextured surface (black circles) versus on the smooth control surface (red squares). The most important point of this plot is that the spreading time (T_s) on the both surfaces are equal, something that will be revisited in Chapter 4.

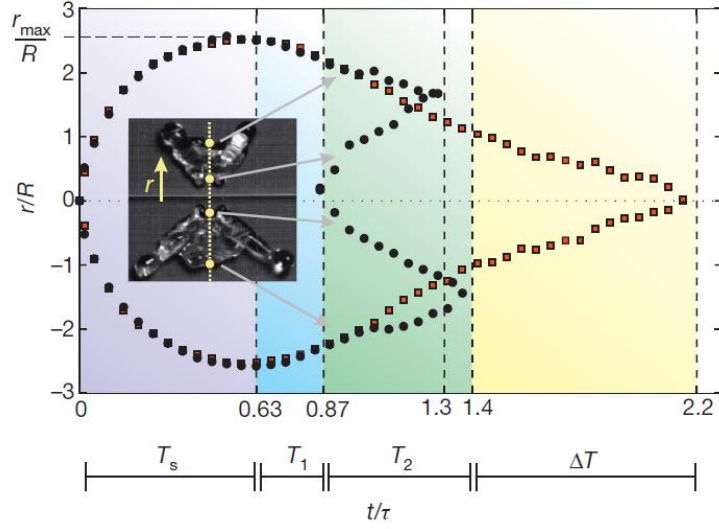


Figure 1.2. The variation of the position of the contact line, as shown as r in the inset, during the impact period. Courtesy of Bird *et al.* [39], used by permission.

Since it became clear that the contact time reduction from implementing a single macrotexture depends on the impact velocity, Gauthier *et al.* [40] investigated how this reduction varies with respect to this crucial parameter. They claimed that the contact time takes distinct values of $\sim \tau/\sqrt{2}$ and $\sim \tau/\sqrt{4}$ at relatively intermediate and high impact velocity ranges, respectively, where τ is the contact time on a macroscopically-smooth surface [40], which they presented in Figure 1.3. They interpreted that these values are the consequence of the formation of 2 and 4 main liquid subunits at the corresponding velocity ranges during the spreading stage. However, it can be seen that the actual values are a little higher than what they predicted. Figure 1.3 also has two important points that will be revisited in Chapter 4. First, the contact time decreases in a step-like manner as the impact velocity increases. Second, changing the size of the macrotexture (b) has no effect on the reduction value and manner.

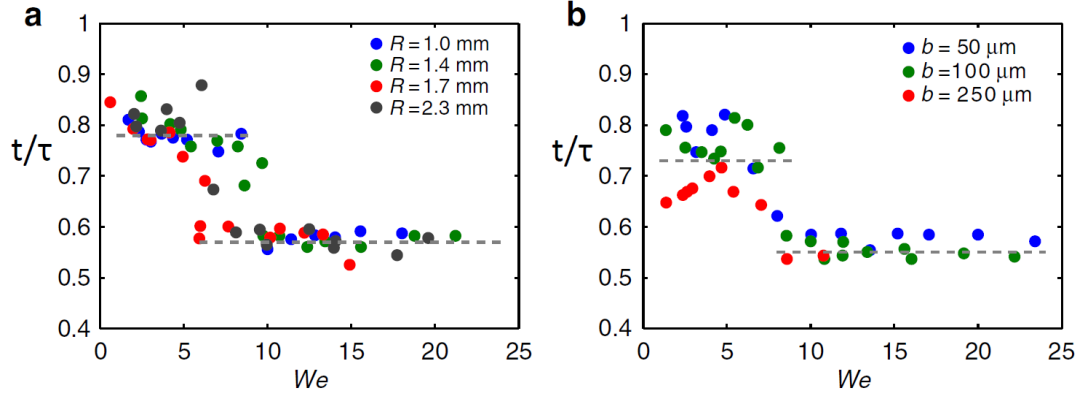


Figure 1.3. Variation of the contact time of water droplet impacting on a macrotexture for (a) different radius of the droplet (b) different radius of the macrotexture when the impact velocity increases. Contact time on the texture is normalized by τ , contact time on the control smooth surface. Courtesy of Gauthier *et al.* [40], used by permission.

Moreover, such an outstanding reduction ($\sim \tau/\sqrt{4}$) happens when the drop hits the macrotexture exactly in the center and it shifts back to τ as the impact center recedes into the distance R_{max} . Therefore, an investigation to clarify how the contact time varies if a non-wetting surface is *fully decorated with macrotextures*, which will be discussed in Chapter 4, is needed.

The other technique for reducing the contact time is fabricating a cylindrical superhydrophobic surface whose curvature is comparable to the droplet size [41]. Unlike flat or spherical surfaces, a cylindrical surface breaks the symmetry of the bouncing drop during the spreading stage, which assists the stationary center of the flattened drop to take off sooner in recoiling stage. Recently, Liu *et al.* [41] studied the impact of water droplet on curved superhydrophobic surfaces and reported that the drop spreads preferentially in azimuthal (curved) direction rather than in axial (straight) direction, which results in elliptical spreading. Since the tangential component of the momentum is disturbed less in the azimuthal direction compared to the axial one, more momentum is transferred to this direction [41]. This asymmetric spreading can be seen in Figure 1.4a. Since they have observed that the liquid drops leave the surface as soon as the retraction in the axial direction completes, they split the contact time in this direction into its components, spreading and

retraction times, as shown in Figure 1.4b. The important point of their study that will be revisited in Chapter 5 is that, for all the cases they studied, the spreading time in the axial direction of a curved surface is equal to that of a flat one (expressed by $D/D_o \sim \text{infinity}$). Using this incident, we found a scaling model for the contact time reduction on curved surfaces with respect to the impact velocity, which will be discussed in detail in Chapter 5.

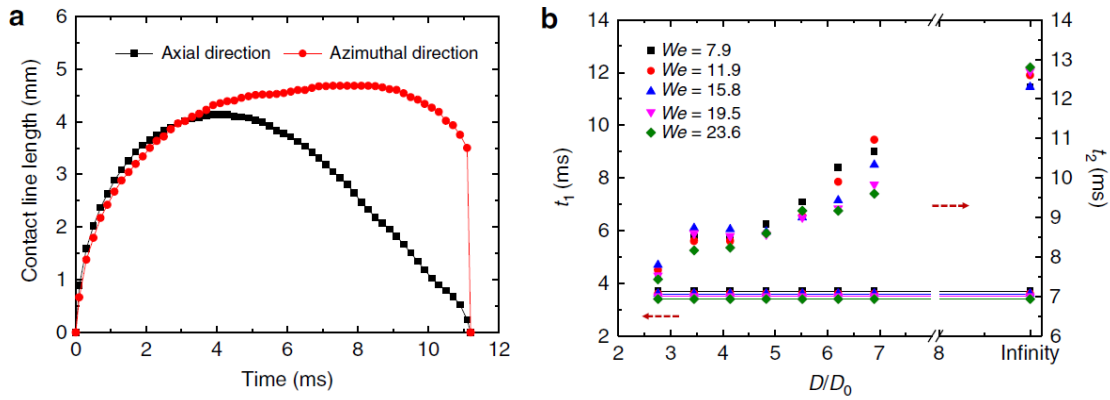


Figure 1.4. (a) Variation of contact line in axial and azimuthal directions during the droplet impact on a curved surface. (b) Splitting the contact time in the axial direction, the plot shows the variation of the spreading time (t_1 , left) and the retraction time (t_2 , right) for drop with $D_o = 2.9$ mm impacting on flat (Infinity) and curved surfaces with various diameters (D) at different impact velocities. Courtesy of Liu *et al.* [41]

1.2 Structure of This Dissertation

This dissertation explains how we have managed to fabricate a non-wettable surface enveloped in cylindrical ridges (ribbed surfaces) and then study its interaction with liquid drops. Chapter 2 discusses our engineering approach to prepare an inherently robust superhydrophobic soot coating with a good adhesion to the substrate. We used a specially-designed conical chimney to manipulate the combustion process of rapeseed oil and produce a modified soot coating.

In Chapter 3, the wettability study of our coating is completed and then the rolling of a viscous drop on our ribbed surfaces is discussed [44]. Since the non-wetting property of a surface should

rise as its roughness increases, the drop should move faster on a ribbed surface. Such a surface was obtained via soot deposition on a solid specimen printed by an extruder-type 3D printer. It was found that the ribbed surface aids the liquid drops to roll down $\sim 27\%$ faster (along the ridges) compared to the surface with no ridges. This faster velocity advocates the implementation of ribbed surfaces for drag-reduction and self-cleaning applications. In addition, a modified scaling model which predicts the descent velocity of viscous rolling drops more accurately than the original one was found and presented in this chapter [44].

Although the amount of time during which the collision happens is mostly in the order of 10 ms for millimetric droplets, decreasing this contact time is beneficial in many applications. As mentioned earlier, it has been shown that decorating a superhydrophobic surface with a single macrotexture reduces the contact time if the droplet hits the texture exactly in the center. To address this restriction, in Chapter 4 we systematically study the dynamic of water droplet impact on a surface fully decorated with cylindrical ridges at different impact velocities and ridge sizes for varied drop volumes. Our data show that when the kinetic energy of the drop is sufficient to completely wet the ridges, intermediate regime, the contact time reduces $\sim 13\%$ as the consequence of $\sim 20\%$ faster retraction, regardless of the location of the contact point [45]. In high impact regime, the contact become shorter since the flattened drop splashes from the periphery. The simplified, time-efficient and inexpensive method of fabrication presented in this chapter can be employed in fabricating many versatile non-wettable surfaces with complex geometries.

From the work of Chapter 4, it can be concluded that a ribbed-curved surface with an additional macrotexture on top of its peak may logically lead to a very short contact time. This investigation is presented in Chapter 5. The bouncing of water droplets of three different volumes on curved and

ribbed-curved samples with two different diameters was investigated for varied impact velocities [46]. Our theoretical investigation led to a scaling model for the contact time reduction with respect to the impact velocity on curved surfaces. It was found that adding a macroscopic wire to the peak of a cylinder structured with macro-scale ridges (wired ribbed-curved surfaces) yields the contact time even shorter than the inertial-capillary time scale, an unprecedented phenomenon [46].

Finally, Chapter 6 concludes our studies and proposes some investigations for future.

Chapter 2 Facile and Inexpensive Synthesis of Durable Superhydrophobic Carbon Soot Coatings

2.1 Introduction

This chapter summarizes the parts of our studies, on the preparation of surfaces [47-49], relevant to this dissertation. Using a candle flame or burning rapeseed oil has become popular among the scientific community for making superhydrophobic surfaces, because it does not need cumbersome processes like lithography and chemical etching in microfabrication [50-56]. However, since the soot layer is fragile due to the weak attraction forces between the nanoparticles [57, 58], producing a stable superhydrophobic coating requires a chemical stabilizer such as epoxy resin [59], paraffin wax [58], PDMS [11], silica gel [57] or silicon [60]. Utilizing the stabilizer not only reduces the simplicity of the fabrication process, it imposes some limitations for their applicability, e.g. low adhesion to gold coated surfaces [61] and high sensitivity to temperature and humidity variations [62].

In the Advanced Functional Materials Laboratory at the Department of Mechanical and Nuclear Engineering at VCU, we discovered an enhanced, simplified and time-efficient method for preparing an inherently robust superhydrophobic carbon soot coating that does not require any additional stabilizer [47]. Utilizing a specially-designed conical aluminum chimney during the combustion decreases the level of oxygen and alters the ratio of chemical bonds in the soot, which results in denser and fused carbon chains. The modified soot coating shows improved mechanical durability and thermal stability that retains its integrity up to ~300 °C. In addition, due to the high deposition rate (~1.5 $\mu\text{m/s}$), the coating can be applied even on materials with low thermal stability (e.g. wood or polyethylene) [47].

2.2 Modified Soot Coating

2.2.1 Sample Preparation

A paper based wick was immersed in ~50 mL of rapeseed oil previously added to a glass evaporating dish. A cone-shaped aluminum chimney (dimensions listed below) was mounted over the wick after ignition. Subsequently, a few glass slides (75×25 mm), aluminum, and copper substrates, as well as polyethylene pads and wood rods were exposed over the fume to be coated by a layer of carbon soot. As shown in Figure 2.1, the dimensions of the chimney were: height $h = 13\text{ cm}$, diameter $d = 6\text{-}1.5\text{ cm}$ (bottom and top, respectively) and a narrow $1.5 \times 2.5\text{ cm}$ opening as air-inlet at the bottom side. Moreover, soot-coated surfaces without using a chimney (conventional soot) were prepared for sake of the comparison [47].

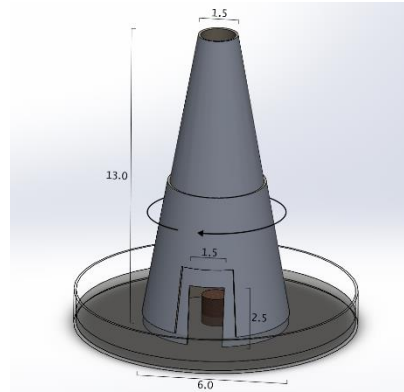


Figure 2.1. Schematic diagram of the conical chimney used to manipulate the combustion process to achieve a modified soot coating. The dimensions are in cm. Courtesy of Esmeryan *et al.* [63], used with permission.

Investigating the coating's thickness with regard to the deposition time shows a linear correlation at the rate of $\sim 1.5\text{ }\mu\text{m/s}$ [47]. Moreover, the deposition distance is irrelevant to the film thickness, but affects its stability and uniformity. It was found that within 3-7 cm above the tip of the chimney is the best position to achieve a stable, uniform, and homogeneous coatings. For instance, due to the high temperature of the region just above the chimney's tip (0-2 cm) the incomplete

combustion of carbon nanoparticles is unstable at this position. Moreover, the low temperature (below 100 °C) at the position further than 7 cm from the tip causes instability for the soot deposition too [47]. All samples, including glass, aluminum, copper, polyethylene and wood were exposed to the fume at 3-7 cm above the chimney for 25 seconds.

Later, we improved our combustion system with a precise air flow control and found more details about the formation mechanism of graphite-like (soot) and diamond-like carbon (DLC) nanostructure in low temperature laminar diffusion flames [49]. The DLC forms in a narrow stoichiometric range of the flame temperature within ~210-260 °C and beyond this range the soot coating can be produced.

2.2.2 Wettability and Characterization of Soot Coating (Modified and Conventional)

To examine the wettability of the modified and conventional soot coating deposited on the different materials mentioned above, advancing (ACA) and receding (RCA) contact angles were investigated using a Drop Shape Analyzer (DSA25E, KRUSS Germany). The contact angles of a de-ionized (DI) water droplet of 3 μ L initially, cycling to 6 μ L, were measured with an accuracy of $\pm 0.1^\circ$ using the tangent method provided by the goniometer's resident software (DSA4). Each measurement was repeated and averaged at five different areas of each sample. Type II de-ionized (DI) water (resistivity > 20 M Ω .cm), with a surface tension of ~73 mN/m (measured using our DSA25E) was obtained from a Milli-Q water purification system (Millipore, USA) and used for the experiments. The thermal sustainability of the modified coatings was examined by heating carbon soot coated glass slides on a hot plate up to 400 °C with a step of 50 °C for 30 min. After cooling to room temperature, the ACA and RCA of the samples were measured. The experimental results are summarized in Figure 2.2.

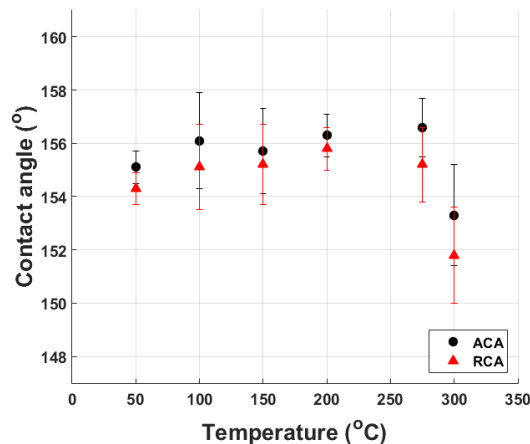


Figure 2.2. Advancing and receding contact angles of the modified soot coating at different temperatures.

It turns out that the ACA and RCA of modified and conventional soot coating are equal regardless of the substrates' materials at room temperature: ACA $\sim 154.5 \pm 0.9^\circ$ and RCA $\sim 153.8 \pm 1.1^\circ$. At higher temperatures, however, the conventional soot peels off when its temperature rises to 50 °C. Up to 275 °C, the modified soot coated glass substrate shows high ACA and RCA in the range of 155.1-156.6° and 154.3-155.8°, respectively, thereby confirming temperature sustainability of the superhydrophobic coating [47]. The coating's superhydrophobic properties remains intact up to 300 °C, but its stability is damaged since some parts of the soot peeled off after rinsing under tap water. Apparently, above this temperature the structure of the layer changes drastically. Such a structural alteration might be attributed to the mobility of carbon atoms at high temperatures [64]. The excessive thermal energy breaks the carbon bonds and the nanostructure transformed into the "onion-type", similar to what occurs after electron irradiation [64]. The complete transformation of the structure which leads to being washed away easily with a water jet occurs at 400 °C.

The Scanning Electron Microscopy (SEM) images in Figure 2.3 illustrates the surface morphology and structure of conventional and modified carbon soot coatings on glass slides [47]. Both images depict the irregular precipitation of the carbon soot on the substrates, forming elongated islands

separated by micro- and nanoscale pores, regardless of the coating approach. The only difference that can be seen is that the particles are much closer to each other in the modified soot. This could be the reason of their stability upon contact with water.

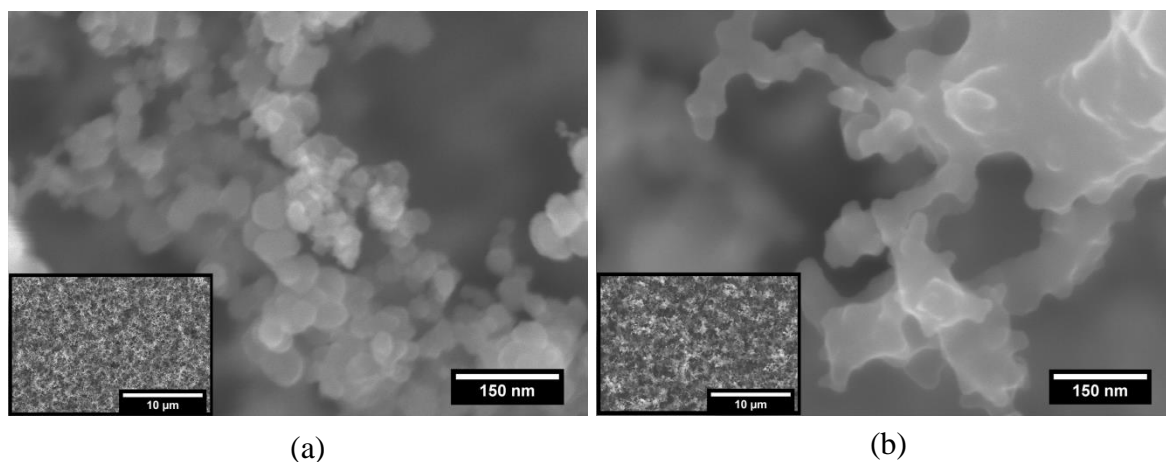


Figure 2.3. SEM image at low and high magnifications of (a) conventional and (b) modified carbon soot coating [47].

Results from Energy Dispersive Spectroscopy (EDS) reveal smaller atomic percentage of oxygen (by a factor of 8) for modified soot, which is attributed to the decrease in the level of oxidizer during the combustion process in the chimney [47]. These results are in accord with those from X-ray photoelectron spectroscopy (XPS), which shows 2.7% and 1.4% of oxygen for conventional and modified soot, respectively. The reduction of oxygen caused by utilizing the chimney leads to reduced amount of C-OH groups, which are hydrophilic active sites and cause mechanical instability in contact with water [47, 65]. High-resolution XPS to C1s analysis also shows that the sp^2/sp^3 ratio decreases by implementing the chimney, 1.17 and 0.91 for the conventional and modified soot, respectively. This reduction is one of the reasons for the fused structure and mechanical durability of the modified carbon soot. More explanation is provided in Ref. [47].

2.3 Chemically Functionalized Soot Coating

Although chimney-enhanced process of soot coating provides relatively robust and stable superhydrophobic coating with high contact angle and low hysteresis, it is not suitable for our purpose in this research. When a water droplet impacts on a modified soot coating at medium velocity ($V \sim 1$ m/s), it peels off some part of the coating and leads to inconsistent results, especially regarding contact time. After spending a relatively large amount of time, we found that we have to implement a more stable superhydrophobic coating whose integrity does not alter after being exposed to striking water droplets. Recently, our research group found that secondary treatment with ethanol and aqueous fluorocarbon solution of the coating improves its mechanical strength without altering its hydrophobicity [66]. Such a functionalized coating keeps its superhydrophobicity upon compressed air scavenging, spinning and water jetting with impact velocity of ~ 25 m/s. We amended the functionalizing process explained in Ref. [66] to be applicable to our samples, and it is described in Chapters 3-6.

As explained in Ref. [66], the ethanol reacts with the remaining oxygen sites in the soot and results in denser and better adhesion to the substrate. The treatment also makes the peak of the carbon nano-features more rounded and decreases overall nanoscale cavities, which results in transition from Cassie-Baxter to Wenzel state. Consequently, the fluorocarbon treatment forms a fluorine-based layer and changes the wetting back to the Cassie-Baxter state.

Later, we studied the anti-biofouling property of three types of our coating namely as diamond-like carbon, fluorocarbon-functionalized diamond-like carbon, and carbon soot. The coatings were deposited on three groups of 5 MHz quartz crystal microbalance (QCM) and then immersed in aqueous suspensions of four biofoulants including red *Polysiphonia*, green *Scenedesmus* algae,

cells of diatom *Navicula*, and filamentous cyanobacteria *Oscillatoria*. The analysis of the resonance frequency of the QCMs revealed that our superhydrophobic soot coating is able to completely prevent the biofouling [48].

2.4 Conclusions

This chapter explained how utilizing a chimney in the combustion process of rapeseed oil results in a superhydrophobic carbon soot coating that can be applied on any type of solid substrates, even with low thermal stability, with no need to any stabilizer. The chimney reduces the oxygen level during the combustion and amends the chemical bonds in the soot, which leads to a denser and fused precipitation of carbon particles. Moreover, it was shown that the modified coating retains its superhydrophobicity up to ~ 300 °C. The mechanical stability of the modified soot coating can be amplified by chemical treatment in such way that it withstand water jet with a reckless impact velocity of ~ 25 m/s. How this chemical functionalization alters the wettability and surface energy of the coating is investigated in Chapter 3.

Chapter 3 Rolling Viscous Drops on Non-wettable Ribbed Surfaces

3.1 Introduction

This chapter is almost a duplication of my article published in *Physics of Fluids* in 2018 [44]. Liquid-solid interaction has been studied for decades because of its involvement in many applications such as lubrication [67, 68], surface cooling [69, 70], surface cleaning [13, 14], and liquid transportation [71, 72]. Sometimes it is desired to prevent this interaction in certain applications; hence, the fabrication and implementation of so-called non-wettable surfaces has been widely investigated by scientists over the past several years. As mentioned earlier, wettability of a solid surface associated with a particular liquid is assessed through the contact angle (θ) of the liquid drop deposited on the solid substrate [7]. The higher the contact angle, the more non-wettable the surface is. By definition, the surface is called superhydrophobic or superoleophobic if it makes a contact angle of greater than 150° with water or oil, respectively. It has been illustrated that such non-wettable surfaces demonstrate some exceptional properties such as anti-biofouling [48], anti-corrosion [13], drag-reduction [10], and self-cleaning [14, 73]. Most of these applications involve the movement of droplets on the surface that may not be straight.

Motion of a liquid drop on an inclined solid substrate generated by its own weight is a combination of rolling and sliding depending on the viscosity of the drop as well as the wettability of the substrate [23-25]. In fact, for high viscous liquids, the motion would be pure rolling with no slip-length [24] and if the liquid partially wets the surface, the larger drops run faster [25]. For the case of large viscosity and non-wettable surfaces, Mahadevan and Pomeau claimed that the drop rolls down at an equilibrium descent velocity (V) [26]. They studied the motion of a liquid drop with viscosity (μ), surface tension (γ), density (ρ), and radius (R) on a tilted plane at an angle of $\alpha < 1$ radian (i.e., $< 57^\circ$) and proposed a scaling model to predict V by balance between viscous

dissipation and the rate of decrease of the gravitational potential energy. Afterwards, Richard and Quere experimentally examined this scaling model and showed for drops with radii smaller than the capillary length $\kappa^{-1} = \sqrt{\frac{\gamma}{\rho g}}$ (g is the gravitational acceleration), the smaller the drop, the faster it rolls (something in contrast with the case of partially-wettable surface). However, the provided equations were not able to accurately explain their presented results [22]. They also showed that the descent velocity is independent of the radius of the drop for $R > \kappa^{-1}$. In addition, Aussillous and Quere obtained a liquid marble by rolling a liquid drop (mixture of water and glycerol with $\mu > 200$ mPa.s) in a hydrophobic powder and then studied its motion on an inclined solid surface [74]. Since the contact angle of the viscous liquid marble was close to 180° , they expressed the same explanation for the motion as Mahadevan and Pomeau did [26]. However, they showed that their equations were valid only for $\alpha < 10^\circ$.

The current chapter presents a modified scaling model to predict the descent velocity of a rolling viscous drop much more accurately up to $\alpha \sim 45^\circ$. It is worth noting that the water motion, which is a mixture of rolling and sliding, should not be confused with the objective of the current study, i.e., rolling of glycerol (with a viscosity 1000-fold greater than that of water). Moreover, we show that a numerical coefficient is crucial in the related equations and must be considered because it reflects the non-wettability (i.e. contact angle) of the surface, something that is missing in the aforementioned studies. To do this systematically, we carefully examined the motion of glycerol drops with different radii rolling on a macroscopically smooth non-wettable surface, made of functionalized soot, at 6 different tilting angles. We also show that the drop rolls $\sim 27\%$ faster if the tilting non-wettable surface is not macroscopically smooth, but contains cylindrical ridges of hundreds of micrometers in diameter (ribbed surface). This phenomenon might be due to the

preserved air layers underneath the drop, which means this surface pattern/morphology (combination of nano/micro and macro roughness) may be useful in drag-reduction applications and self-cleaning surfaces.

3.2 Experimental Method

3.2.1 Sample Preparation

Soot has been used in many studies as a superhydrophobic coating layer, yet the deposition and stabilizing processes have been varied [47, 57-60]. In this study, we used the chimney-modified method of deposition [47] and functionalized the soot afterwards. In fact, exposing our solid substrates to the black fumes generated from our oil-based combustion unit [49], at an air flow rate of 0.0031 m³/min, provided a uniform layer of untreated soot coating. To Improve the wettability and strength of the as-synthesized soot, we functionalized it using a method that was composed of dipping in ethanol (99%, Sigma-Aldrich, USA) for 5s (ethanol treatment), followed by perfluorocarbon treatment consisting of immersion in a solution of 12.5 wt.% perfluorocarbon (Granger's Performance Proofer, Granger's Ltd., UK) and 87.5 wt.% de-ionized (DI) water for 10 min.

It has been shown that for the relatively-thick soot layers, synthesized using the method that we previously developed and used here, the material of the solid substrate (glass, polymer or metal) has no effect on the wettability and characterization of the coating [47]. As such, the solid substrates used for wetting characterization of the coating were 25 × 25 mm glass slides (Fisher Scientific, USA). For the rolling-drop experiments, two rectangular prisms of 50 × 50 × 10 mm were printed in polyethylene terephthalate glycol-modified (PETG) using an extruder-type 3D printer (Ultimaker 2, Netherlands) with a nozzle of 0.4 mm in diameter and the speed of 12 mm/s.

One of the specimens was used with its original surface finish after printing, fully covered with cylindrical ridges of $2b = 300 \mu\text{m}$ in diameter (ribbed surface) with the resolution of about 5 microns. The other one was polished with 600 and 1200 grit sand papers (Allied High Tech Products Inc., USA) to obtain a surface with no macroscopic-sized textures, which we call smooth surface. Prior to the soot deposition, both surfaces were cleaned with a detergent and then sonicated in water-ethanol solution for 30 minutes.

Four different liquids, water, diiodomethane, glycerol, and olive oil were used for studying the wettability and surface energy of our non-wettable coating. For the rolling droplet experiments only glycerol, whose viscosity is sufficiently high, was used.

3.2.2 Surface Free Energy Examination

Soot has previously been used as a template to fabricate superamphiphobic coatings [57]. The synthesis of such surfaces, however, includes chemical vapor deposition followed by calcination at 600°C , which constrains its applicability. The fabrication process of the functionalized soot presented here can be applied on any type of solid substrate even with low thermal stability such as plastic and wood. Recently, our research group has shown that ethanol treatment reduces the porosity and thickness of the soot layer so that its robustness improves significantly [66, 75]. Here we examined how ethanol and perfluorocarbon treatments change the surface free energy and water/oil repellency of the soot.

Theoretically, contact angle (θ) of a sessile liquid drop on a solid surface correlates the surface free energy of the solid (γ_s), the energy of the solid-liquid interface (γ_{sl}), and the surface tension of the liquid (γ_l) through the Young's equation (Equation 3.1a) [5]. The θ and γ_l can

experimentally be measured, which we did using a Drop Shape Analyzer (DSA-25E, KRUSS, Germany); thus, having an additional equation for γ_{sl} makes it mathematically possible to determine the γ_s . It is known that γ_s and γ_l are the summation of their own dispersive and polar components, denoted with superscript d and p in Equations (3.1b-c), respectively [76-78]. The permanent dipoles, induced dipoles and hydrogen bond forces are responsible for the polar component, whereas the non-polar van der Waals forces are the origin of the dispersive component [78].

$$(a) \gamma_s - \gamma_{sl} = \gamma_l \cos\theta \quad (b) \gamma_s = \gamma_s^d + \gamma_s^p \quad (c) \gamma_l = \gamma_l^d + \gamma_l^p \quad (3.1)$$

The solid-liquid interaction, i.e. γ_{sl} , is directly related to the extent of polarity and non-polarity of the solid and the liquid. Using the geometric mean, Owens and Wendt proposed an equation for γ_{sl} [76]. Alternatively, Wu claimed that for low-energy surfaces, the harmonic mean should be used to obtain γ_{sl} , as expressed in Equation (3.2) [77].

$$\gamma_{sl} = \gamma_s + \gamma_l - 4 \frac{\gamma_s^d \gamma_l^d}{\gamma_s^d + \gamma_l^d} - 4 \frac{\gamma_s^p \gamma_l^p}{\gamma_s^p + \gamma_l^p} \quad (3.2)$$

Substituting Equation (3.2) into Equation (3.1a) yields Equation (3.3)

$$\frac{\gamma_l(1+\cos\theta)}{4} = \frac{\gamma_s^d \gamma_l^d}{\gamma_s^d + \gamma_l^d} + \frac{\gamma_s^p \gamma_l^p}{\gamma_s^p + \gamma_l^p} \quad (3.3)$$

According to Equation (3.3), the dispersive and polar components of the solid surface can be calculated with measuring the contact angle of two liquids whose γ_l^d and γ_l^p are known. Here, a non-polar liquid (diiodomethane, Fisher Scientific, USA) and a relatively polar one (water), whose surface tension components are presented in Table 3.1 [78], were used to calculate the surface

energy of the untreated soot (as-synthesized), the ethanol-treated soot, the perfluorocarbon-treated soot and the functionalized (ethanol-treated followed by perfluorocarbon treatment) soot coatings.

Table 3.1. Surface tension components of the liquids used to evaluate surface energy of the four solid surfaces studied. We have measured the total surface tension values (second column) in our experiments, while their contributing components (third and fourth columns) have been estimated by consulting Ref. [78].

Liquid	$\gamma_l(\text{mN/m})$	$\gamma_l^d(\text{mN/m})$	$\gamma_l^p(\text{mN/m})$
Water (H ₂ O)	72.8	21.8	51.0
Diiodomethane (CH ₂ I ₂)	48.5	48.5	0.0

3.2.3 Rolling Drop Setup

Glycerol (99%, Acros Organics, USA) of density $\rho = 1261 \text{ kg/m}^3$, surface tension $\gamma = 64.6 \pm 0.1 \text{ mN/m}$ and viscosity $\mu = 1076 \pm 5 \text{ mPa.s}$ at 23 °C was used as the viscous liquid. The surface tension and viscosity were measured by means of our DSA-25E and a Rheometer (MCR301, Anton Paar, USA), respectively. Using a precisely-controlled automated syringe and calibrated tips, glycerol drops of volume 6-116 μL were formed with $< 5\%$ error. The drops were gently placed on the non-wettable smooth and ribbed surfaces tilted at 6 different angles ($\alpha \sim 5^\circ\text{-}45^\circ$) and allowed to roll down under the influence of their own weights. The tilting angles were made by a stepper motor controlled by an Arduino microcontroller and were confirmed by a digital level (DWL-80e, Digi-Pas, USA).

Using a high-speed camera (Phantom Miro ex2, Ametek, USA), the motion of the glycerol drops was filmed at 1200 frames per second (fps) at first. After analyzing the videos via Tracker, open-source computer software, it was found that 1200 fps was unnecessarily high; therefore, the frame rates were adjusted accordingly from 120-600 fps. Each test was repeated three times and the measured velocities fluctuated $< 5\%$. All the experiments were conducted at $\sim 23^\circ\text{C}$ and $\sim 38\%$ relative humidity. Figure 3.1a shows the schematic diagram of the experimental setup as well as

the roughness of the functionalized soot coating and Figure 3.1b shows the actual setup used during the experiments.

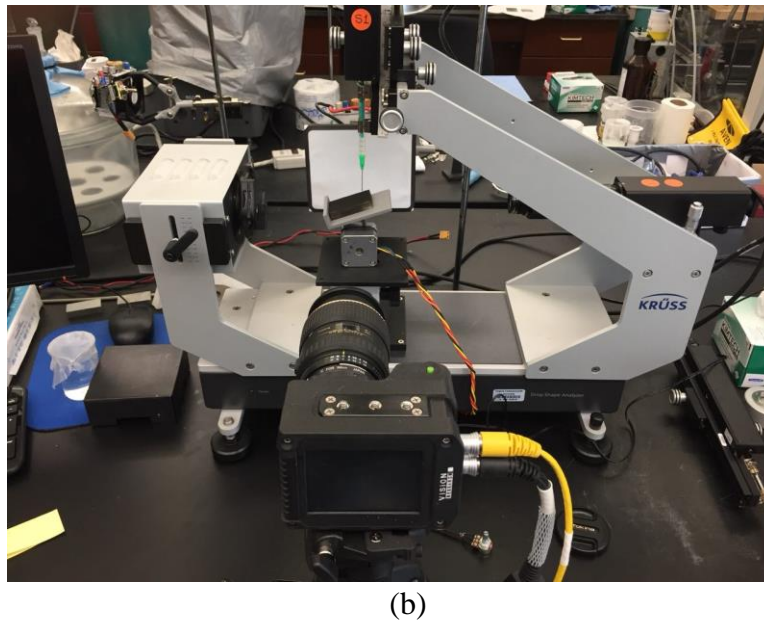
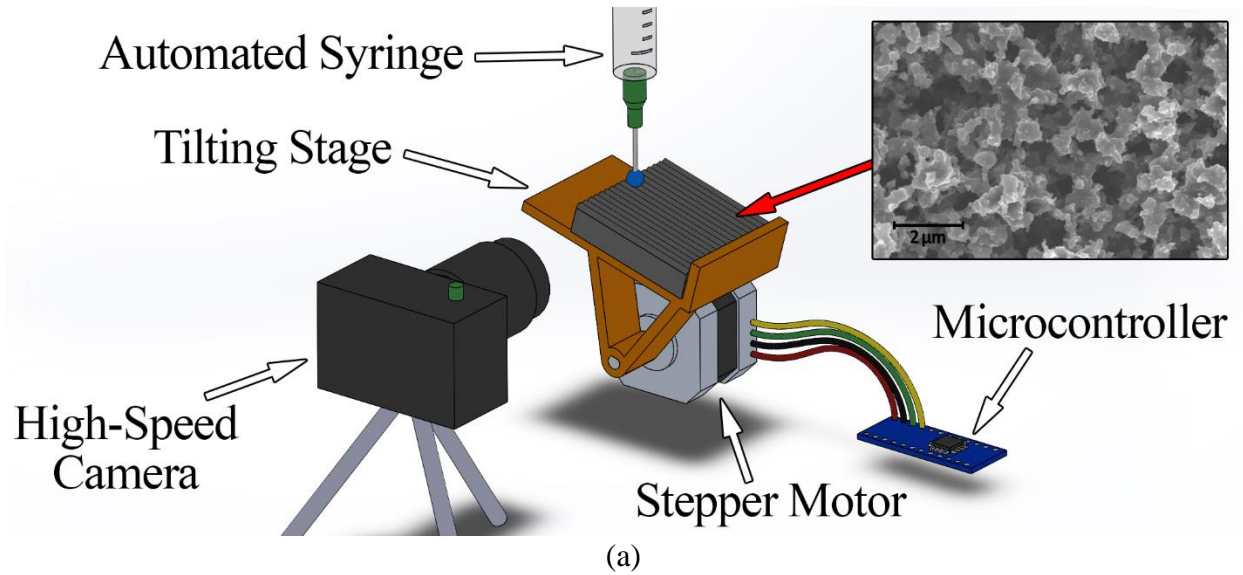


Figure 3.1. (a) The schematic diagram of the experimental setup. The inset is a SEM image of a functionalized soot coating that illustrates its nano-/micro-sized roughness. (b) The actual setup used for the tests.

3.3 Results and Discussion

3.3.1 Wettability and Surface Free Energy of the Soot-based Coatings

Table 3.2 states the measured contact angles of water ($\rho = 1000 \text{ kg/m}^3$, $\gamma = 72.8 \pm 0.2 \text{ mN/m}$), diiodomethane ($\rho = 3322 \text{ kg/m}^3$, $\gamma = 48.5 \pm 0.3 \text{ mN/m}$), glycerol ($\rho = 1261 \text{ kg/m}^3$, $\gamma = 64.6 \pm 0.1 \text{ mN/m}$), and olive oil ($\rho = 930 \text{ kg/m}^3$, $\gamma = 33.1 \pm 0.1 \text{ mN/m}$) on the four solid substrates investigated. It should be noted that drops with a volume of $\sim 5 \text{ }\mu\text{L}$ were used for water, glycerol, and olive oil. For diiodomethane, however, $\sim 1 \text{ }\mu\text{L}$ drops were used due to its high density and low surface tension. The contact angles were measured on the macroscopically-smooth samples (without ribs).

Table 3.2. Contact angle values of water, diiodomethane, glycerol and olive oil on untreated soot, ethanol-treated soot, perfluorocarbon-treated soot and functionalized soot.

Solid Surface	Water	Diiodomethane	Glycerol	Olive oil
Soot (untreated)	$155.1 \pm 1.5^\circ$	$\sim 0.0^\circ$	$147.1 \pm 2.4^\circ$	$\sim 0.0^\circ$
Ethanol-treated soot	$147.7 \pm 2.4^\circ$	$\sim 0.0^\circ$	$127.8 \pm 0.9^\circ$	$\sim 0.0^\circ$
Perfluorocarbon-treated soot	$168.1 \pm 1.4^\circ$	$103.9 \pm 4.5^\circ$	$167.6 \pm 1.8^\circ$	$153.8 \pm 1.1^\circ$
Functionalized soot	$166.8 \pm 0.9^\circ$	$105.0 \pm 4.4^\circ$	$169.1 \pm 1.3^\circ$	$157.5 \pm 0.9^\circ$

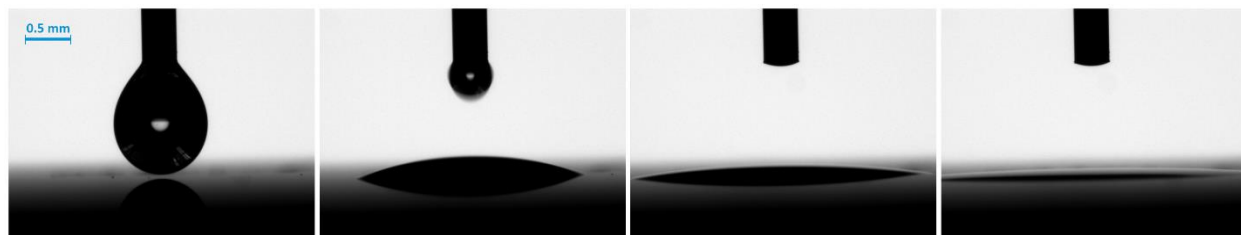


Figure 3.2. The snapshots from left to right depict how a $1 \text{ }\mu\text{L}$ droplet of diiodomethane (CH_2I_2) spreads on untreated soot. The spreading occurs in less than 1 second. Olive oil also spreads similar on both untreated and ethanol-treated soot coatings.

Since diiodomethane and olive oil (non-polar liquids [78, 79]) spread instantly on both the soot and ethanol-treated soot coatings (Table 3.2 and Figure 3.2), it is concluded that the ethanol treatment does not change the non-polarity of the soot. However, since the ethanol treatment makes the soot denser and reduces its porosity [66, 75], the contact angles of water and glycerol (polar liquids [80]) on the ethanol-treated soot are smaller than those on the untreated soot. Moreover, Figure 3.3a shows how a 5 μ L water drop suspended from a needle (of 0.2 mm inside diameter) cannot be detached by the untreated soot, while the ethanol-treated soot detaches the drop from the needle easily (Figure 3.3b). This also illustrates that this treatment alters the wetting state of the soot from Cassie-Baxter to Wenzel regime.

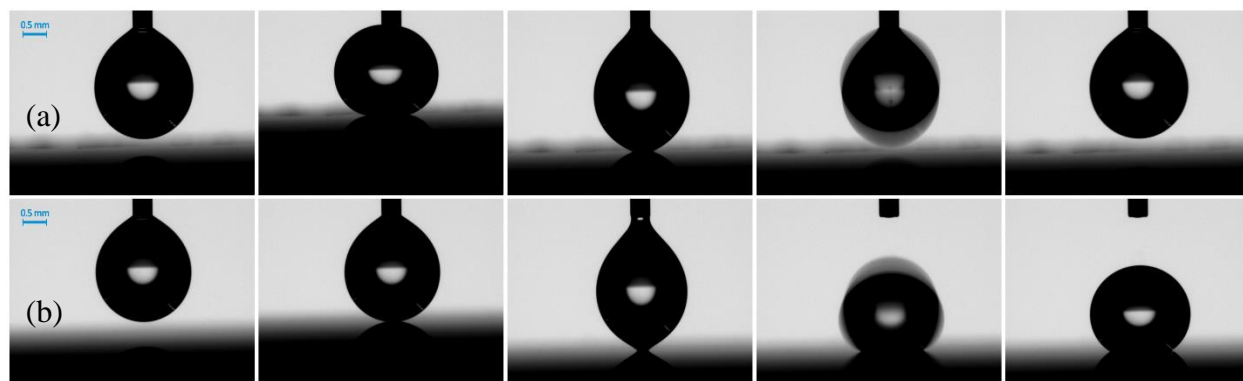


Figure 3.3. The top row (a) from left to right shows that the un-treated soot cannot detach a 5 μ L water drop from the needle of 0.2 mm inside diameter due to its Cassie-Baxter state of wetting. The bottom row (b) illustrates how the same size drop sticks to the ethanol-treated soot as soon as it touches the surface (Wenzel state).

According to the data of Table 3.2, the interaction with perfluorocarbon solution drastically changes the wettability of the coating so that it repels both polar and non-polar liquids, which means that the surface energy of the coating must have become very low. The surface energies of the solid surfaces were calculated using Equation (3.3) and casting the mean value of the contact angles of water and diiodomethane presented in Table 3.2 and their surface tension components listed in Table 3.1. In fact, Table 3.3 shows that the calculated surface energy reduces drastically

from 37.9 mJ/mm² for the soot and 38.6 mJ/mm² for the ethanol-treated soot to 5.2 mJ/mm² for perfluorocarbon-treated soot and 5.0 mJ/mm² for functionalized soot, respectively, due to the generation of a fluorine-based layer on top of the coatings [66, 75]. Such a low surface energy results in the oil repellency of the functionalized soot coating with the contact angle hysteresis of ~0.9° for glycerol and makes the surface a great candidate for the rolling drop test (no liquid pinning).

Table 3.3. The results of surface energy calculations for the different types of soot-based coatings. The values were obtained using Equation (3.3) and the data presented in Table 3.1 and Table 3.2.

Solid Surface	γ_s (mJ/mm ²)
Soot (untreated)	37.9
Ethanol-treated soot	38.6
Perfluorocarbon-treated soot	5.2
Functionalized soot	5.0

3.3.2 Rolling Viscous Drop

The motion of glycerol ($\rho = 1261 \text{ kg/m}^3$, $\gamma = 64.6 \pm 0.1 \text{ mN/m}$, and $\mu = 1076 \pm 5 \text{ mPa.s}$) drops on the polished PETG sample (smooth surface) coated with functionalized soot and inclined at 6 different angles ($\alpha = 5^\circ$ - 45°) was investigated here in order to find the modified scaling model for predicting their descent velocities. Considering the case of a small liquid drop ($R < \kappa^{-1}$) sitting on a horizontal non-wettable solid surface, the capillary forces endeavor to keep the spherical shape of the drop whereas gravity tends to increase the solid-liquid contact area. Mahadevan and Pomeau [26] stated that the radius of the contact disk (l) is related to the radius of the drop (R) and the displacement of the center of mass of the drop (δ) due to its weight as

$$l \approx \sqrt{R\delta} \quad (3.4)$$

As the drop is almost spherical except in the vicinity of the substrate, they explained geometrically that the increase in the surface area of the drop due to flattening because of contact with the substrate is in the order of $\Delta s \approx l^4/R^2$ [26]. Therefore, balancing the increase in the surface energy $\gamma\Delta s \approx \gamma l^4/R^2$ and the decrease in the potential energy of the drop $\rho R^3 g \delta$ yields the expression for δ as

$$\delta \approx \rho g R^3 / \gamma \quad (3.5)$$

Finally, substituting Equation (3.5) into Equation (3.4) results in

$$l \approx R^2 / \kappa^{-1} \quad (3.6)$$

where κ^{-1} is capillary length, as mentioned earlier ($\kappa^{-1} = \sqrt{\frac{\gamma}{\rho g}}$). For the case of $R > \kappa^{-1}$, gravity dominates the surface tension and flattens the drop to a pancake shape. Since the thickness of the pancake (w) scales with the capillary length (κ^{-1}), conservation of mass ($l^2 w \sim R^3$) concludes that the radius of the contact scales as

$$l \approx R^{3/2} / \kappa^{-1/2} \quad (3.7)$$

One approach to estimate the numerical coefficients of Equations (3.6) and (3.7), which have to be the same, is to use the conservation of mass for flattened heavy drops. It is well established that the thickness of the flattened drop due to its own weight is: $w = \sqrt{2(1 - \cos\theta)} \kappa^{-1}$ [22, 37, 81]. For non-wettable surfaces, where $\theta > 150^\circ$, the height can be considered $w \approx 2\kappa^{-1}$. Casting this value in the conservation of mass, which is $\rho \pi l^2 w = \rho \frac{4\pi}{3} R^3$, results in

$$l \approx \sqrt{\frac{2}{3} \frac{R^3}{\kappa^{-1}}} = 0.81 R^{3/2} / \kappa^{-1/2} \quad (3.8)$$

Moreover, it has been reported that numerically solving the Laplace equation yields a numerical coefficient in the order of 0.8 [74]. We measured the contact radius of the glycerol drop on the smooth (non-wettable) surface, which was horizontally oriented, as a function of its initial radius. The best numerical coefficient for Equations (3.6) and (3.7) to fit our data was found to be 0.79 using a least-squares fit of the data shown in Figure 3.4, thus the contact radius can be calculated from Equation (3.9) for our experiments.

$$\begin{cases} l = 0.79 R^2 \kappa & \text{for } R < \kappa^{-1} \\ l = 0.79 R^{\frac{3}{2}} \kappa^{\frac{1}{2}} & \text{for } R > \kappa^{-1} \end{cases} \quad (3.9)$$

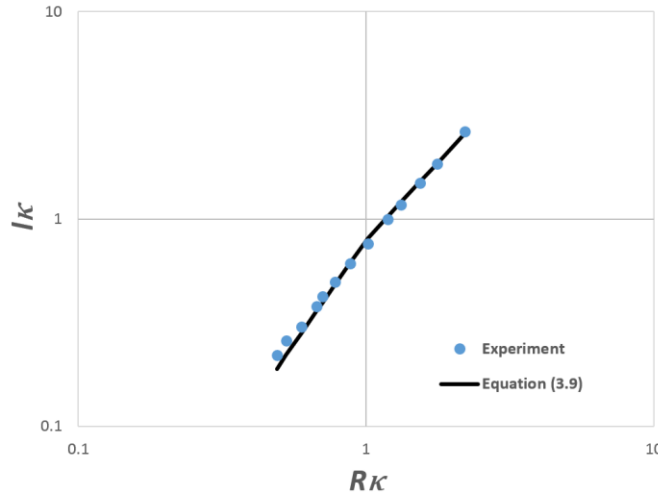


Figure 3.4. The radius (l) of the solid-liquid contact area for glycerol drops of different initial radii (R) sitting on the horizontal macroscopically-smooth, non-wettable surface. Both values were normalized with the capillary length $\kappa^{-1} = \sqrt{\gamma/\rho g} = 2.27$ mm.

For the case of small drops ($R < \kappa^{-1}$) rolling down an inclined non-wettable surface with Stokes flow ($Re = \rho V R / \mu < 1$), low velocity ($Ca = \mu V / \gamma < 1$), and little change in the spherical shape of the drops, Mahadevan and Pomeau [26] claimed that the rate of decrease in the gravitational

potential energy (LHS in Equation 3.10) balances with the viscous dissipation (RHS in Equation 3.10). This happens in the portion of the volume of the rolling drop influenced by the contact region, $\sim l^3$, as

$$\rho R^3 g V \sin \alpha \approx \mu \left(\frac{V}{R}\right)^2 l^3 \quad (3.10)$$

Solving Equation (3.10) for V and substituting Equation (3.6) in it, Richard and Quere came up with an equation to predict the descent velocity of a rolling droplet [22]. Using their equation, which is related to $\sin \alpha$ and κ^{-1} , and plotting the normalized values of the measured velocities of the rolling drops with different radii for the varied tilting angles of our study (Figure 3.5), we noticed that the data did not correlate on a single plot, similar to what Richard and Quere found in their study, but did not address. This means that a key factor has been missing in the related equations and the scaling model needs to be modified.

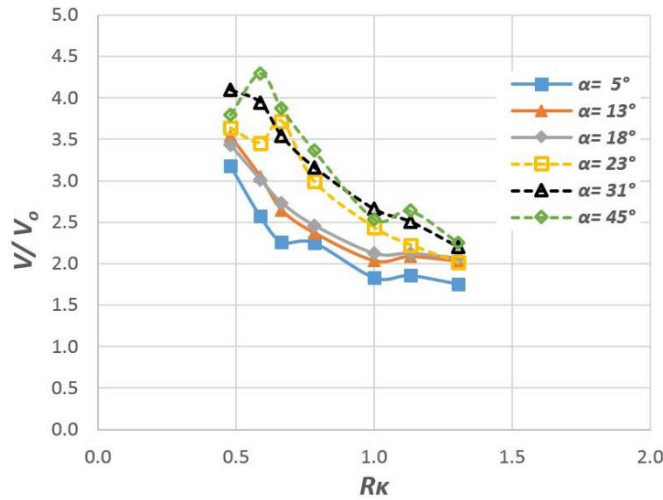


Figure 3.5. The variation of the measured velocity normalized by $V_o = \frac{2(1-\cos\theta)g\sin\alpha}{3\mu}$ as a function of drop radius normalized by κ^{-1} . The equation for V_o is taken from Richard and Quere's work [22]. It can be seen that the diagrams are sporadic for different tilting angles (α) and do not collapse in a single plot of $\frac{V}{V_o} \approx \frac{\kappa^{-1}}{R}$, similar to what

Richard and Quere reported in their study. However, the results follow the trend of the smaller the drop, the faster it rolls.

As explained earlier, Equation (3.5) for δ is obtained with the balance between the increase in the surface energy by $\gamma l^4/R^2 \approx \gamma \delta^2$ and the decrease in the potential energy of the drop by $\rho R^3 g \delta$ generated by its own weight. For a rolling drop on an inclined surface, the displacement of the center of mass caused by the *normal* component of gravity should be considered (see Figure 3.6), hence the reduction in the potential energy is $\rho R^3 g \delta \cos \alpha$. Consequently, $\delta \approx \rho g R^3 \cos \alpha / \gamma$ and

$$l \approx R^2 / \kappa^{*-1} \text{ where } \kappa^{*-1} = \sqrt{\gamma / \rho g \cos \alpha} \quad (3.11)$$

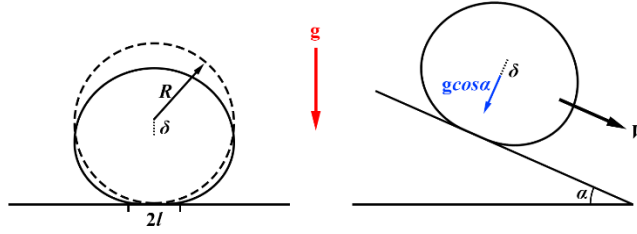


Figure 3.6. For the case of the rolling drop on a tilted surface at the angle of α , the δ is a consequence of the normal component of gravity to the surface.

The modified scaling model to predict the descent velocity of a rolling viscous drop on a non-wettable solid substrate tilted at an angle of α is obtained by combining Equations (3.10) and (3.11) as

$$V \approx \frac{\rho R^5 g \sin \alpha}{\mu l^3} = \frac{\gamma}{\mu} \frac{\kappa^{*-1}}{R} \tan \alpha \quad (3.12)$$

According to Equation (3.12), when the radius of the drop reaches the critical value of κ^{*-1} , the velocity reaches the value of $V_o = \frac{\gamma}{\mu} \tan \alpha$. Figure 3.7 shows that all the normalized velocities of the rolling drops (V/V_o) with respect to their normalized sizes ($R\kappa^*$) collapse into a single plot

with the numerical coefficient of 2.23 for the 6 different tilting angles tested in this work. The reason that our Equation (3.12) fits better with the experimental data is its dependence to $\tan\alpha$ and κ^{*-1} , whereas to $\sin\alpha$ and κ^{-1} as expressed in Refs. [22, 26, 74]. Moreover, since $V \propto \frac{1}{l^3}$, it can be speculated that the numerical coefficient for Equation (3.11) must have been $1/\sqrt[3]{2.23} = 0.77$, a value indeed close to what we found for Equation (3.9). Moreover, since the thickness (w) of a flattened heavy drop is independent of its size [22, 37, 81] and the velocity gradient scales as V/w in its entire volume $\propto R^3$ (instead of V/R and $\propto l^3$ for small drops in Equation 3.10), the velocity is independent of the radius of the drop for $R > \kappa^{*-1}$, similar to what has been reported in Refs. [22, 74].

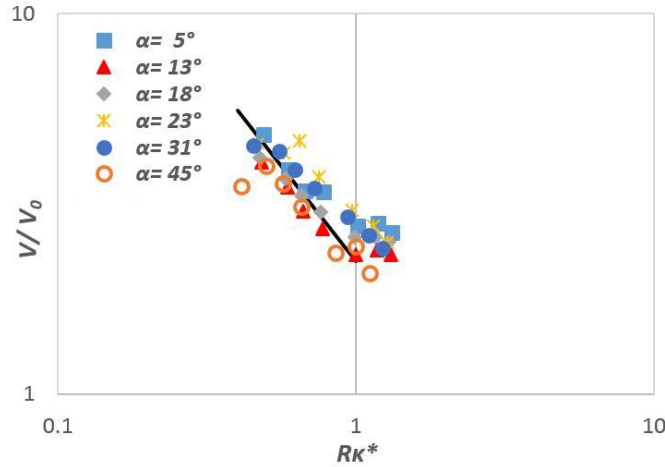


Figure 3.7. The normalized velocity of the rolling drops as a function of their normalized radii for the 6 different tilting angles $\alpha = 5^\circ$ - 45° tested in this study. The solid black line represents $\frac{V}{V_0} = 2.23 \frac{\kappa^{*-1}}{R}$ where $V_0 = \frac{\gamma}{\mu} \tan\alpha$.

We also measured the contact radius of the glycerol drops deposited on the non-wettable ribbed surface, fully decorated with cylindrical ridges of $2b = 300 \mu\text{m}$ diameter. It turns out that Equation (3.9) is also valid for this surface. Figure 3.8 illustrates how drops of different radii sit on (a) ribbed and (b) smooth samples.

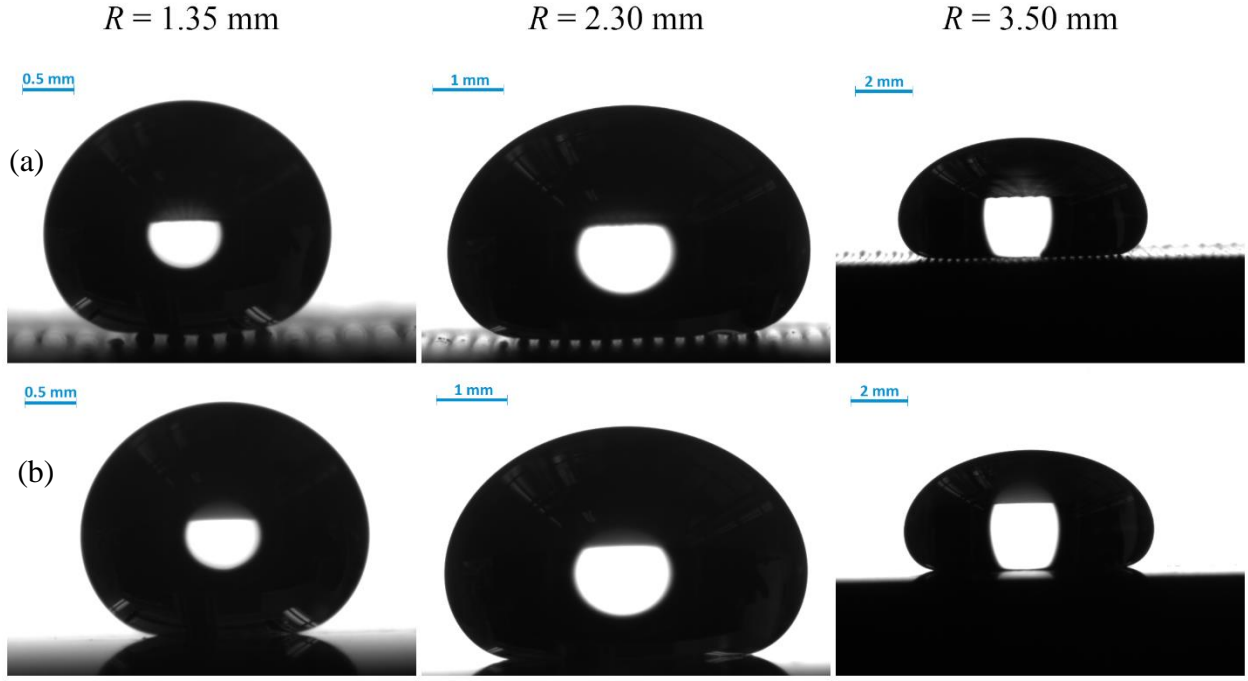


Figure 3.8. Glycerol drops of different radii deposited on (a) ribbed and (b) smooth surfaces. The capillary length for glycerol is ~ 2.27 mm.

The reflection of light underneath the drops on the ribbed surface illustrates that this surface pattern keeps macroscopic air pockets beneath the drop. When the drop rolls on such a surface, it encounters either the air pocket or the solid substrate. The relation between the probability of air (P_a) and the solid (P_s) surface being in contact with the rolling drop can be geometrically found from equations below.

$$(a) \frac{P_s}{P_a} = \frac{\frac{\pi b^2}{2}}{2b^2 - \frac{\pi b^2}{2}} = 3.7 \quad (b) P_s + P_a = 1 \quad (3.13)$$

Hence $P_s = 0.79$ and $P_a = 0.21$. This means that the area of contact between solid and liquid reduces to $\sim 79\%$ on such a surface pattern compared to the smooth one. As explained earlier, since viscous dissipation occurs in the part of the volume ($\sim l^3$) of the rolling drop influenced by the contact

region, the velocity is proportional to $\frac{1}{l^3}$. Considering the fact that this partial volume of the rolling drop on the ribbed surface is $\sim 79\%$ of that on the smooth one, the relation between the descent velocity of an equivalent-sized drop on ribbed (V_b) and smooth (V_s) surfaces will be $\frac{V_b}{V_s} \approx \frac{1}{0.79} \approx 1.27$. We measured the descent velocity of rolling glycerol drops on the ribbed surface under the same conditions as for the smooth surface. Figure 3.9 shows that the normalized velocities of the rolling drops (along the axis of the cylindrical ridges) concur well with the modified scaling model, yet with a numerical coefficient of 2.83, which is indeed 27% higher than that of the smooth surface. This means that the droplet rolls down faster on the ribbed surface due to the air pockets shown in Figure 3.8. It should also be mentioned that the drops almost instantly rolled at the associated descent velocity on the smooth surface, whilst their motions were slightly accelerated on the ribbed surface before reaching V_b especially for higher α . For instance, the 50 mm length of our samples was not long enough for the drops to reach an equilibrium descent velocity when they were rolling along the ridges at a 31° -tilted angle, thus the data have not been presented here.

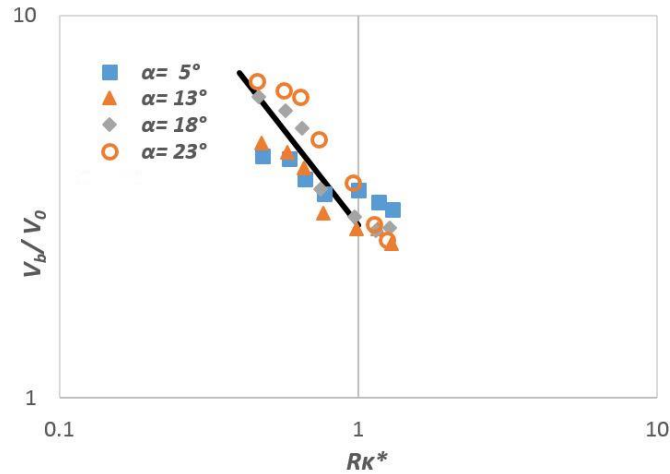


Figure 3.9. The plot depicts the normalized velocity of the rolling drops versus their normalized radii on the ribbed surface for varied tilting angles (α). The solid black line represents $\frac{V_b}{V_0} = 2.83 \frac{\kappa^{*-1}}{R}$ where $V_0 = \frac{\gamma}{\mu} \tan \alpha$.

In addition, we measured the descent velocity of the drops rolling perpendicular to the ridges and found a numerical coefficient of 2.53 for such rolling as shown in Figure 3.10. This value is still 13% higher than that of the smooth surface, but not comparable to 27% that was obtained for the case of rolling droplets along the ridges. This may be attributed to the fact that when the drop rolls perpendicular to the ridges, the ridges play a barrier role and hinder the motion [82].

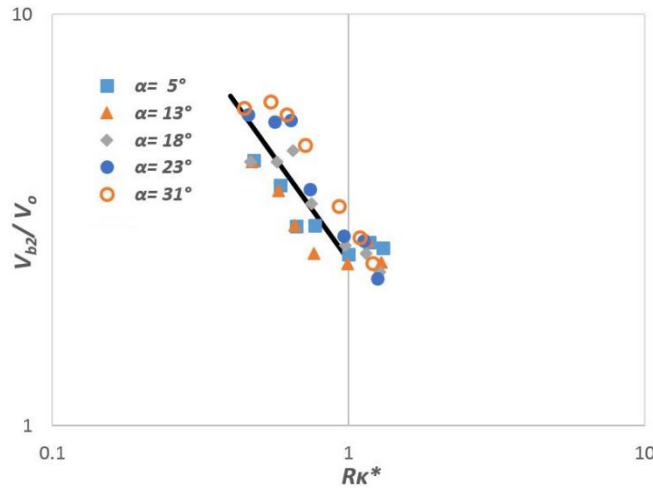


Figure 3.10. The plot shows the normalized velocity of glycerol drops rolling down, perpendicular to ridges, on the ribbed surface. The velocities are normalized by $V_o = \frac{\gamma}{\mu} \tan \alpha$ and the solid line represents the best fit for the data as $\frac{V_{b2}}{V_o} = 2.53 \frac{\kappa^{*-1}}{R}$.

Interestingly, we found that the skin patterns of a human being's palm, the sole of the foot, and the finger print look similar to the ribbed pattern as shown in Figure 3.11. This similarity, along with the faster motion of liquid drops on the ribbed surface, shows that this surface pattern may be useful in designing enhanced self-cleaning surfaces.

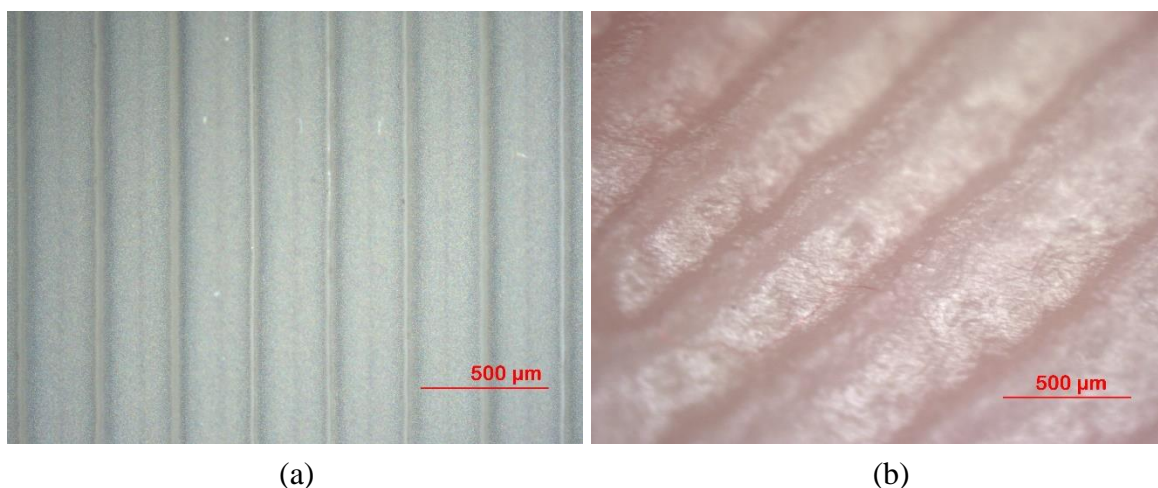


Figure 3.11. The image of (a) ribbed surface coated with functionalized soot and (b) skin pattern of the finger tip, taken using a Axio Lab optical microscope (Zeiss, Germany).

3.4 Conclusions

In this chapter, first the wettability of chimney-modified soot coating was investigated by measuring the contact angles of polar (water and glycerol) and non-polar (diiodomethane and olive oil) liquids before and after its interaction with ethanol and perfluorocarbon solutions. It was shown that the ethanol treatment increases the surface energy of the soot, yet does not alter its non-polar nature. Moreover, the perfluorocarbon treatment generates a fluorine-based layer on top of the soot and reduces its surface energy down to $\sim 5.0 \text{ mJ/mm}^2$. This functionalized soot coating with such a low surface energy demonstrated oil repellency with a contact angles of $\sim 157.5^\circ$ for olive oil and $\sim 169.1^\circ$ for glycerol.

Second, the motion of glycerol drops with different sizes rolling down on the non-wettable smooth and ribbed surfaces at 6 different angles of tilt was studied and a modified scaling model was given to predict the descent velocity more accurately, Equation (3.12). The experimental results exhibited a good agreement with this modified scaling model, even for a tilting angle as high as $\sim 45^\circ$. Moreover, it was shown that the drops roll $\sim 27\%$ faster (along the ridges) on the ribbed

surface compared to the smooth one due to the preserved air pockets underneath the drops. This indicates that a ribbed surface pattern may be valuable in designing enhanced self-cleaning surfaces.

Chapter 4 Droplet Impact on Superhydrophobic Ribbed Surfaces

4.1 Introduction

This chapter is nearly a duplication of my paper published in *Journal of Colloid and Interface Science* [45], in which the impact of water droplets on the ribbed surfaces was studied systematically. When an inviscid drop like water strikes a superhydrophobic surface, on one hand, the Weber number ($We = \rho V^2 R_o / \gamma$, in which ρ , V , R_o and γ are density, impact velocity, radius and surface tension of the drop, respectively) defines the maximum spreading diameter of the pancake created at the end of the spreading stage [36], which means the faster the impact velocity, the larger the spreading diameter. On the other hand, the amount of time that the drop and the solid surface are in contact (contact time) scales with the inertial-capillary time scale [31-33], $\tau_o = \sqrt{\rho R_o^3 / \gamma}$, which means the contact time is independent of the impact velocity. Since the exchange of mass, momentum and energy between the solid surface and the drop occurs during the contact time [83], minimizing this time is beneficial in certain applications. As such, this study focuses on the dynamic behavior of a water drop impinging on a superhydrophobic surface with a specific surface pattern/morphology which indicates shorter contact time under certain conditions.

Conventionally, it was known that symmetric bouncing of a droplet on a non-wetting surface leads to the minimum contact time [23, 31-33]. In addition, if the drop does not penetrate into the surface asperities in this type of bouncing [84], the contact time (t_c) is restricted by the Rayleigh limit, $t_c / \tau_o \geq \pi / \sqrt{2} \approx 2.2$ [23, 31, 33, 34]. Recently, however, Bird *et al.* showed that altering mass distribution in the spreading stage can lower the contact time below this theoretical limit [39]. The asymmetry is introduced by a single ridge whose amplitude is comparable to, but less than, the thickness of the flattened drop ($\sim 150 \mu\text{m}$). They claimed that since the liquid film is thinner on top

of the ridge, it retracts faster and generates non-uniform velocity field which leads to a shorter contact. The drawback of this technique for reducing the contact time is that the drop must hit the macrotexture exactly in the center in order for this reduction to happen and this time shifts back to the contact time on the macroscopically smooth surface as the point of impact recedes into the distance of the spreading radius, which again depends on the impact velocity as mentioned earlier [39, 40]. To overcome this issue, we aim in the present study to fabricate superhydrophobic surfaces *fully decorated with cylindrical ridges of hundreds of micron radii* and investigate the behavior of impacting water drops on them. Therefore, here we examine how the contact time on such surfaces varies with the impact velocity, diameter of the ridges and size of the droplet. Our results show that in the intermediate impact velocity range, the ribbed surface exhibits 13% shorter contact time compared to the macroscopically smooth surface due to faster retraction. Moreover, the contact becomes shorter at high impact velocity because the flattened droplet splashes from the periphery.

4.2 Experimental Methods

4.2.1 Sample Preparation

The solid substrates, on which we deposited the superhydrophobic soot layer, were cubes fabricated using an extruder-type 3D printer (Ultimaker 2, Netherlands). In this technique, polyethylene terephthalate glycol-modified (PETG) filament (Maker Geeks 54548) is fed into a heated liquefier where it melts. The melted PETG is pushed out from a nozzle of 0.4 mm in diameter and generates a cylindrical layer when it is deposited on a previously solidified layer. The thickness of both layers is controlled by slicing software (Cura) that controls the extrusion

volume. The surface pattern that we used in this study (fully decorated with cylindrical ridges) is the ribbed surface finish of the 3D printed samples, as illustrated in Figure 4.1.

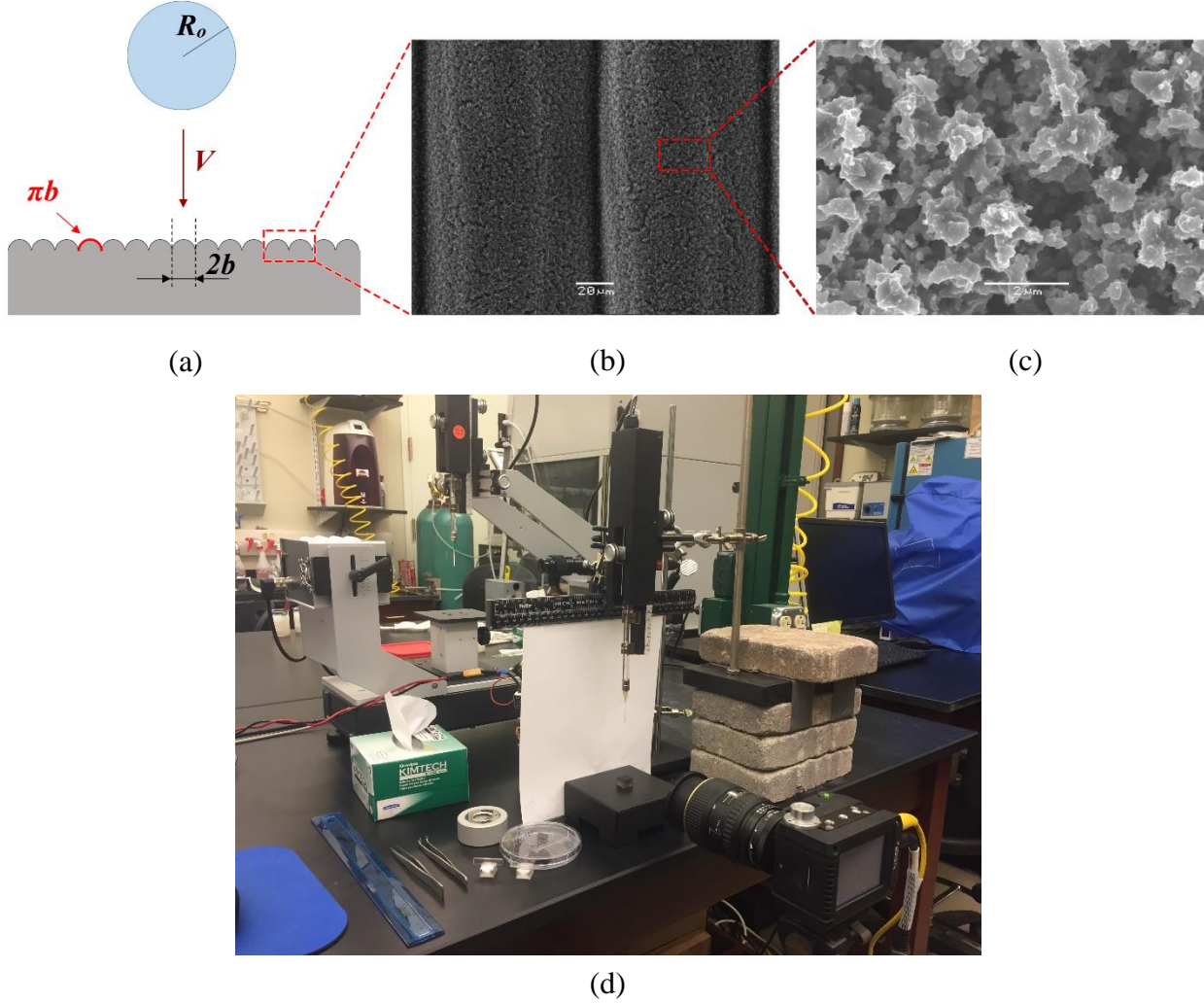


Figure 4.1. Experimental configuration and materials. (a) A water droplet of radius R_o impacts on a ribbed surface with macrotexture of diameter $2b = 0.1$ - 0.3 mm at velocity V . (b) Low and (c) high magnification SEM images of a cube printed at $2b = 0.1$ mm and coated with functionalized soot. (d) The actual setup used for conducting the experiments.

Prior to coating of the soot, PETG cubes ($15 \times 15 \times 10$ mm) printed with thickness layers (surface finish) of 0.1, 0.2 and 0.3 mm (with resolution of ~ 5 microns) were cleaned with a typical detergent and then inspected using an optical microscope (Axio Lab, Zeiss, Germany) confirming that there were no excrescences on their surfaces. The cubes were exposed for ~ 5 s over a black

fume rising from an inverted funnel used to control the input oxygen to the laminar diffusion flame of rapeseed oil [49]. The funnel was connected to an electric air pump and the supplying air flow was set at $0.0031 \text{ m}^3/\text{min}$ using a flow meter to obtain a uniform layer of stable soot. Such a short exposure time provided a thin layer of soot (thickness $\sim 7 \text{ }\mu\text{m}$ [47]) which did not alter the primary surface configuration. After the soot deposition, the samples were gently immersed in ethanol (99%, Sigma-Aldrich, USA) for 5s and then dried under a 250W heat lamp (Feit Electric, USA) for 5s, to evaporate the excessive ethanol with little increase in the temperature of the sample. Afterwards, the samples were submerged for 10 min in perfluorocarbon solution (Grangers Performance Proofer, UK) previously diluted with de-ionized (DI) water by a factor of 7. Next, each sample was dried under the heat lamp for 20s, which increased its temperature up to $\sim 38 \text{ }^\circ\text{C}$ and evaporated the chemical residues.

To prepare a macroscopically smooth sample, which we call smooth PETG from now on, a PETG cube was polished with 600 and 1200 grit sand papers (Allied High Tech Products Inc., USA) and then sonicated in DI-water for 30 minutes, to ensure that no debris from polishing remains on the surface. For the sake of comparison, the polished sample was coated with soot and chemically treated, following exactly the same procedure detailed above. Advancing and receding contact angles of DI-water on this sample (with no macrotecture) were found to be $166.2 \pm 2.6^\circ$ and $164.1 \pm 1.2^\circ$ (Figure 4.2), indicating the combination of a very high contact angle and low hysteresis, the required characteristics for fast water bouncing. These measurements were done using a Drop Shape Analyzer (DSA25E, Krüss, Germany).

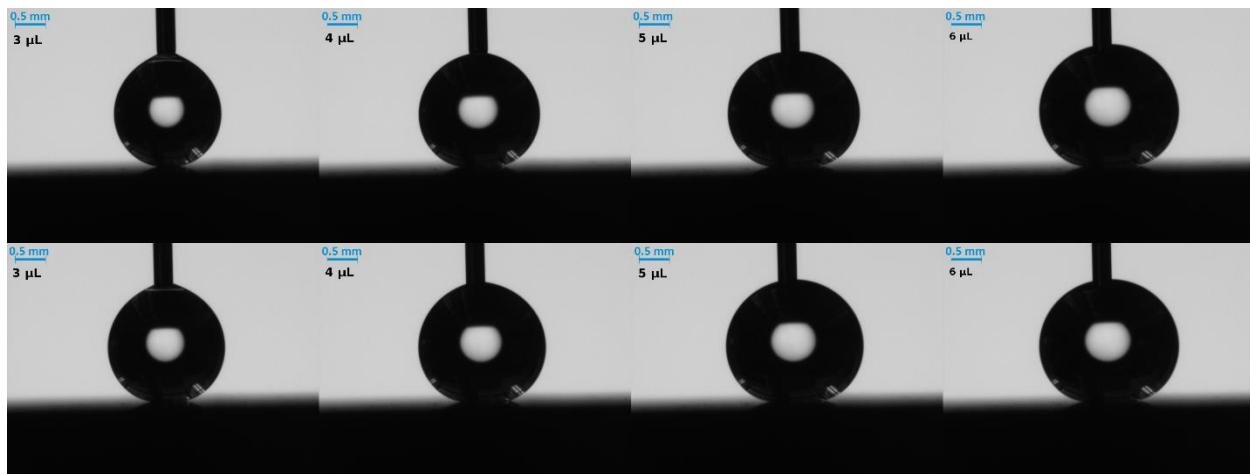


Figure 4.2. The top row from left to right shows that the volume of the water droplet advances from 3 μL to 6 μL while its advancing contact angle is $166.2 \pm 2.6^\circ$. The bottom row from right to left illustrates that receding contact angle of the surface is $164.1 \pm 1.2^\circ$, slightly lower than the advancing contact angle.

4.2.2 Experimental Setup

Our experiments consisted of releasing water drops of varied volumes from different heights onto the smooth and ribbed superhydrophobic samples. Impacts were filmed from above and from the side using a high-speed camera (Phantom Miro ex2, Ametek, USA), typically at 10000 frames per second (fps). The videos were analyzed via Tracker and the snap shots taken from them were analyzed with ImageJ software, developed at National Institute of Health. Water drops of density $\rho = 1000 \text{ kg/m}^3$ and surface tension $\gamma = 73 \pm 0.2 \text{ mN/m}$ were dosed from a precisely-controlled automated syringe. Using calibrated needles, we formed drops of volume 6-31 μL with $< 5\%$ error. The impact velocity varied between 0.4-2.2 m/s in 0.2 m/s increments by adjusting the release height from 8 to 247 mm. At each height, the impact velocity was also confirmed by measuring the rate of the change in the vertical position of the drop in last five frames prior to the impact. Each impact was repeated at least on three randomly-chosen spots of the sample at each velocity. For each averaged data, the error bars presented in the results show two standard deviations of the measured values.

4.3 Results and Discussion

Since our goal is to study the dynamic of impact in terms of contact time and spreading area of the flattened droplet, an expression that can precisely predict the maximum spreading radius (R_{max}) is required. For a viscous droplet, assuming that kinetic energy of the droplet $\sim \rho R_o^3 V^2$ mostly dissipates through the viscosity (μ) during the impact as $\sim \mu \frac{V}{\delta} R_{max}^3$, where δ is the thickness of the flattened droplet $\sim R_o^3/R_{max}^2$, yields that the Reynolds number ($Re = \rho V R_o / \mu$) governs the spreading radius as $R_{max} \sim R_o Re^{1/5}$ [85, 86]. On the other hand, for an inviscid droplet such as water, one approach to determining R_{max} can be assuming that the kinetic energy of the droplet transforms to the surface energy of the pancake $\sim \gamma R_{max}^2$. Such a scaling equation predicts that Weber number determines the spreading radius as $R_{max} \sim R_o We^{1/2}$. However, Clanet *et al.* showed that this approach is not accurate because some part of the initial kinetic energy is consumed to raise the internal kinetic energy of the droplet [36]. They proposed another scaling equation to predict R_{max} by balancing the hydrostatic and Laplace pressure. Since the droplet's initial velocity V decelerated to zero during the impact time R_o/V , the acceleration acting on the droplet is V^2/R_o , not the gravity [33, 36]. Therefore, the balance between the inertial hydrostatic pressure and the Laplace pressure, which defines the radius and thickness (δ) of the pancake, can be described as

$$\rho \frac{V^2}{R_o} \delta = \frac{\gamma}{\delta/2} \quad (4.1)$$

Combining Equation (4.1) with conservation of mass, $\rho \pi R_{max}^2 \delta = \rho \frac{4\pi}{3} R_o^3$, concludes

$$R_{max} = R_o \left(\frac{8}{9} We \right)^{0.25} \quad (4.2)$$

Despite the numerical factor of $\sqrt[4]{8/9} = 0.97$ in Equation (4.2), Clanet *et al.* found that their experimental data fit better with a factor of 1.07 [36]. This minor adjustment is attributed to the assumptions of the uniform deceleration and the cylindrical shape of the pancake [87]. They also defined an Impact number as $P \equiv We/Re^{4/5}$ to determine whether We or Re controls R_{max} [36]. For Impact number below unity, the impact is inviscid and $R_{max} \sim R_o We^{1/4}$, whereas for $P > 1$ the impact is viscous and $R_{max} \sim R_o Re^{1/5}$.

We measured the maximum spreading radii of droplets of 6, 9, 16 and 31 μL , whose initial radii were 1.1, 1.3, 1.6 and 2.0 mm respectively, impacting on the smooth PETG with the impact velocities mentioned earlier. The Reynolds number for our experiments changes between ~ 440 -3600 and the Impact number is $P < 0.13$ (for highest V and R_o), indicating the viscous dissipation is negligible for the impacts in this study. Figure 4.3 shows that the best scaling factor for the smooth PETG is 1.02, for the range of Weber number we used, i.e. ~ 2 -90. Therefore, Equations (4.3) and (4.4) can be used to find the radius and the thickness of the pancake for this sample.

$$R_{max} = 1.02 R_o We^{0.25} \quad (4.3)$$

$$\delta = 1.28 R_o We^{-0.5} \quad (4.4)$$

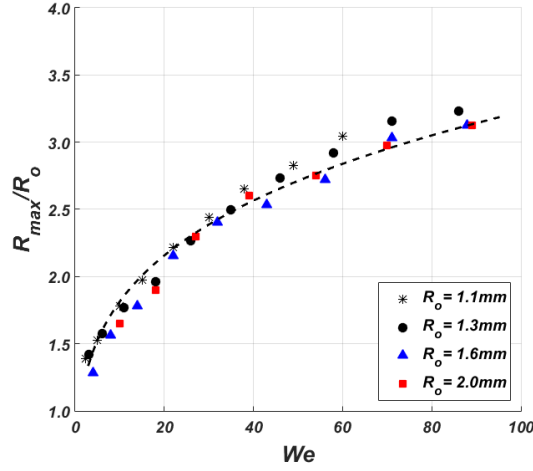


Figure 4.3. The ratio of the maximum spreading radius to initial radius of the droplet at different We . The ratio was measured experimentally for droplets of 6, 9, 16 and 31 μL impacting on the smooth PETG. Values of the initial radius of 6, 9, 16 and 31 μL droplets are 1.1, 1.3, 1.6 and 2.0 mm respectively. The maximum error bar is 0.05. The dashed line represents $1.02We^{0.25}$. This graph indicates that our measurements are sufficiently accurate and valid.

We start with analyzing the impact of 9 μL droplet on the ribbed (with $2b = 0.2$ mm, see Figure 4.1) and the smooth samples at different impact velocities. The impact on the ribbed surface is categorized into three distinguished regimes; low, intermediate and high impact velocity. For low impact velocity ($V < 1$ m/s), the droplet spreads and recoils circularly on both ribbed and smooth substrates. We hypothesized that the ribbed surface alters the mass distribution in the spreading stage and results in a lower contact time. In the low impact regime, however, no difference is observed and the ribbed surface interacts with the droplet as the smooth surface does, hence the contact times are the same for both surfaces. Figure 4.4a indicates the variation of the spreading radius (r) on the smooth PETG as well as the spreading length along (x) and perpendicular (y) to the cylindrical ridges on the ribbed surface during an impact at $V = 0.8$ m/s and $We \approx 11$. It can be seen that x , y and r follow the same trend as reported in literature for a bouncing drop on a superhydrophobic substrate at $We > 1$ [23], which is spreading symmetrically to a pancake of

radius R_{max} and thickness δ through a decelerated motion and then retracting at a constant velocity V_r [23, 42], expressed in Equation (4.5).

$$V_r = \sqrt{2\gamma/\rho\delta} \quad (4.5)$$

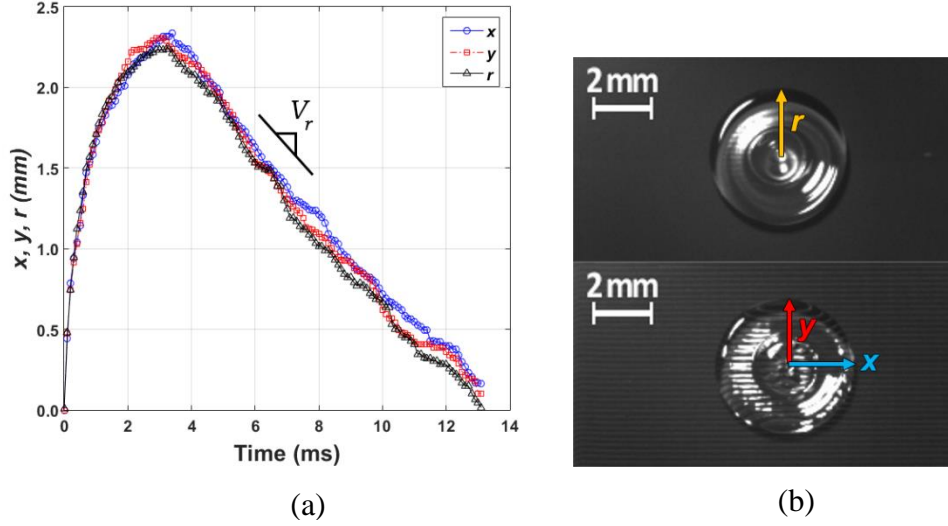


Figure 4.4. Water droplet of 9 μL impacting on ribbed ($2b = 0.2$ mm) and smooth surfaces at $V = 0.8$ m/s. The droplet symmetrically spreads to a circle on both samples. (a) The temporal variation of spreading radius (r), spreading length along (x) and perpendicular (y) to the cylindrical ridges during the impact. The data were acquired from side view videos. (b) Top view of the droplet at the end of the spreading stage on both samples; the circular pancake shape.

At higher impact velocity ($V > 1$ m/s), the expected asymmetry spreading starts to happen on the ribbed substrate. As shown in Figure 4.5a, for a 9 μL droplet impacting at $V = 1.2$ m/s and $We \approx 26$, the droplet spreads longer along the ridges (x) and adapts a quasi-elliptical shape, followed by non-circular retraction. The greater stretching in the x direction generates a shallower region in the middle. It was observed that the outer rim retracts faster along the ridges due to it being thinner and results in a retraction at non-uniform velocity. This is the reason that tail-like detachment is not seen for this substrate, and consequently the contact time decreases. The contact time is defined as the time the south pole of the droplet touches the substrate till the last point of contact leaves

the surface. It was determined from side view videos and found to be 11.4 ± 0.17 ms for the ribbed surface versus 13.5 ± 0.20 ms for the smooth one.

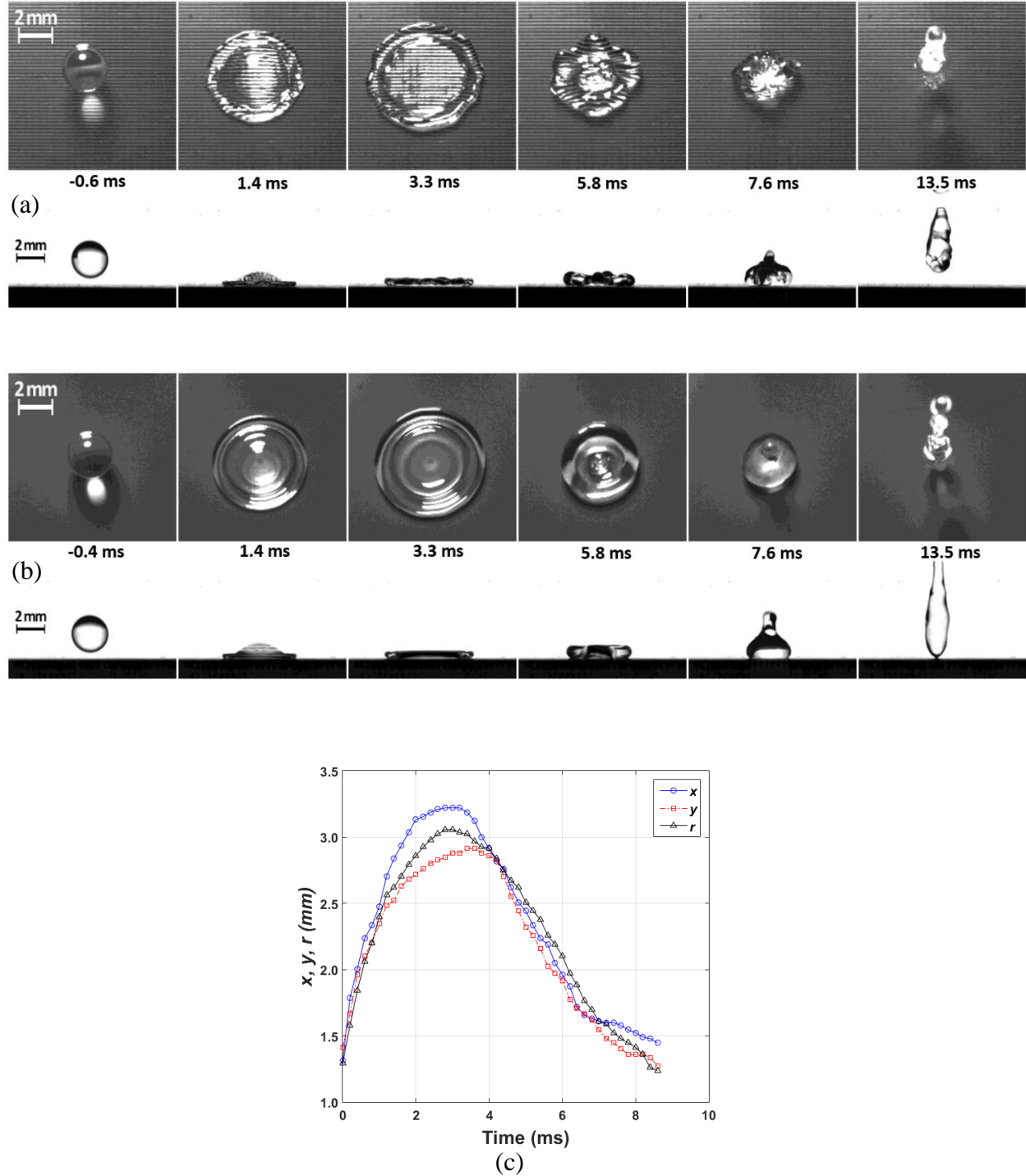


Figure 4.5. Impacting of a 9 μ L water droplet at $V = 1.2$ m/s on (a) ribbed sample of $2b = 0.2$ mm and (b) smooth PETG. Unlike on the smooth surface, the droplet spreads to a quasi-elliptical shape and retracts in a non-circular manner on the ribbed substrate, which results in reduced contact time. The contact time for the ribbed surface is

11.4±0.17 ms, compared to 13.5±0.20 for the smooth sample. (c) The graph illustrates the variation of x , y and r , as defined earlier, during the impact. The data is extracted from top view videos for both surfaces. Extracting data continues until the outer rim seems stationary from the top view.

In addition to the aforementioned qualitative assessment for reducing the contact time, a quantitative comparison can be drawn. Although the droplet flattens to a quasi-elliptical shape at the end of the spreading stage on the ribbed sample, its projected area is equal to that on the smooth sample. For instance, the areas shown in Figure 4.5a and b at 3.3 ms are 29.9 and 29.8 mm², respectively. It should be noted that the actual area on the ribbed surface is larger by a factor of $\pi/2$ since the ratio of the ribbed length to the projected length is $\pi b/2b$, according to Figure 4.1a. The volume of the droplet can be considered as the product of the actual area and the average thickness of the liquid film, thus the relation between the film thicknesses on the surfaces can be described as

$$\frac{\delta_b}{\delta_s} \approx \frac{2}{\pi} \quad (4.6)$$

Where δ_b and δ_s denote the average thickness of the liquid film on ribbed and on smooth surfaces, respectively. Since the retraction velocity (Equation 4.5) is proportional to $\sqrt{1/\delta}$, the ratio of the average retraction velocity on the ribbed surface (V_{rb}) to that on the smooth (V_{rs}) is deduced as

$$\frac{V_{rb}}{V_{rs}} \approx \sqrt{\frac{\pi}{2}} \quad (4.7)$$

The retraction time (t_r) is the time needed for the outer rim to recoil from its position at the end of the spreading stage (R_{max}), so $t_r = R_{max}/V_r$. Since Figure 4.5c shows that the maximum value of r is between the maximum value of x and y , the average distance from the center can be assumed equal for both samples. Thus, the relation between the retraction time of the ribbed and smooth substrates can be concluded as

$$\frac{t_{rb}}{t_{rs}} \approx \sqrt{\frac{2}{\pi}} \quad (8)$$

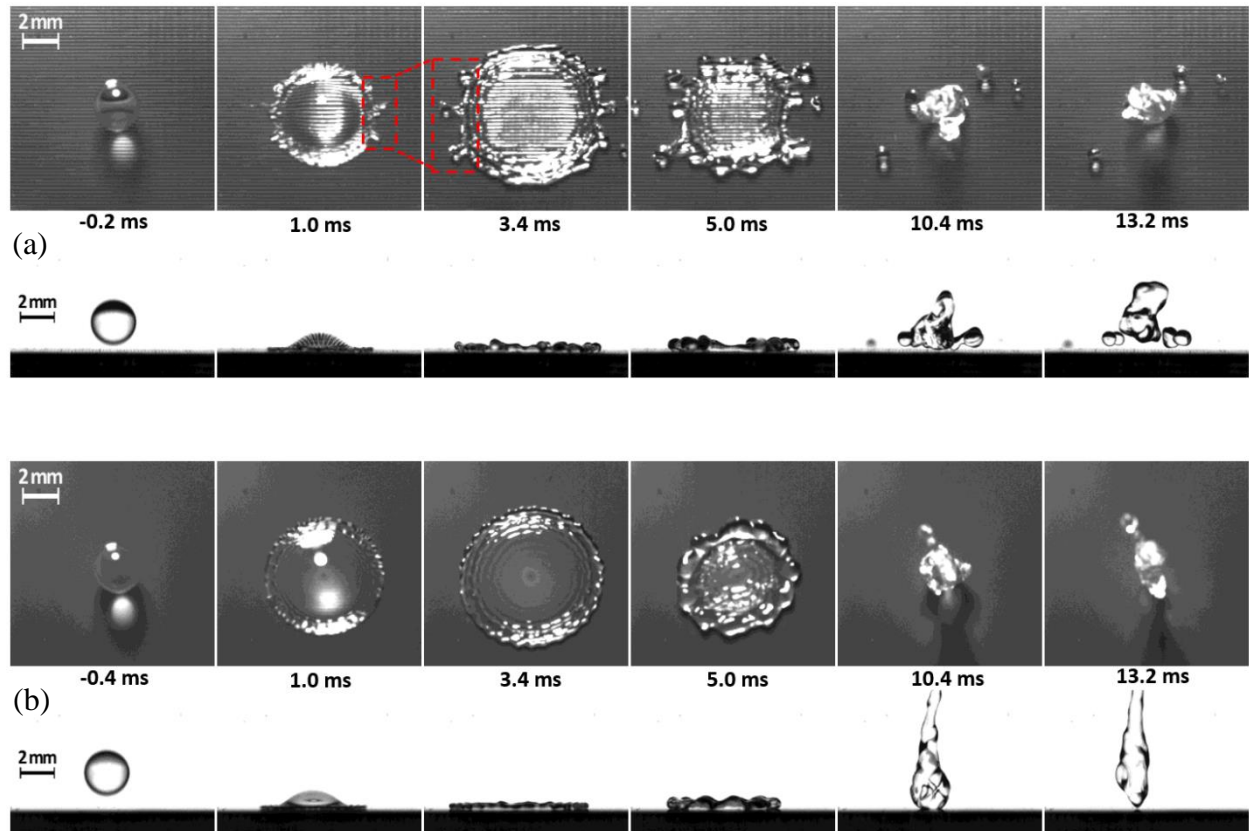
The measured retraction time for the impact mentioned above is $t_{rb} = 7.9 \pm 0.21$ ms for the ribbed surface while it is $t_{rs} = 10.2 \pm 0.15$ ms for the smooth PETG, which results in the ratio of 0.77 indeed comparable to $\sqrt{2/\pi} = 0.80$. This reduction is found to be persistent in a wide range of impact velocities between 1.0 and 1.6 m/s; intermediate impact regime. Such a step-like behavior has been reported for impact on a superhydrophobic surface decorated with a single macrotexture [40].

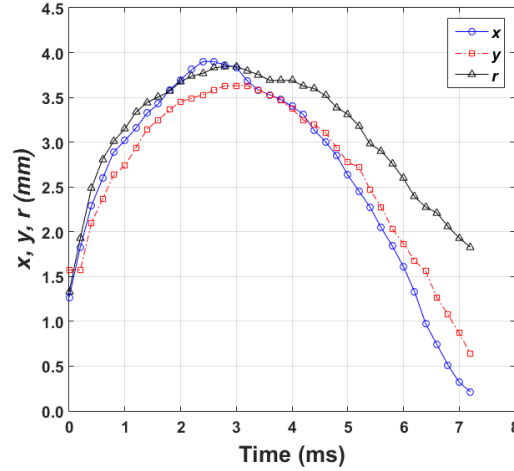
Considering both the low and intermediate impact regimes that have been defined so far, it can be deduced that in the former, the cylindrical ridges get partially wet as the impacting droplet does not see any difference between the ribbed and smooth substrates. The criterion for the droplet to wet the ribbed surface completely and distinguish the difference between the substrates is likely the sufficient amount of the dynamic pressure of the impacting droplet $\sim \rho V^2$ to dominate its Laplace pressure $\sim \gamma/R_0$. If one order of magnitude higher dynamic pressure satisfies this domination, the criterion for beginning the intermediate impact regime will be $We > 10$. Later in this paper, it can be seen that the range of We for this regime is $\sim 15-50$. The criterion for the transition from the intermediate to the high impact regime ($We \sim 55$) is defined as when the flattened droplet gets thin enough (critical thickness) to start splashing from its edges on the ribbed surface.

As the impact velocity increases from 1.0 to 1.6 m/s, the thinner middle region propagates wider in the y direction which results in a barrel-shape spreading at $V = 1.6$ m/s. It seems that at this point, the onset of the high impact regime, the thickness of the middle region reaches its critical value as the flattened droplet splashes in the x direction along the propagation line. The length of the

propagation line, which represents the portion of the liquid film with the critical thickness, increases from $\sim 2R_o$ at $V = 1.6$ m/s to $\sim 2R_{max}$ at $V = 2.0$ m/s where the flattened droplet splashes from its periphery on the ribbed surface. For the smooth PETG, however, the thickness of the pancake is still below its critical value as it does not splash from the outer edge. The increase in the extent of the middle thin region and the splashing lead to further reduction in the retraction time in this range of the impact velocity.

Figure 4.6a illustrates the spreading and retraction stages of the 9 μ L water droplet impacting on the ribbed surface at $V = 1.8$ m/s and $We \approx 58$. The barrel-shape spreading can be seen at 3.4 ms, when the flattened droplet splashes along the propagation line (shown with red rectangles). Moreover, the liquid film retracts in a square-like manner due to its non-uniform thickness.





(c)

Figure 4.6. Impacting of a 9 μL water droplet at $V = 1.8$ m/s on (a) ribbed sample of $2b = 0.2$ mm and (b) smooth PETG. On the ribbed substrate, the droplet spreads to a barrel-shape at 3.4 ms and retracts in a square-like manner. This faster anisotropic recoiling as well as splashing are the reasons for further contact time reduction. The contact time for the ribbed surface is 10.5 ± 0.45 ms, compared to 13.2 ± 0.40 for the smooth PETG. (c) Extracting the data from the top view videos, this graph depicts the variation of x , y and r during the impact. Since the splashing happens in x direction, the length of the outer edge before splashing is considered.

Since the droplet splashes at this impact velocity, drawing the aforementioned quantitative comparison may be debatable. Following the same rationality, however, it can be concluded that the retraction velocity should be even faster, as a larger portion of the flattened droplet has the critical thickness. This significantly faster retraction can be seen in Figure 4.6c, as the slopes of the plots for x and y are clearly sharper than the slope of r through the retraction stage. For example, at this impact velocity, the retraction time on the ribbed surface is found to be 6.9 ± 0.52 ms while it is 10.1 ± 0.30 for smooth PETG, concluding $t_{rb}/t_{rf} < \sqrt{2/\pi}$.

Finally at $V = 2.2$ m/s and $We \approx 86$, the thickness of the flattened water droplet on the smooth PETG reaches its critical value since it splashes from its periphery, as in Figure 4.7b. Moreover, the barrel-shape of the liquid film on the ribbed substrate changes to a new figure as shown in Figure 4.7c. This shape looks similar to the butterfly spreading reported for a superhydrophobic surface with a single macrotexture [39, 40]. The retraction time is found to be as short as 4.7 ± 0.29

on the ribbed surface, while it is 9.6 ± 0.89 for the smooth PETG. The variation of the spreading and retraction time of the 9 μL water droplet on the smooth PETG and the ribbed surface with $2b = 0.2$ mm is summarized in Figure 4.7a. Although the spreading dynamic of the droplet on the ribbed sample diverges from that on the smooth PETG for $V \geq 1.0$ m/s, it can be seen that the spreading time is the same for both of them through the whole range of the velocity investigated in this study. This similarity has been reported for the same droplet size impacting on a superhydrophobic surface with one single macrotexture [39].

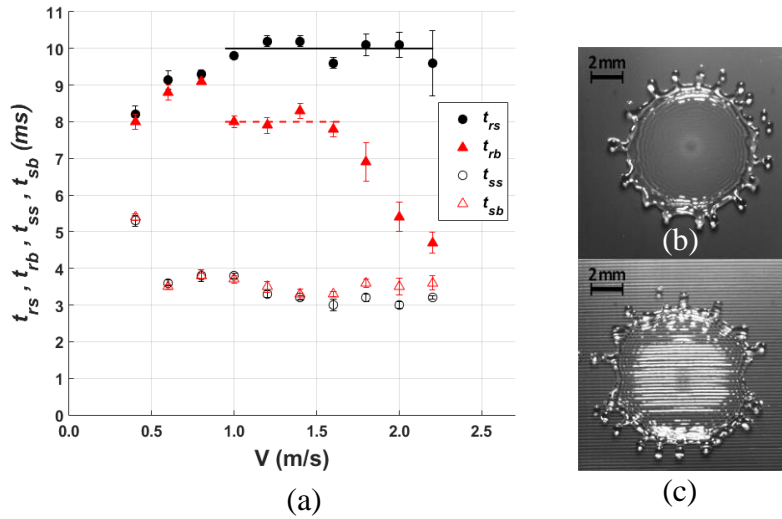


Figure 4.7. (a) The plot depicts the variation of the retraction and spreading time of a 9 μL water droplet impacting on smooth PETG and ribbed sample of $2b = 0.2$ mm for impact velocity changing from 0.4 to 2.2 m/s. Filled and empty circles show the retraction (t_{rs}) and spreading (t_{ss}) time on the smooth PETG, respectively, while the filled and empty triangles indicate the retraction (t_{rb}) and spreading (t_{sb}) time on the ribbed sample. The black solid line is the average of t_{rs} (10.0 ms) for $V = 1.0$ –2.2 m/s. The red dashed line is the average of t_{rb} (8.0 ms) for $V = 1.0$ –1.6 m/s, the range in which $t_{rb}/t_{rs} \approx \sqrt{2/\pi}$. (b) The pancake with the critical thickness on smooth PETG at $V = 2.2$ m/s, where it splashes from the outer rim. (c) The droplet adapts a butterfly shape at $V = 2.2$ m/s on the ribbed substrate.

We also studied the effect of the ridge size on decreasing the contact time for the whole range of the impact velocity. To do this, we repeated all our experiments, explained above, on ribbed surfaces with $2b = 0.1$ and 0.3 mm (see Figure 4.1a for the geometry). The results (Figure 4.8a) indicate that the droplet behaves similarly on the ribbed surfaces of $2b = 0.1$, 0.2 and 0.3 mm.

Since Equation (4.8) is independent of the ridge's size, collapsing the data is reasonable. As a matter of fact, the extent to which contact time decreases on a superhydrophobic surface decorated with one single macrotexture is also found to be constant for the texture's amplitude changing from 100 to 500 μm [40]. Figure 4.8a shows that the average contact time of the 9 μL water droplet at $V = 1.0 - 1.6$ m/s decreases from 13.2 ms for smooth PETG to 11.5 ms for the ribbed surfaces. The contact time for the ribbed surfaces reduces further as the impact velocity increases, while it remains unchanged for the smooth PETG. We also investigated the impact of 6, 16 and 31 μL droplets, whose $R_o = 1.1$, 1.6 and 2.0 mm respectively, on both ribbed and smooth PETG. The contact time presented in Figure 4.8b is normalized by the average contact time of the droplets on the smooth PETG. It is observed that the contact time decreases 13% in the intermediate impact regime $We \sim 15-50$.

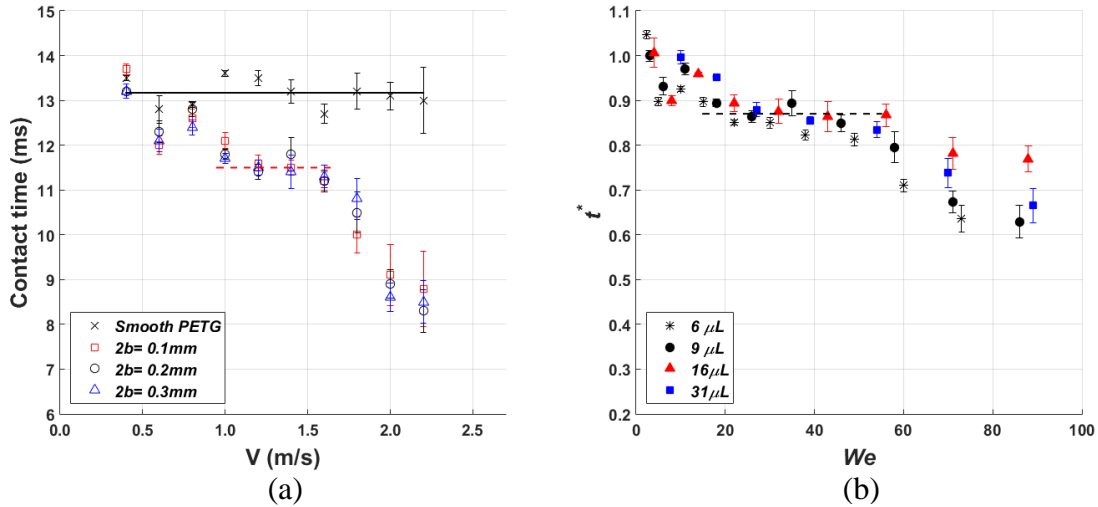


Figure 4.8. (a) Variation of the contact time of a 9 μL water droplet for impact velocity $V = 0.4-2.2$ m/s on smooth PETG as well as ribbed samples of $2b = 0.1, 0.2$ and 0.3 mm. The solid black line indicates that the average contact time of the droplet on smooth PETG is independent of V as reported in literature [31, 40]. The red dashed line shows the average contact time of 11.5 ms on the ribbed samples for $V = 1.0-1.6$ m/s, intermediate impact regime, which is 13% shorter than that on the smooth PETG. The reduction in contact time is attributed to the 20% shorter retraction time on the ribbed samples. (b) For the ribbed sample of $2b = 0.2$ mm, the plot shows the contact time of water droplets of four volumes normalized by their contact time on smooth PETG. The black dashed line illustrates a 13% reduction for $We \sim 15-50$, the intermediate impact regime, before the droplets start to splash on the ribbed surface.

Figure 4.8b also indicates that the onset of further reduction in contact time is $We \sim 55$, the value at which splashing happens in x direction along the propagation line. Regarding Equation (4.4), the thickness of the flattened droplet is governed by We . The critical We at which the droplet starts splashing from its periphery on smooth PETG is ~ 90 . Interestingly, the ratio of the critical We on the ribbed surface to that on the smooth PETG is $\sim 55/90 = 0.61$, a value comparable to $2/\pi = 0.64$. This may be interpreted as the term of the surface energy in the critical We being increased by a factor of $\pi/2$ for the ribbed substrate.

In general, the fabricated ribbed superhydrophobic surfaces in this study showed shorter contact time compared to their smooth counterpart regardless of the point of the impact on the surface. In contrast, reducing the contact time by incorporating a single macrotexture or multiple intersecting ridges requires impact happening exactly on the texture or the intersection [39, 40, 87]. To complete our study, we compared the droplet impact on one of the ribbed surfaces ($2b = 0.2$ mm) and on a single macrotexture. Nickel (Ni) wire of 0.1 mm in diameter was used as the texture [40] and was secured on a smooth sample using pieces of duct tape. Both Ni wire and the surface became superhydrophobic following the same procedure explained earlier. In addition, ribbed surfaces ($2b = 0.2$ mm) with Ni wire added along and perpendicular to the ridges were tested afterwards. Figure 4.9a shows the normalized contact time of the surfaces by the inertial-capillary time scale for 9 μ L droplet at $V = 0.4$ -2.2 m/s. In the intermediate impact regime, the ribbed surface shows the contact time of $t_c \approx 2.05\tau_o$, even shorter than the Rayleigh limit for any collision regardless of the point of impact. For the sake of comparison, it is worth noting that the contact time for smooth PETG was $t_c \approx 2.35\tau_o$. In the case of impact on the wire exactly in the center, ribbed surface with wire along the ridges exhibits shorter contact time for low impact velocity, while the ribbed surface with wire perpendicular to the ridges shows the shortest contact for higher

V. While the significantly shorter contact time caused by incorporating the wire is strictly related to the point of impact, the associated results for the ribbed surface are independent of it.

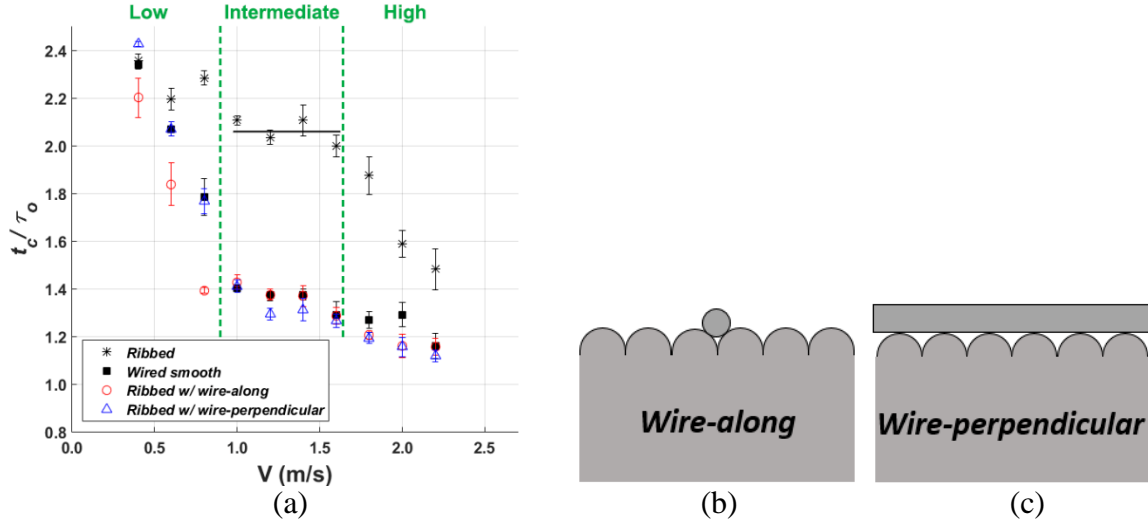


Figure 4.9. (a) Contact time of 9 μL water droplet normalized by $\tau_o = \sqrt{\rho R_d^3/\gamma}$ is plotted for superhydrophobic ribbed ($2b = 0.2$ mm) with no wire, wired smooth (Ni wire diameter, $d = 0.1$ mm), ribbed with wire along and perpendicular to the ridges at varied impact regimes. The schematic cross section of ribbed with wire along (b) and perpendicular (c) to the ridges are shown.

4.4 Conclusions

This chapter provided a comprehensive investigation of water droplet impacting on superhydrophobic surfaces *fully decorated with cylindrical ridges* (ribbed) at different impact velocities. The dynamic of impact on these surfaces is classified into three regimes regarding the impact velocity; low, intermediate and high. The data declare that the impact on such a surface pattern is quite similar to that on a macroscopically smooth one in the low impact regime, whereas it changes for the intermediate and high velocity regimes. The asymmetric spreading of the droplet in the intermediate regime shows that its kinetic energy is sufficient to wet the surface completely and create a thinner flattened droplet on the ribbed surface. Therefore, the retraction time decreases

by a factor of $\sim\sqrt{2/\pi}$, consequently leading to $\sim 13\%$ reduction in the contact time in this regime. Such a step like behavior was reported for the impact on a surface decorated with a single cylindrical ridge [40]. In the high impact regime, the retraction and the contact time reduce further since the thin liquid film reaches the critical value and splashes from its periphery. It is also shown that the size of the ridges has a negligible effect on the contact time, same as the behavior reported for one single ridge [40].

It should be noted that the current study has successfully addressed the problem with using only one single macrotexture, to obtain the shortest contact time, by making it independent of the contact point when ribbed surfaces are used. For a single macrotexture, it is known that the droplet must hit the texture exactly in the center to get the best results, which is not the case most of the times. The simplified and cost-effective method of fabricating the ribbed superhydrophobic surfaces presented in this chapter introduced us to a surface with contact time shorter than the Rayleigh limit, $t_c \approx 2.05\tau_o$, regardless of the point of the impact. Adding a Ni wire as a macrotexture to the ribbed surface reduces the contact time even further, still if the impact occurs on the wire. For the low impact regime, the ribbed surface with wire along the ridge shows the shortest contact time, whereas for the intermediate and high impact regimes the ribbed surface with wire perpendicular to the ridges indicates the shortest contact.

Chapter 5 Droplet Impact on Cylindrical Surfaces to Achieve the Shortest Possible Contact Time

5.1 Introduction

This chapter is also adopted from my paper [46] published very recently in *JCIS*. Droplet impact on a solid substrate has been the focus of numerous studies [23, 31, 33, 39-41, 45, 69, 87-90] due to its application in processes such as spray coating [91], inkjet printing [92], self-cleaning [12], and anti-icing [93]. Perhaps, one of the first pioneering studies on this subject has been done by Worthington [88] who investigated the patterns left by drops of various liquids impinging smoked glass plates. Thanks to recent advances in high-speed photography, researchers have been able to investigate the challenging physics of the impact more precisely by experiments. It has been shown that when the solid substrate is non-wettable (superhydrophobic) and flat, the impact consists of radial spreading of the droplet followed by its retraction and bounce off. The summation of spreading and retraction times, which is called contact time (t_c), is a key factor of the impact dynamics that researchers have endeavored to minimize, intending to enhance the water repellency of superhydrophobic surfaces.

Richard *et al.* have shown that the contact time for a droplet of density (ρ), surface tension (γ), and radius (R_o) scales with inertial-capillary time scale, $\tau_o = \sqrt{\rho R_o^3 / \gamma}$, and is independent of the impact velocity (V) [31]. In addition, it has been accepted that symmetric bouncing is associated with the shortest contact time [23, 31, 33, 39], although this correlation is limited by Rayleigh constant, $t_c / \tau_o \geq \pi / \sqrt{2} \approx 2.2$ [34]. In contrast, Bird *et al.* have recently shown that utilizing a single macrotexture (ridge) leads to an even shorter contact time below this theoretical limit [39]. They theorized that this reduction is the consequence of altering mass distribution in the spreading stage. Following them, Gauthier *et al.* claimed that the contact time on a single ridge takes discrete

values of $\sim\tau/\sqrt{2}$ and $\sim\tau/\sqrt{4}$ at intermediate and high impact velocity ranges, respectively, where τ is the contact time on an equivalent surface with no ridge [40]. Their discussion implies that if the impact happens on an intersection that splits the droplet into n fragments, the contact time would be $t_c \sim \tau/\sqrt{n}$. On the other hand, Paterson *et al.* showed that the contact time of a bouncing Lindenfrost drop on such an intersection barely changes as n increases [87]. The common issue in all the aforementioned studies associated with contact time reduction is that the impact must happen exactly on the ridge or intersection. As explained in Chapter 4, we resolved this issue by fabricating a surface fully structured by cylindrical ridges (ribbed surface) [45]. Although the contact time reduction ($\sim 13\text{-}35\%$) caused by utilizing the ribbed surface was not as high as that of a single macrotexture, the implemented surface pattern led to a contact time shorter than the Rayleigh limit, $t_c < 2.05\tau_o$, regardless of the location of the impact.

Inspired by the work of Bird *et al.* [39], Liu *et al.* studied the impact dynamics on curved superhydrophobic surfaces using both experiments and numerical modeling [41]. They started with investigating the impact on Echevaria leaves, which induce asymmetric bouncing due to their cylindrical geometry. Their experimental and numerical results qualitatively agreed that the asymmetry is the consequence of more momentum being transformed in the azimuthal (curved) direction. Specifically, they investigated the contact time where the radius of the surface (R) is comparable to that of the droplet (R_o). Subsequently, they demonstrated that the contact time decreases for cylindrical surfaces as R/R_o decreases, yet remains unchanged for spherical ones. Although their study involved different impact velocities (0.6-1.1 m/s), they did not consider how the impact velocity affects the contact time, *which is the objective of the current chapter*. Later in this chapter, we will compare our observations with Liu *et al.*'s [41] to validate our results and discussion.

Here, we study the impact of water droplets on curved surfaces for various impact velocities and ratios of the radii (R/R_o). Our results show the extent to which the contact time changes with respect to the impact velocity (for different R/R_o), for which we present a correlation with 95% confidence intervals. Since decorating a flat substrate with the ribbed pattern and/or a single ridge had reduced the contact time [39, 40, 45, 87], we examined the contact time for ribbed-curved surfaces and those with a ridge on their peaks. It should be noted that the focus of this study is the impact that occurs on the acme of curved surfaces, hence adding a ridge (elongated in the axial direction) on these peaks does not impose any new limitations regarding the location of impact in the axial direction. However, the restriction in azimuthal direction does still hold.

5.2 Experimental Methods

5.2.1 Sample Preparation

The substrates, used in this study, were borosilicate glass tubes of 9.0 and 12.7 mm in diameter (McMaster Carr, USA) and semi-cylinders printed in the same diameters using an extruder-type 3D printer (Ultimaker 2, Netherlands). Such a printer with a nozzle of 0.4 mm in diameter provided us curved samples enveloped in cylindrical ridges (ribbed-curved) elongated in azimuthal direction. The ridges' diameters were 300 μm , controlled by Cura software with a resolution of about 5 microns. To obtain the curved samples with an additional macrotexture, a copper wire with a diameter of 0.2 mm (McMaster Carr, USA) was secured on their peaks using pieces of duct tape. To comprehend the dynamics of impact on the curved surfaces, we had to compare it with droplet impact on a macroscopically-smooth flat surface. Such a substrate was obtained by polishing a 3D-printed specimen (15×15×10 mm) with 600 and 1200 grit sand papers (Allied High Tech Products Inc., USA). All the solid substrates were washed with a typical lab detergent and then

sonicated in water for 30 min before the soot deposition. The superhydrophobic coating utilized in this work is a layer of functionalized chimney-modified soot, which has been explained in detail in the previous chapters. The functionalized soot coating demonstrated advancing and receding contact angles of $165.8 \pm 2.6^\circ$ and $164.4 \pm 1.5^\circ$ for water, respectively. A Drop Shape Analyzer (DSA25E, Krüss, Germany) was used for these measurements.

5.2.2 Experimental Setup

Using a precisely-controlled automated syringe and calibrated needles, we dosed water droplets ($\rho = 1000 \text{ kg/m}^3$ and $\gamma = 73 \pm 0.2 \text{ mN/m}$) of volume 6, 9, and 16 μL (with $< 5\%$ error), whose radii were 1.13, 1.29, and 1.56 mm respectively. Releasing the droplets from 8 to 247 mm above the substrates, we were able to acquire impact velocities from 0.4 to 2.2 m/s. The impacts were recorded by a high-speed camera (Phantom Miro ex2, Ametek, USA) at 10000 frames per second (fps) from front and side views for curved samples and from side and top views for the flat one. An open-source piece of software called Tracker was used to analyze the videos. The impact for a specific release height was repeated at least three times on each sample and the impact velocity was confirmed by measuring it via Tracker in the last five frames before the impact. The contact time was defined as the time from which the droplet touched the sample until its last point of contact became detached. In the case of the wired substrates, for which the droplet split, the contact time of each fragment was considered and then averaged. Figure 5.1 shows the schematic diagram of the experiment (front view) as well as the side view of a ribbed-curved specimen and a wired-curved sample before coating.

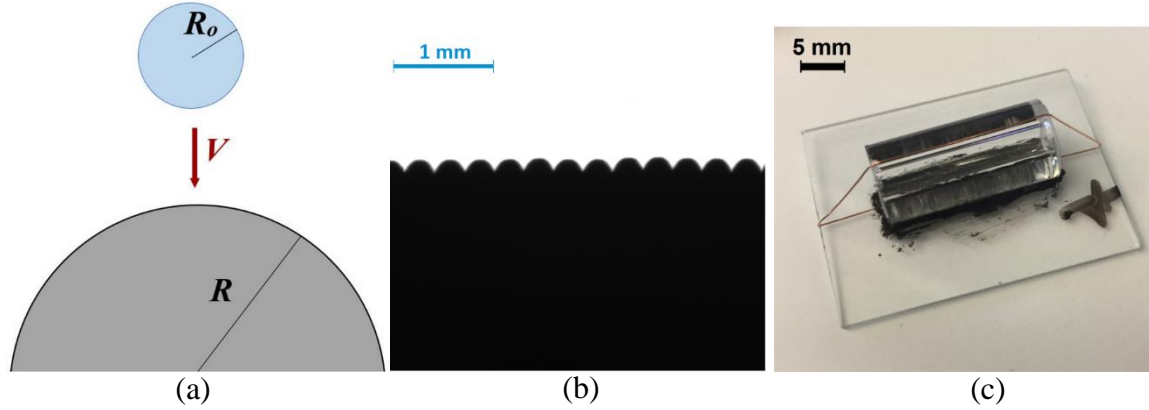


Figure 5.1. (a) Experimental configuration. (b) Side view of a ribbed-curved sample with radius of 4.5 mm and ridges of 300 μm in diameter. (c) Image of a curved specimen ($R = 4.5$ mm) with an additional macroscopic copper wire (with a diameter of 0.2 mm) on its peak prior to coating.

5.3 Results and Discussion

Although droplet impact studies date back to 19th century [88], the complicated dynamics of this subject still present some dilemmas. For example, the maximum spreading of the impacting droplet has been believed to scale with Reynolds number ($Re = \rho V R_o / \mu$, with μ being viscosity) as $r_{max} \sim R_o Re^{1/5}$ [85, 86]. This discussion implies that the surface tension of the droplet has no effect on r_{max} . In 1996, however, Pasandidehfard *et al.* claimed that Weber number ($We = \rho V^2 R_o / \gamma$) is crucial for maximum spreading and capillary effects can be neglected only if $We \gg \sqrt{Re}$ [94]. Later in 2004, Clanet *et al.* defined a criterion for the impact to assess whether it is dominated mainly by μ or γ [36]. They claimed that, if Impact number ($P \equiv We / Re^{4/5}$) is higher than unity, the impact should be considered viscous and $r_{max} \sim R_o Re^{1/5}$. Otherwise, it should be considered to be inviscid and its maximum spreading radius is governed as $r_{max} \sim R_o We^{1/4}$. This discussion for a flat surface has been confirmed by most of the relevant studies [23, 41, 45, 87] mentioned in the Introduction of this Chapter. The Impact number for our experiments here is $P < 0.13$ (for highest V and R_o), meaning that the impacts are inviscid.

Investigating the impact of a 9 μL ($R_o = 1.29 \text{ mm}$) droplet on the flat and curved ($R = 4.5 \text{ mm}$) samples for various impact velocities (V), we found that the spreading and retraction phases are noticeably different (see Figure 5.2a-b). On the flat surface, the droplet spreads to a circle and then recoils symmetrically until its center engulfed by the retracting rim. On the curved substrate, however, it spreads longer in the azimuthal direction, which causes an asymmetric bouncing [41]. Monitoring the spreading radius (r) on flat as well as spreading length in axial (x) and azimuthal (z) directions yields Figure 5.2c. It can be seen that r recoils at a constant velocity scaling as $V_r \sim \sqrt{\gamma/\rho\delta}$, where δ is the average thickness of the flattened droplet at the beginning of the retraction stage, confirming the findings presented in the literature [23, 39, 42]. This means that the time needed for the expanded droplet to retract scales as $t_r \sim r_{max}/\sqrt{\gamma/\rho\delta}$. Consolidating this correlation with conservation of volume ($\delta \sim R_o^3/r_{max}^2$) yields that the retraction time scales with $\tau_o = \sqrt{\rho R_o^3/\gamma}$. Moreover, as mentioned earlier, it has been illustrated that contact time (summation of spreading and retraction time) for a flat superhydrophobic surface is independent of V and scales with τ_o . Interestingly, in the studies associated with reducing the contact time [39-41, 45, 87], only the retraction time has been reduced. In fact, for our curved substrate, analogous to what Liu *et al.* reported [41], spreading time (3.5 ms in Figure 5.2) in the axial direction is the same as that on the flat surface because it is controlled primarily by inertia. Moreover, the droplet leaves the surface as soon as the retraction in the axial direction completes. This means, firstly, the faster the retraction in the x direction, the shorter the contact time. Secondly, the way in which contact time changes with respect to V is the same as how the retraction time does. In order to quantify this relationship, the distance from which the droplet starts to retract and the retraction velocity need to be found for various values of V .

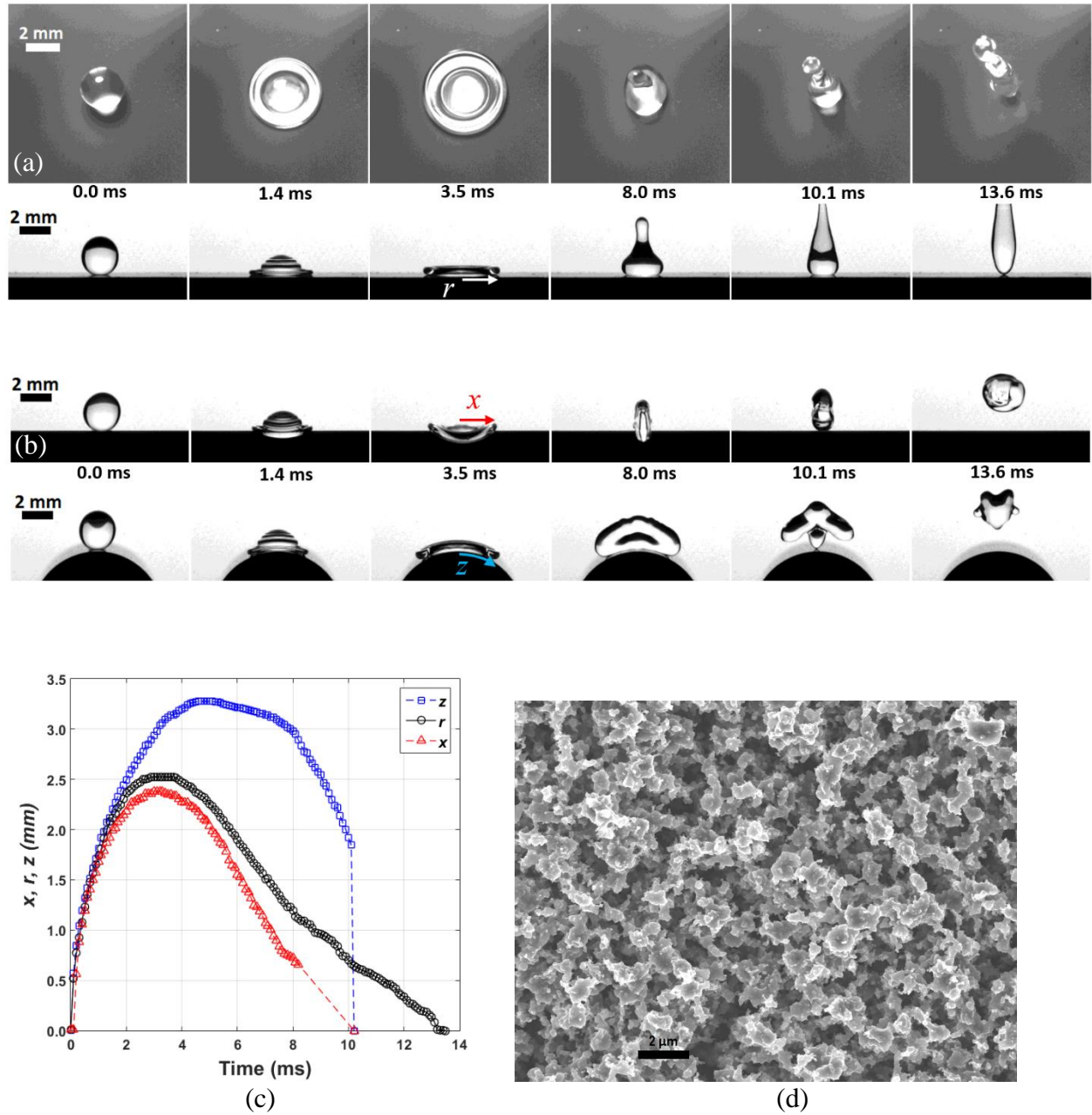


Figure 5.2. Impact of a 9 μL water droplet at $V = 1.0$ m/s on (a) flat and (b) curved ($R = 4.5$ mm) substrates. Spreading time in the axial direction (x) is equal to that found on a flat surface. Contact times were found to be 13.57 ± 0.06 ms (obtained from side-view videos) for the flat surface and 10.10 ± 0.23 ms (obtained from front-view videos) for the curved one. (c) Temporal variation of x , r , and z , as defined in this chapter, during the impact. Extracting data points for x continued until the outer rim was visible from the side view. Comparing the data of this diagram with the similar content reported by Liu *et al.* [41], the accuracy and validity of our measurements are confirmed. (d) Scanning electron microscopy (SEM) image of the functionalized soot utilized as superhydrophobic coating.

Besides showing a higher z_{max} , Figure 5.2c illustrates two more concepts. First, the maximum spreading radius (r_{max}) is slightly bigger than x_{max} . Second, the x diagram reduces at a significantly sharper slope than the r diagram does. To quantify the effect of V on these observations, we define dimensionless radius and lengths as $r^* = r_{max}/R_o$, $x^* = x_{max}/R_o$, and $z^* = z_{max}/R_o$. Figure 5.3 shows their deviation for different Weber numbers. It can be seen that power lines fit the measured data quite well with numerical coefficients of 1.02, 1.00, and 0.97 for r^* , x^* , and z^* , respectively. These values were obtained from a least-squares fit and are, indeed, close to 1.07 reported by Clanet *et al.* [36] and 1.1 by Patterson *et al.* [87]. Despite the close powers found for Weber number for the correlations associated with r^* and x^* (0.25 and 0.24, respectively), the power found for z^* is noticeably higher (0.35). This can be explained with what is shown in Figure 5.2c. While the droplet spreads in r and x equally until 3.5 ms, it continues to spread in z until 5.3 ms. Liu *et al.* mentioned the same behavior in their study [41] and justified it qualitatively with their numerical calculations, which depicted more momentum being transferred in the azimuthal direction than the axial one.

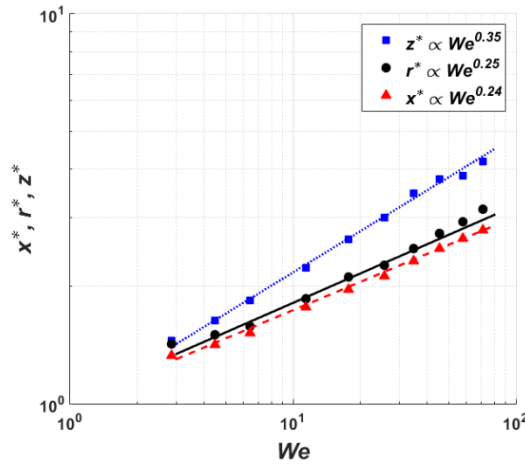


Figure 5.3. The maximum spreading radius and lengths normalized by $R_o = 1.29$ mm (9 μ L) for different Weber numbers (various V). The dashed, solid, and dotted lines respectively depict $x^* = 1.00We^{0.24}$, $r^* = 1.02We^{0.25}$, and $z^* = 0.97We^{0.35}$. The error bars were too small to be shown (< 0.04).

The faster retraction velocity in the axial direction, recognized from the sharper slope of x in Figure 5.2c, can be observed in Figure 5.2ab as well. While x considerably recoils between 3.5 and 8.0 ms, r does moderately and z barely changes. Since the impact happens over a shorter period of time on the curved surface compared to the flat one due to this faster retraction in the x direction, we measured the retraction velocity (V_r) in the x and r directions from similar diagrams plotted at various impact velocities. We define a characteristic velocity as $v = \sqrt{\gamma/\rho R_o}$ to normalize V_r with. Since V_r , r^* and x^* all depend on the impact velocity, plotting the variation of dimensionless retraction velocities $V_r^* = \frac{V_r}{v}$ with respect to r^* and x^* helps us comprehend the contact time reduction better (Figure 5.4).

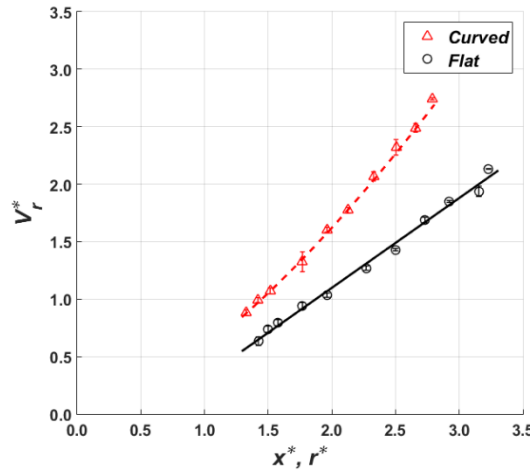


Figure 5.4. The plot displays how the normalized retraction velocities ($V_r^* = V_r/v$) for curved and flat surfaces correlate with x^* and r^* , respectively. The solid black line illustrates that $V_r^* \propto r^*$, whereas the dashed red line follows $V_r^* \propto x^{*\frac{3}{2}}$.

Figure 5.4 indicates that V_r^* changes linearly with r^* for the flat surface, and is proportional to $(x^*)^{\frac{3}{2}}$ for the curved substrate. Assuming that the contact time changes with V in proportion to the change in retraction time, as explained earlier, this linear correlation for flat substrate concurs with the fact that the contact time is independent of the impact velocity [31]. Following the same

rational, a relationship can be developed between the contact time and the Weber number on curved surfaces. Equation (5.1) summarizes what was shown in Figure 5.3 and Figure 5.4 for such a geometry.

$$(a) x_{max} = 1.00R_oWe^{0.24} \quad (b) \frac{V_r}{v} \propto \left(\frac{x_{max}}{R_o}\right)^{1.5} \quad (5.1)$$

A scaling correlation will be deduced from Equation (5.1) as

$$\frac{t_c}{\tau_o} \sim We^{-0.12} \quad (5.2)$$

Since R/R_o is a critical factor that must be considered for contact time on curved surfaces [41], we have checked this scaling model for five different ratios obtained from 6, 9, and 16 μL droplets impacting the samples with diameters of 9.0 and 12.7 mm. Figure 5.5a demonstrates that this scaling model fits well with the numerical coefficient $C = 2.612 \pm 0.255$, presented in Equation (5.3), with a 95% confidence.

$$t_c = C\tau_oWe^{-0.12} \quad (5.3)$$

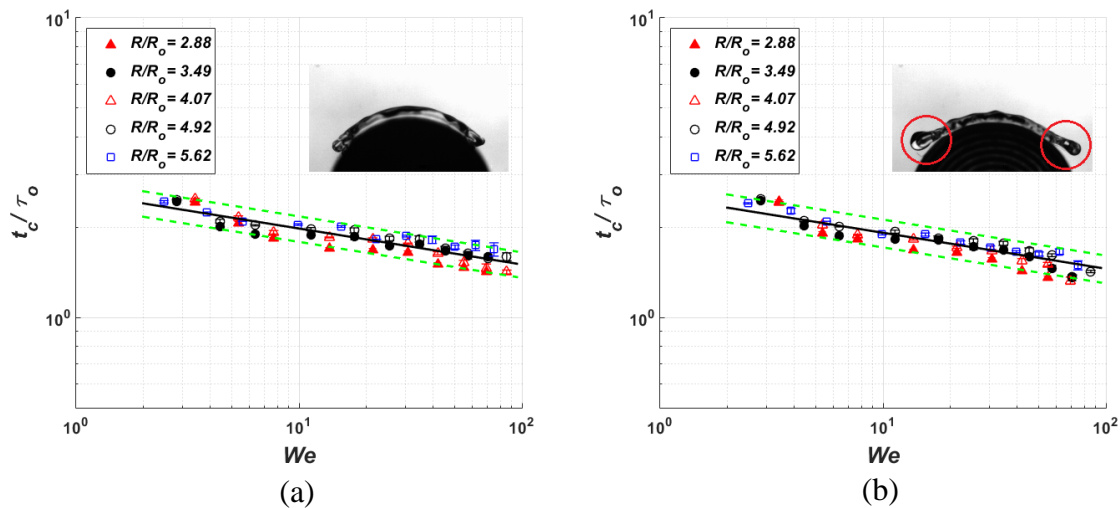


Figure 5.5. (a) The plot shows the trend of the reduction of contact time on curved surfaces as the Weber number increases. The contact time has been normalized by the inertial-capillary time scale $\tau_o = \sqrt{\rho R_o^3 / \gamma}$. The solid black line represents $\frac{t_c}{\tau_o} = 2.612We^{-0.12}$. The dashed green lines show the top and bottom boundaries of the numerical coefficient in Equation (5.3) for data acquired from the droplet impacts with different R/R_o ratios with a 95% confidence. (b) This plot shows that the normalized contact time versus Weber number for ribbed-curved samples follows the same trend yet with a slightly smaller numerical coefficient: $C = 2.528 \pm 0.269$ (the solid black and dashed green lines). The insets show that the edges of liquid film spreading on a ribbed-curved sample do not contact the solid substrate for high impact velocities, whilst they keep connected on the curved surface. The insets are associated with the impact of a 9 μ L droplet on a curved/ribbed-curved surface of $R = 4.5$ mm at $V = 1.6$ m/s ($R/R_o = 3.49$).

We have shown in Chapter 4 that contact time of an impacting droplet on a ribbed-flat surface becomes shorter for relatively high impact velocity due to a thinner flattened droplet and longer spreading along the ridges. Thus, a ribbed-curved surface with ridges elongated in the azimuthal direction (see Figure 5.1b) may cause more spreading in this direction and boost the asymmetry of the bouncing, consequently leading to a shorter contact time. Figure 5.5b shows that the normalized contact time of ribbed-curved substrates decreases as the Weber number increases following the predicted scaling model, given by Equation (5.3), with a slightly smaller numerical coefficient of 2.528 ± 0.269 with a 95% confidence. The reason that the reduction is almost negligible for this case, unlike for the flat surface [45], may be attributed to the detachment of the edges of the liquid film in the spreading stage for relatively higher impact velocity, where a shorter contact is expected (see the insets in Figure 5.5a-b). Moreover, as we expected, changing the diameter of the ridges (100-300 μ m) has negligible effect on the contact time, similar to Figure 4.8, because the size of the ridges (hundreds of microns) is one order of magnitude smaller than the size of the drops (millimeters). The data associated with these tests are presented in Figure 5.6.

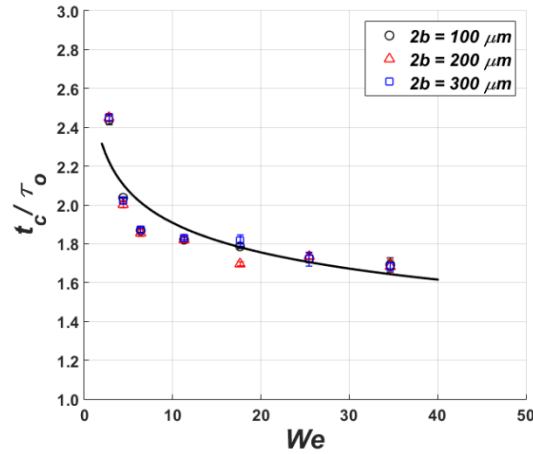


Figure 5.6. For the case of $R/R_o = 3.49$, the plot depicts the variation of the normalized contact time vs changing the Weber number for ribbed-curved samples with various ridge's diameters ($2b = 100\text{--}300\text{ }\mu\text{m}$). The plot illustrates that changing the size of the ridges barely changes the contact time. The solid black line represents $\frac{t_c}{\tau_o} = 2.528We^{-0.12}$.

The other technique which can be used to manipulate the dynamics of impact, in order to achieve a shorter contact time, is to utilize a single macrotexture. As such, contact times for 9 μL droplets on both ribbed and smooth curved samples ($R = 4.5\text{ mm}$) with an additional macrotexture (copper wire of 0.2 mm in diameter) on their peaks were investigated for various impact velocities. The results of this investigation, along with the results for curved and ribbed-curved substrates, are shown in Figure 5.7. It can be seen that contact time of the droplets on the ribbed-curved substrate (containing no wire) is slightly smaller than that of the smooth curved one; however, incorporating the wire to them makes the contact time significantly smaller due to the faster retraction on the wire [39]. Moreover, the contact times for all four samples follow a similar reduction trend up to $V = 1.4\text{ m/s}$. On the other hand, for $V = 1.6\text{--}2.0\text{ m/s}$ the contact time on the wired ribbed-curved surface shows an unprecedented contact time of $t_c = 0.84 \pm 0.02\tau_o$, whilst the shortest contact times reported so far have been $t_c \approx 1.4\tau_o$ for a single macrotexture [39] and $t_c \approx 1.2\tau_o$ for an intersection of six spokes [87]. A similar step-like shortening the contact time for varied impact velocities has also been observed for a wired flat surface [40] and a wired ribbed surface (for

relatively high impact velocities) [45], which means that the wire appears to be the dominant feature that has changed the dynamics of impact in this case. This dominance may be attributed to the fact that the thickness of the liquid film, on which the retraction velocity depends, becomes comparable to the ridge size.

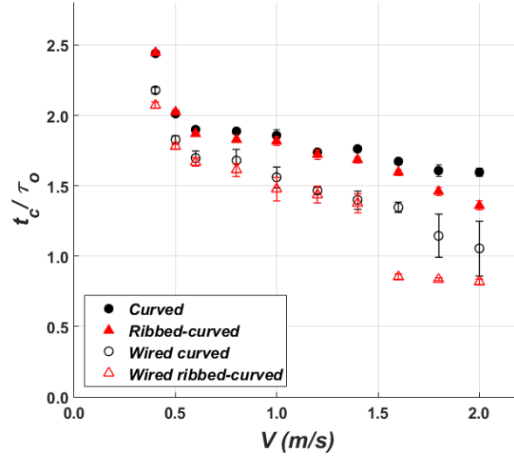


Figure 5.7. This plot demonstrates that the contact time of a bouncing 9 μ L droplet on curved, ribbed-curved, wired curved, and wired ribbed-curved substrates decreases as the impact velocity increases. The wired ribbed-curved substrate exhibits a contact time of $t_c = 0.84 \pm 0.02\tau_o$ for $V = 1.6$ - 2.0 m/s, which may be the shortest contact physically possible.

Figure 5.8 shows how the effect of wire, curvature, and ribbed pattern yields such a short contact time, which may be the shortest contact physically possible. Comparing the spreading time in the x direction (t_{sx}), along with x_{max} and V_r of the impact (wired ribbed-curved), with those of smooth curved surfaces at $V = 1.8$ m/s clarifies the reduction. The values of spreading time, t_{sx} , for curved and wired ribbed-curved surfaces are 3.23 ± 0.06 and 2.21 ± 0.11 ms, respectively. This means that the dynamic of impact has changed in such a way that spreading time in the axial direction becomes 31% shorter for the wired ribbed-curved surface, while it has barely changed for the other cases as mentioned earlier. In contrast, x_{max} is found to be 3.46 ± 0.02 and 3.42 ± 0.16 mm for curved and wired ribbed-curved surfaces, respectively. This similarity may be the consequence of the

continuation of the common reduction trend shown by these two samples for lower V as presented in Figure 5.7. The retraction velocity (V_r) for the case of wired ribbed-curved is 150.3 ± 3.4 cm/s, which is significantly higher than that of the curved surface ($V_r = 59.1 \pm 0.9$ cm/s). These three parameters, as well as the detachment of the edges caused by the ribbed pattern, yield a contact time of 4.55 ± 0.10 ms for the impact whose inertial-capillary time scale is $\tau_o = 5.44$ ms.

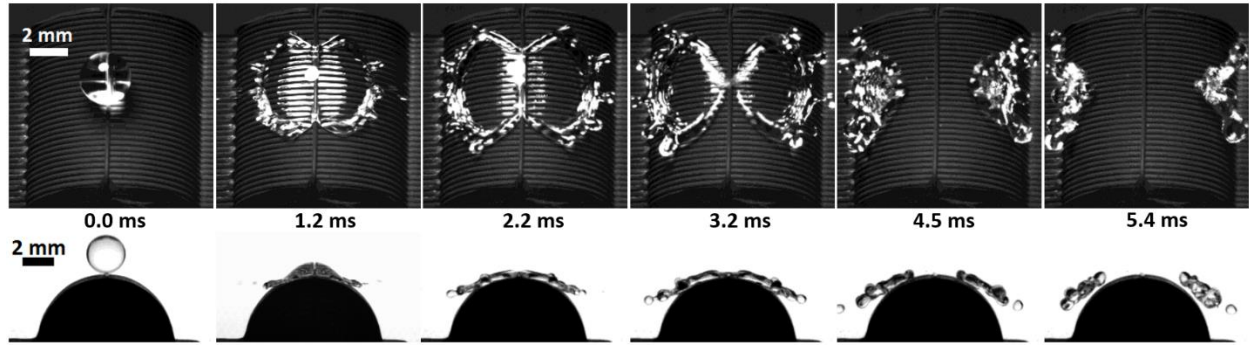


Figure 5.8. Impact of the 9 μ L water droplet at $V = 1.8$ m/s on the wired ribbed-curved ($R = 4.5$ mm) substrates. While the inertial-capillary time scale of the impact is $\tau_o = 5.44$ ms, the last point of the droplet leaves the surfaces at 4.5 ms (may not be clear here). This means that $t_c \approx 0.84\tau_o$, which is an unprecedented contact time.

5.4 Conclusions

A systematic investigation of droplet impact on non-wettable flat and curved solid substrates done in this study resulted in the development of relationships for contact time reduction for a curved surface. For a flat surface, it was shown that since the normalized retraction velocity (V_r^*) of the flattened droplet is linearly proportional to the normalized maximum spreading radius (r^*), the contact time is independent of impact velocity [31, 33, 40]. For the curved substrate, however, as the retraction velocity in the axial direction is proportional to $x^{*\frac{3}{2}}$, the contact time changes with Weber number as $\frac{t_c}{\tau_o} \sim We^{-0.12}$. A numerical coefficient of 2.612 ± 0.255 (with a 95% confidence) was found for this scaling model for droplets of three different volumes (6, 9, and 16 μ L) impacting

on surfaces with diameters of 9.0 and 12.7 mm, which provides various R/R_o ratios (2.88-5.62). Such a scaling model was also confirmed for ribbed-curved surfaces with a slightly smaller numerical coefficient for the same R/R_o ratios. These factors confirm that our presented argument, which says the contact time changes with respect to V as the retraction time does, is consistent with the experimental results. Moreover, adding a wire as an additional macrotexture to the peaks of curved and ribbed-curved samples reduced the contact time further due to the faster retraction on the wire [39]. Finally, the contact time for the wired ribbed-curved surface, which contains both micro- and macro-scale roughness, decreased to as short as $t_c = 0.84 \pm 0.02\tau_o$ for a high impact velocity while the shortest one that has been reported in the literature is $t_c \approx 1.2\tau_o$ [87]. As discussed earlier, the effect of curvature, ribbed pattern, and the additional macrotexture in the axial direction (our specific design) collaborated to yield such an unprecedented short contact time. We hope that considering our findings for the contact time reduction trend on curved surfaces will assist future numerical investigations to yield solutions quantitatively comparable to experimental results.

Chapter 6 Overall Conclusions and Future Work

6.1 Conclusions

Inspired from the skin patterns of a human being's finger print and a gecko's toe, the idea of studying the liquid interaction with a non-wettable surface fully structured with macroscopic ridges has been formed. Utilizing an extruder-type 3D printer, a solid specimen with ribbed surface pattern was obtained, on which we deposited our non-wettable soot-based coating. The liquid interaction with the ribbed surface has been investigated from two perspectives: 1- How does a liquid drop move on such a solid substrate? 2- What happens when a water drop impacts on them?

Investigating the motion of viscous drops on the ribbed non-wettable surface tilted at different angles, it was found that such a surface pattern assists the liquid drops to roll down $\sim 27\%$ faster (along the ridges) compared to the surface with no ridges. Such a faster rolling can be attributed to the preserved air layers underneath the drops which causes lower friction. A scaling model which predicts the descent velocity of the rolling drops more accurately was developed in this part of the dissertation. In addition, the wettability study on the functionalization process of our chimney-modified soot coating has released that the surface energy of the coating increases after ethanol treatment, yet significantly decreases after perfluorocarbon treatment, which results in the oil-repellency of the coating.

Studying the water droplet impacting on the ribbed surfaces showed that when the kinetic energy of the drop is sufficient to completely wet the ridges, intermediate regime, the contact time becomes shorter as the consequence of $\sim \sqrt{\pi/2}$ faster retraction velocity. This shortening, which is below the theoretical Rayleigh limit, is regardless of the location of the impact point. The contact becomes even shorter at higher impact velocity due to drop splashing from its periphery. The

innovative and simplified method of fabrication presented in this part of dissertation was employed to fabricate a superhydrophobic sample with a specific design to achieve the shortest possible contact time.

Examining the impacts of water droplets with three different diameters on cylindrically-curved superhydrophobic surfaces of two diameters for varied impact velocities has led to a scaling model for the contact time reduction with respect to the impact velocity for such curved surfaces. Since the normalized retraction velocity (V_r^* defined in Chapter 5) in the axial direction is proportional to $x^{*\frac{3}{2}}$ (normalized spreading length in the axial direction), it can be concluded that $\frac{t_c}{\tau_0} \sim We^{-0.12}$. Such a scaling model was confirmed for impacts of five varied R/R_o ratios on smooth-/ribbed-curved surfaces. The specific design, which was speculated to exhibit the shortest possible contact time, was a ribbed-curved surface with an additional macroscopic wire on top of its peak. It was shown that the contact time of this design has become even shorter than the inertial-capillary time scale ($\approx 0.84\tau_0$). It should be emphasized that the shortest contact time that has been reported so far in the literature was $\approx 1.2\tau_0$ [87].

6.2 Future Work

The liquid-interaction with ribbed surfaces has been studied by experiments in this dissertation and the results illustrate that this surface exhibit more efficient non-wettability. The numerical simulation of this interaction can clarify the complexity of this problem further and more innovative ideas to improve its performance can be generated, hence, this will be the study to be done in the future.

As explained earlier, the maximum spreading diameter of impacting a viscous drop is controlled by the Reynolds number as opposed to the Weber number for inviscid drops like water. This means that the scenario of the impact of a viscous droplet is completely different than what has been studied in this dissertation. Thus, it will be scientifically very interesting to investigate the viscous impact on the surfaces discussed in this work.

Since the ribbed surface has shown not only a shorter contact time but also faster droplet rolling on itself, it can be speculated that this surface pattern exhibits an excellent performance in anti-icing applications. However, the droplet splashing that occurs on this surface may cause some issues in subzero environment. Such tiny droplets may not leave the surface after separating from the original drop due to their low inertia. Therefore, it is worth experimentally investigating the anti-icing performance of the ribbed surface at environment with subzero temperature.

Chapter 7 References

- [1] L. Feng, S. Li, Y. Li, H. Li, L. Zhang, J. Zhai, Y. Song, B. Liu, L. Jiang, D. Zhu, Superhydrophobic surfaces: from natural to artificial, *Advanced materials* 14(24) (2002) 1857-1860.
- [2] G.S. Watson, D.W. Green, L. Schwarzkopf, X. Li, B.W. Cribb, S. Myhra, J.A. Watson, A gecko skin micro/nano structure—A low adhesion, superhydrophobic, anti-wetting, self-cleaning, biocompatible, antibacterial surface, *Acta biomaterialia* 21 (2015) 109-122.
- [3] A.Y. Stark, T.W. Sullivan, P.H. Niewiarowski, The effect of surface water and wetting on gecko adhesion, *Journal of Experimental Biology* 215(17) (2012) 3080-3086.
- [4] A.Y. Stark, N.A. Wucinich, E.L. Paoloni, P.H. Niewiarowski, A. Dhinojwala, Self-drying: a gecko's innate ability to remove water from wet toe pads, *PLoS One* 9(7) (2014) e101885.
- [5] T. Young, An essay on the cohesion of fluids, *Philosophical Transactions of the Royal Society of London* 95 (1805) 65-87.
- [6] A.W. Neumann, R. David, Y. Zuo, *Applied surface thermodynamics*, CRC Press 2010.
- [7] P.-G. De Gennes, F. Brochard-Wyart, D. Quéré, *Capillarity and wetting phenomena: drops, bubbles, pearls, waves*, Springer Science & Business Media 2013.
- [8] A. Lafuma, D. Quéré, Superhydrophobic states, *Nature materials* 2(7) (2003) 457-460.
- [9] D. Quéré, Wetting and roughness, *Annu. Rev. Mater. Res.* 38 (2008) 71-99.
- [10] S. Zhang, X. Ouyang, J. Li, S. Gao, S. Han, L. Liu, H. Wei, Underwater Drag-Reducing Effect of Superhydrophobic Submarine Model, *Langmuir* 31(1) (2014) 587-593.
- [11] L. Yuan, J. Dai, X. Fan, T. Song, Y.T. Tao, K. Wang, Z. Xu, J. Zhang, X. Bai, P. Lu, Self-cleaning flexible infrared nanosensor based on carbon nanoparticles, *ACS nano* 5(5) (2011) 4007-4013.
- [12] Y. Lu, S. Sathasivam, J. Song, C.R. Crick, C.J. Carmalt, I.P. Parkin, Robust self-cleaning surfaces that function when exposed to either air or oil, *Science* 347(6226) (2015) 1132-1135.
- [13] E.-C. Cho, C.-W. Chang-Jian, H.-C. Chen, K.-S. Chuang, J.-H. Zheng, Y.-S. Hsiao, K.-C. Lee, J.-H. Huang, Robust multifunctional superhydrophobic coatings with enhanced water/oil separation, self-cleaning, anti-corrosion, and anti-biological adhesion, *Chemical Engineering Journal* 314 (2017) 347-357.
- [14] Z. Yang, L. Wang, W. Sun, S. Li, T. Zhu, W. Liu, G. Liu, Superhydrophobic epoxy coating modified by fluorographene used for anti-corrosion and self-cleaning, *Applied Surface Science* 401 (2017) 146-155.
- [15] S. Farhadi, M. Farzaneh, S. Kulinich, Anti-icing performance of superhydrophobic surfaces, *Applied Surface Science* 257(14) (2011) 6264-6269.
- [16] K. Sobolev, M. Nosonovsky, T. Krupenkin, I. Flores-Vivian, S. Rao, M. Kozhukhova, V. Hejazi, S. Muzenski, B. Bosch, R. Rivero, Anti-icing and de-icing superhydrophobic concrete to improve the safety on critical elements on roadway pavements, 2013.

- [17] J.B. Boreyko, C.-H. Chen, Self-propelled dropwise condensate on superhydrophobic surfaces, *Physical Review Letters* 103(18) (2009) 184501.
- [18] X. Chen, J. Wu, R. Ma, M. Hua, N. Koratkar, S. Yao, Z. Wang, Nanograsped micropyramidal architectures for continuous dropwise condensation, *Advanced functional materials* 21(24) (2011) 4617-4623.
- [19] M.M. Garimella, S. Koppu, S.S. Kadlaskar, V. Pillutla, W. Choi, Difference in growth and coalescing patterns of droplets on bi-philic surfaces with varying spatial distribution, *Journal of colloid and interface science* 505 (2017) 1065-1073.
- [20] X.-M. Li, D. Reinhoudt, M. Crego-Calama, What do we need for a superhydrophobic surface? A review on the recent progress in the preparation of superhydrophobic surfaces, *Chemical Society Reviews* 36(8) (2007) 1350-1368.
- [21] K.D. Esmerlyan, G. McHale, C.L. Trabi, N.R. Geraldi, M.I. Newton, Manipulated wettability of a superhydrophobic quartz crystal microbalance through electrowetting, *Journal of Physics D: Applied Physics* 46(34) (2013) 345307.
- [22] D. Richard, D. Quéré, Viscous drops rolling on a tilted non-wettable solid, *EPL (Europhysics Letters)* 48(3) (1999) 286-291.
- [23] M. Reyssat, D. Richard, C. Clanet, D. Quéré, Dynamical superhydrophobicity, *Faraday discussions* 146 (2010) 19-33.
- [24] S.P. Thampi, R. Adhikari, R. Govindarajan, Do liquid drops roll or slide on inclined surfaces?, *Langmuir* 29(10) (2013) 3339-3346.
- [25] B.S. Yilbas, A. Al-Sharafi, H. Ali, N. Al-Aqeeli, Dynamics of a water droplet on a hydrophobic inclined surface: influence of droplet size and surface inclination angle on droplet rolling, *RSC Advances* 7(77) (2017) 48806-48818.
- [26] L. Mahadevan, Y. Pomeau, Rolling droplets, *Physics of Fluids* 11(9) (1999) 2449-2453.
- [27] R. Rioboo, C. Tropea, M. Marengo, Outcomes from a drop impact on solid surfaces, *Atomization and Sprays* 11(2) (2001).
- [28] P. Tsai, R. CA van der Veen, M. van de Raa, D. Lohse, How micropatterns and air pressure affect splashing on surfaces, *Langmuir* 26(20) (2010) 16090-16095.
- [29] L. Xu, W.W. Zhang, S.R. Nagel, Drop splashing on a dry smooth surface, *Physical review letters* 94(18) (2005) 184505.
- [30] P. Tsai, M.H. Hendrix, R.R. Dijkstra, L. Shui, D. Lohse, Microscopic structure influencing macroscopic splash at high Weber number, *Soft Matter* 7(24) (2011) 11325-11333.
- [31] D. Richard, C. Clanet, D. Quéré, Surface phenomena: Contact time of a bouncing drop, *Nature* 417(6891) (2002) 811-811.
- [32] D. Richard, D. Quéré, Bouncing water drops, *EPL (Europhysics Letters)* 50(6) (2000) 769.
- [33] K. Okumura, F. Chevy, D. Richard, D. Quéré, C. Clanet, Water spring: A model for bouncing drops, *EPL (Europhysics Letters)* 62(2) (2003) 237.
- [34] L. Rayleigh, On the capillary phenomena of jets, *Proc. R. Soc. London*, 1879, pp. 71-97.

- [35] L. Wachters, N. Westerling, The heat transfer from a hot wall to impinging water drops in the spheroidal state, *Chemical Engineering Science* 21(11) (1966) 1047-1056.
- [36] C. Clanet, C. Béguin, D. Richard, D. Quéré, Maximal deformation of an impacting drop, *Journal of Fluid Mechanics* 517 (2004) 199-208.
- [37] C. Extrand, S.I. Moon, When sessile drops are no longer small: Transitions from spherical to fully flattened, *Langmuir* 26(14) (2010) 11815-11822.
- [38] G. Taylor, D. Michael, On making holes in a sheet of fluid, *Journal of fluid mechanics* 58(04) (1973) 625-639.
- [39] J.C. Bird, R. Dhiman, H.-M. Kwon, K.K. Varanasi, Reducing the contact time of a bouncing drop, *Nature* 503(7476) (2013) 385-388.
- [40] A. Gauthier, S. Symon, C. Clanet, D. Quéré, Water impacting on superhydrophobic macrotextures, *Nature communications* 6 (2015).
- [41] Y. Liu, M. Andrew, J. Li, J.M. Yeomans, Z. Wang, Symmetry breaking in drop bouncing on curved surfaces, *Nature communications* 6 (2015) 10034-10034.
- [42] G. Taylor, The dynamics of thin sheets of fluid. III. Disintegration of fluid sheets, *Proceedings of the Royal Society of London A: Mathematical, Physical and Engineering Sciences*, The Royal Society, 1959, pp. 313-321.
- [43] F. Culick, Comments on a ruptured soap film, *Journal of applied physics* 31(6) (1960) 1128.
- [44] M. Abolghasemibizaki, C.J. Robertson, C.P. Fergusson, R.L. McMasters, R. Mohammadi, Rolling viscous drops on a non-wettable surface containing both micro-and macro-scale roughness, *Physics of Fluids* 30(2) (2018) 023105.
- [45] M. Abolghasemibizaki, R. Mohammadi, Droplet impact on superhydrophobic surfaces fully decorated with cylindrical macrotextures, *Journal of colloid and interface science* 509 (2018) 422-431.
- [46] M. Abolghasemibizaki, R.L. McMasters, R. Mohammadi, Towards the Shortest Possible Contact Time: Droplet Impact on Cylindrical Superhydrophobic Surfaces Structured with Macro-Scale Features, *Journal of Colloid and Interface Science* 521 (2018) 17-23.
- [47] K.D. Esmerlyan, C.E. Castano, A.H. Bressler, M. Abolghasemibizaki, R. Mohammadi, Rapid Synthesis of Inherently Robust and Stable Superhydrophobic Carbon Soot Coatings, *Applied Surface Science* 369 (2016) 341-347.
- [48] K.D. Esmerlyan, C.E. Castano, M. Abolghasemibizaki, R. Mohammadi, An artful method for in-situ assessment of the anti-biofouling potential of various functional coatings using a quartz crystal microbalance, *Sensors and Actuators B: Chemical* 243 (2017) 910-918.
- [49] K.D. Esmerlyan, C.E. Castano, A.H. Bressler, M. Abolghasemibizaki, C.P. Fergusson, A. Roberts, R. Mohammadi, Kinetically driven graphite-like to diamond-like carbon transformation in low temperature laminar diffusion flames, *Diamond and Related Materials* 75 (2017) 58-68.
- [50] K.K. Lau, J. Bico, K.B. Teo, M. Chhowalla, G.A. Amaratunga, W.I. Milne, G.H. McKinley, K.K. Gleason, Superhydrophobic carbon nanotube forests, *Nano Letters* 3(12) (2003) 1701-1705.

- [51] Z. Yoshimitsu, A. Nakajima, T. Watanabe, K. Hashimoto, Effects of surface structure on the hydrophobicity and sliding behavior of water droplets, *Langmuir* 18(15) (2002) 5818-5822.
- [52] M. Sun, C. Luo, L. Xu, H. Ji, Q. Ouyang, D. Yu, Y. Chen, Artificial lotus leaf by nanocasting, *Langmuir* 21(19) (2005) 8978-8981.
- [53] X.J. Feng, L. Jiang, Design and Creation of Superwetting/Antiwetting Surfaces, *Advanced Materials* 18(23) (2006) 3063-3078.
- [54] E. Martines, K. Seunarine, H. Morgan, N. Gadegaard, C.D. Wilkinson, M.O. Riehle, Superhydrophobicity and superhydrophilicity of regular nanopatterns, *Nano letters* 5(10) (2005) 2097-2103.
- [55] Y. Xiu, S. Zhang, V. Yelundur, A. Rohatgi, D.W. Hess, C. Wong, Superhydrophobic and low light reflectivity silicon surfaces fabricated by hierarchical etching, *Langmuir* 24(18) (2008) 10421-10426.
- [56] Z. Wang, C. Lopez, A. Hirs, N. Koratkar, Impact dynamics and rebound of water droplets on superhydrophobic carbon nanotube arrays, *Applied physics letters* 91(2) (2007) 023105.
- [57] X. Deng, L. Mammen, H.-J. Butt, D. Vollmer, Candle soot as a template for a transparent robust superamphiphobic coating, *Science* 335(6064) (2012) 67-70.
- [58] K. Seo, M. Kim, Candle-based process for creating a stable superhydrophobic surface, *Carbon* 68 (2014) 583-596.
- [59] K. Esmeryan, E. Radeva, L. Vergov, Z. Raicheva, T. Angelov, Humidity tolerant organic vapor detection using a superhydrophobic quartz crystal microbalance, *IEEE Sensors Journal* (2015) 1-1.
- [60] L. Shen, W. Wang, H. Ding, Q. Guo, Flame soot stably deposited on silicone coatings possess superhydrophobic surface, *Applied surface science* 284 (2013) 651-656.
- [61] J. Lötters, W. Olthuis, P. Veltink, P. Bergveld, The mechanical properties of the rubber elastic polymer polydimethylsiloxane for sensor applications, *Journal of Micromechanics and Microengineering* 7(3) (1997) 145.
- [62] W. Brostow, N.M. Glass, Cure progress in epoxy systems: dependence on temperature and time, *Materials Research Innovations* 7(3) (2003) 125-132.
- [63] K.D. Esmeryan, C.E. Castano, A.H. Bressler, C.P. Fergusson, R. Mohammadi, Single-step flame synthesis of carbon nanoparticles with tunable structure and chemical reactivity, *RSC Advances* 6(66) (2016) 61620-61629.
- [64] O.A. Shenderova, Detonation nanodiamonds: science and applications, Pan Stanford Publishing 2014.
- [65] O. Popovicheva, N.M. Persiantseva, N.K. Shonija, P. DeMott, K. Koehler, M. Petters, S. Kreidenweis, V. Tishkova, B. Demirdjian, J. Suzanne, Water interaction with hydrophobic and hydrophilic soot particles, *Physical Chemistry Chemical Physics* 10(17) (2008) 2332-2344.
- [66] K.D. Esmeryan, A.H. Bressler, C.E. Castano, C.P. Fergusson, R. Mohammadi, Rational strategy for the atmospheric icing prevention based on chemically functionalized carbon soot coatings, *Applied Surface Science* 390 (2016) 452-460.

- [67] E. Omrani, B. Barari, A.D. Moghadam, P.K. Rohatgi, K.M. Pillai, Mechanical and tribological properties of self-lubricating bio-based carbon-fabric epoxy composites made using liquid composite molding, *Tribology International* 92 (2015) 222-232.
- [68] B. Barari, E. Omrani, A.D. Moghadam, P.L. Menezes, K.M. Pillai, P.K. Rohatgi, Mechanical, physical and tribological characterization of nano-cellulose fibers reinforced bio-epoxy composites: an attempt to fabricate and scale the 'Green' composite, *Carbohydrate polymers* 147 (2016) 282-293.
- [69] D. Khojasteh, S.M. Mousavi, R. Kamali, CFD analysis of Newtonian and non-Newtonian droplets impinging on heated hydrophilic and hydrophobic surfaces, *Indian Journal of Physics* 91(5) (2017) 513-520.
- [70] S.A. Mayer, R.G. Kowalski, M. Presciutti, N.D. Ostapovich, E. McGann, B.-F. Fitzsimmons, D.R. Yavagal, Y.E. Du, A.M. Naidech, N.A. Janjua, Clinical trial of a novel surface cooling system for fever control in neurocritical care patients, *Critical care medicine* 32(12) (2004) 2508-2515.
- [71] J. Fang, M. Davoudi, G. Chase, Drop movement along a fiber axis due to pressure driven air flow in a thin slit, *Separation and Purification Technology* 140 (2015) 77-83.
- [72] M. Davoudi, E. Moore, G. Chase, Motion of water drops on hydrophobic expanded polymer mat surfaces due to tangential air flow, *Journal of the Taiwan Institute of Chemical Engineers* (2017).
- [73] W.-T. Cao, Y.-J. Liu, M.-G. Ma, J.-F. Zhu, Facile preparation of robust and superhydrophobic materials for self-cleaning and oil/water separation, *Colloids and Surfaces A: Physicochemical and Engineering Aspects* 529 (2017) 18-25.
- [74] P. Aussillous, D. Quéré, Liquid marbles, *Nature* 411(6840) (2001) 924-927.
- [75] K.D. Esmerlyan, C.E. Castano, R. Mohammadi, Interactions of superhydrophobic carbon soot coatings with short alkyl chain alcohols and fluorocarbon solutions, *Colloids and Surfaces A: Physicochemical and Engineering Aspects* 529 (2017) 715-724.
- [76] D.K. Owens, R. Wendt, Estimation of the surface free energy of polymers, *Journal of applied polymer science* 13(8) (1969) 1741-1747.
- [77] S. Wu, Calculation of interfacial tension in polymer systems, *Journal of Polymer Science: Polymer Symposia*, Wiley Online Library, 1971, pp. 19-30.
- [78] S. Chiu, S.-J. Hwang, C. Chu, D. Gan, The influence of Cr-based coating on the adhesion force between epoxy molding compounds and IC encapsulation mold, *Thin Solid Films* 515(1) (2006) 285-292.
- [79] M.-C. Michalski, S. Desobry, M.-N. Pons, J. Hardy, Adhesion of edible oils to food contact surfaces, *Journal of the American Oil Chemists' Society* 75(4) (1998) 447-454.
- [80] S. Wu, Polymer interface and adhesion, M. Dekker 1982.
- [81] F. Brochard-Wyart, H. Hervet, C. Redon, F. Rondelez, Spreading of "heavy" droplets: I. Theory, *Journal of colloid and interface science* 142(2) (1991) 518-527.
- [82] X. Jiang, H.Z. Li, Liquid Drops Hurdling Barriers of Various Geometries, *Advanced Materials Interfaces* 4(17) (2017) 1700516-1700523.

- [83] R.B. Bird, W.E. Stewart, E.N. Lightfoot, Transport phenomena, John Wiley & Sons 2007.
- [84] T. Deng, K.K. Varanasi, M. Hsu, N. Bhate, C. Keimel, J. Stein, M. Blohm, Nonwetting of impinging droplets on textured surfaces, *Applied Physics Letters* 94(13) (2009) 133109.
- [85] S. Chandra, C. Avedisian, On the collision of a droplet with a solid surface, *Proceedings of the Royal Society of London A: Mathematical, Physical and Engineering Sciences*, The Royal Society, 1991, pp. 13-41.
- [86] M. Rein, Phenomena of liquid drop impact on solid and liquid surfaces, *Fluid Dynamics Research* 12(2) (1993) 61-93.
- [87] C.J. Patterson, S. Shiri, J.C. Bird, Macrot textured spoked surfaces reduce the residence time of a bouncing Leidenfrost drop, *Journal of Physics: Condensed Matter* 29(6) (2016) 064007.
- [88] A. Worthington, On the forms assumed by drops of liquids falling vertically on a horizontal plate, *Proceedings of the royal society of London* 25(171-178) (1876) 261-272.
- [89] D. Khojasteh, A. Bordbar, R. Kamali, M. Marengo, Curvature effect on droplet impacting onto hydrophobic and superhydrophobic spheres, *International Journal of Computational Fluid Dynamics* 31(6-8) (2017) 310-323.
- [90] J. Song, M. Gao, C. Zhao, Y. Lu, L. Huang, X. Liu, C.J. Carmalt, X. Deng, I.P. Parkin, Large-Area Fabrication of Droplet Pancake Bouncing Surface and Control of Bouncing State, *ACS nano* 11(9) (2017) 9259-9267.
- [91] S. Das, B. Yang, G. Gu, P.C. Joshi, I.N. Ivanov, C.M. Rouleau, T. Aytug, D.B. Geohegan, K. Xiao, High-performance flexible perovskite solar cells by using a combination of ultrasonic spray-coating and low thermal budget photonic curing, *Acs Photonics* 2(6) (2015) 680-686.
- [92] A. Yusof, H. Keegan, C.D. Spillane, O.M. Sheils, C.M. Martin, J.J. O'Leary, R. Zengerle, P. Koltay, Inkjet-like printing of single-cells, *Lab on a Chip* 11(14) (2011) 2447-2454.
- [93] L. Mishchenko, B. Hatton, V. Bahadur, J.A. Taylor, T. Krupenkin, J. Aizenberg, Design of ice-free nanostructured surfaces based on repulsion of impacting water droplets, *ACS nano* 4(12) (2010) 7699-7707.
- [94] M. Pasandideh-Fard, Y.M. Qiao, S. Chandra, J. Mostaghimi, Capillary effects during droplet impact on a solid surface, *Physics of Fluids* 8(3) (1996) 650.

Appendix: Vita

Mehran Abolghasemibizaki

abolghasemibm@vcu.edu

PhD in Mechanical and Nuclear Engineering Department (GPA: 3.8)

May 2018

Virginia Commonwealth University, Richmond VA

ACCOMPLISHMENTS

- ❖ Published Nine (9) **peer-reviewed papers** in prestigious journals such as *Journal of Colloid and Interface Science*. Published the last three in less than one year after defending my proposal.
- ❖ Came up with the innovative idea of fabricating Ribbed superhydrophobic surfaces
- ❖ Finalist for Outstanding Graduate Research Award (2018)
- ❖ Dissertation Assistantship Award (2017)
- ❖ Young Project Manager Award at Kalleh, Dairy Co. (2013)
- ❖ Came up with three techniques which enhanced a thermal energy storage system by 57% (2011)
- ❖ Top 1% (220 out of 15,000) out of over 15,000 Mechanical Engineering Students in National Graduate Studies Entrance Examination (2008)
- ❖ Top 0.1% (184 out of 300,000) out of more than 300,000 Students in National Under-Graduate Studies Entrance Examination (2002)

RESEARCH EXPERTISE

- ❖ Droplet Impact on Non-wettable surfaces
- ❖ Wettability and Characterization of Superhydrophobic Coatings
- ❖ Phase Change Materials and Thermal Energy Storage Systems
- ❖ Heat Transfer and Computational Fluid Dynamics

JOURNAL PAPERS

9. Mehran Abolghasemibizaki, Robert L. McMasters, Reza Mohammadi, “Towards the Shortest Possible Contact Time: Droplet Impact on Cylindrical Superhydrophobic Surfaces Structured with Macro-Scale Features” *Journal of Colloid and Interface Science*, Volume 521, Pages 17-23, 2018. Available [here](#)

8. **Mehran Abolghasemibizaki**, Connor J. Robertson, Christian P. Fergusson, Robert L. McMaster, Reza Mohammadi, “*Rolling Viscous Drops on a Non-wettable Surface Containing both Micro- and Macro-Scale Roughness*” **Physics of Fluids**, Volume 30, **2018**. Available [here](#)
7. **Mehran Abolghasemibizaki** and Reza Mohammadi, “*Droplet Impact on Superhydrophobic Surfaces Decorated with Cylindrical Macrotextures*” **Journal of Colloid and Interface Science**, Volume 509, Pages 422-431, **2018**. Available [here](#)
6. Karekin D. Esmeryan, Carlos E. Castano, Ashton H. Bressler, **Mehran Abolghasemibizaki**, Christian P. Fergusson, Allan Roberts, Reza Mohammadi, “*Kinetically Driven Graphite-like Carbon Transformation in Low Temperature Laminar Diffusion Flames*”, **Diamond and Related Materials**, Volume 75, Pages 58–68, **2017**. Available [here](#)
5. Karekin D. Esmeryan, Carlos E. Castano, **Mehran Abolghasemibizaki**, Reza Mohammadi, “*An Artful Method for In-situ Assessment of the Anti-biofouling Potential of Various Functional Coatings Using a Quartz Crystal Microbalance*”, **Sensors and Actuators B: Chemical**, Volume 243, Pages 910–918, **2017**. Available [here](#)
4. Karekin D. Esmeryan, Carlos E. Castano, Ashton H. Bressler, **Mehran Abolghasemibizaki**, Reza Mohammadi, “*Rapid Synthesis of Inherently Robust and Stable Superhydrophobic Carbon Soot Coatings*”, **Applied Surface Science**, Volume 369, Pages 341–347, **2016**. Available [here](#)
3. **Mehran Abolghasemi**, Ali Keshavarz, Mozaffar A. Mehrabian, “*Thermodynamic Analysis of a Thermal Storage Unit under the Influence of Nano-particles added to the Phase Change Materials and/ or the Working Fluid*”, **Heat and Mass Transfer**, Volume 48, Pages 1961–1970, **2012**. Available [here](#)
2. **Mehran Abolghasemi**, Ali Keshavarz, Mozaffar A. Mehrabian, “*Heat Transfer Enhancement of a Thermal Storage Unit Consisting of a Phase Change Material and Nano-particles*”, **Journal of Renewable and Sustainable Energy**, Volume 4, Issue 4, DOI: 10.1063/1.4747824, **2012**. Available [here](#)
1. Ali Keshavarz, Mozaffar A. Mehrabian, **Mehran Abolghasemi**, Arash Mostafavi “*Availability (exergy) Analysis in a Thermal Energy Storage System with the Phase Change Materials Arranged in Series*”, **Journal of Power and Energy**, Volume 225, Pages 44-52, **2011**. Available [here](#)

EDUCATION

❖ **PhD in Mechanical and Nuclear Engineering (2018) VCU**

Dissertation title: *Liquid Interaction with Non-Wettable Surfaces Structured with Macroscopic Ridges*

❖ **MSc in Mechanical Engineering (Heat Transfer and Fluid Mechanics, 2011)**

K.N. Toosi University of Technology, Tehran, Iran

Thesis title: *Enhancing Thermal Energy Storage Systems under the Influence of Nano-particles Added to the Phase Change Material and/or the Working Fluid*

❖ **BSc in Mechanical Engineering (Solid Mechanics, 2008)**

Amirkabir University of Technology (Tehran Polytechnic), Tehran, Iran

Thesis title: *Analytical Design of a Buckling Test Device for Circular Plates*

PROFESSIONAL EXPERIENCE

❖ **Project Manager/Process Improvement, Kalleh Dairy Co. Iran (Aug 2012-Jun 2013)**

- Assigned projects completed:
 - Installing/Relocating three filling lines (increased the production capacity by 60%)
 - Providing piping and instrumentation diagrams for the entire beverage company
- **Self-initiated projects completed:**
 - Automating the Clean-In-Place (CIP) system
 - Improving the piping system to increase the product quality using less pump/pipe/joint
 - Installing sensors in filling lines and automating their operation (reduced product waste by 10%)
 - Proposing a new packaging for enhancing the heat transfer in the cooling tunnel based on numerical and experimental studies

❖ **Quality Control Supervisor, Parsamizeh Co. Iran (Feb 2007-Nov 2007)**

- Documented the fabrication process for getting ISO 9000 and 9001
- Supervising **15** technicians in the absence of their manager
- Designed molds and fabricated specimens for mechanical testing

ACADEMIC EXPERIENCE

❖ **Graduate Research Assistant**

- Advanced Functional Laboratory, MNE department, VCU, Richmond (Sep 2014-present)
- Mechanical Engineering department, K.N. Toosi University of Technology, (Sep 2008-Aug 2011)

❖ **Teaching Assistant**

- *Mechanical and Nuclear Engineering Materials, Continuum Mechanics* (graduate courses) and *Mechanics of Deformables* (undergraduate course) at MNE department, VCU, Richmond (Sep 2015-May 2017)
- *Fluid Dynamics* and *Thermodynamics* (undergraduate courses) at Department of Mechanical and Materials Engineering, University of Cincinnati, Cincinnati (Sep 2013-Aug 2014)

MEMBERSHIP

- ❖ American Society of Mechanical Engineering (ASME)

STUDENT ORGANIZATIONS & ACTIVITIES

- ❖ **Secretary**, *Engineering Graduate Student Association*, VCU, Richmond, VA (2016-present)
- ❖ **Social Chair**, *Persian Club at VCU*, VCU, Richmond, VA (2014-2015)